**FATIGUE BEHAVIOR OF AN ADVANCED SiC/SiC COMPOSITE
AT ELEVATED TEMPERATURE IN AIR AND IN STEAM**

THESIS

Devon T. Christensen, Captain, USAF

AFIT/GAE/ENY/09-D02

**DEPARTMENT OF THE AIR FORCE
AIR UNIVERSITY**

AIR FORCE INSTITUTE OF TECHNOLOGY

Wright-Patterson Air Force Base, Ohio

AFIT/GAE/ENY/09-D02

FATIGUE BEHAVIOR OF AN ADVANCED SiC/SiC COMPOSITE AT ELEVATED TEMPERATURE IN AIR AND IN STEAM

THESIS

Presented to the Faculty

Department of Aeronautics and Astronautics

Graduate School of Engineering and Management

Air Force Institute of Technology

Air University

Air Education and Training Command

In Partial Fulfillment of the Requirements for the

Degree of Master of Science in Aeronautical Engineering

Devon T. Christensen, BS

Captain, USAF

December 2009

**FATIGUE BEHAVIOR OF AN ADVANCED SiC/SiC COMPOSITE
AT ELEVATED TEMPERATURE IN AIR AND IN STEAM**

Devon T. Christensen, BS

Captain, USAF

Approved:

Marina B. Ruggles-Wrenn, PhD (Chairman)	date

Lt Col Eric D. Swenson (Member)	date

Geoff E. Fair, PhD (Member)	date

Abstract

The fatigue behavior of an advanced Silicon Carbide/Silicon Carbide (SiC/SiC) ceramic matrix composite (CMC) was investigated at 1200 ℃ in laboratory air and in steam environments. The composite consisted of a SiC matrix reinforced with Boron Nitride (BN) coated Hi-Nicalon fibers woven into eight-harness-satin (8HS) weave plies. Tensile stress-strain behavior and tensile properties were also evaluated at 1200 ℃. Tension-tension fatigue tests were conducted in both laboratory air and in steam at 1200 ℃ at frequencies of 0.1 Hz, 1.0 Hz, and 10 Hz. The tension-tension fatigue tests had a ratio of minimum stress to maximum stress of R = 0.1, with maximum stresses ranging from 80-120 MPa in air and 60-110 MPa in steam. Fatigue run-out was defined as 10^5 cycles for 0.1 Hz tests and as 2×10^5 cycles for 1.0 Hz and 10 Hz tests. Strain accumulation with cycles and modulus evolution with cycles were analyzed for each fatigue test. The CMC fatigue performance degraded after moving from the air to the steam environment. Fatigue limit was 100 MPa (46%UTS) in air and 80 MPa (37%UTS) in steam. Specimens that achieved run-out were subjected to tensile tests to failure to characterize the retained tensile properties. All specimens tested in air retained 100% of their tensile strength and only one specimen tested in steam showed strength degradation of approximately 5%. The average modulus loss in air and in steam was limited to 12%.

Acknowledgements

I would like to express my gratitude to the following individuals whose involvement enabled me to complete this research. First, to Dr. Marina Ruggles-Wrenn whose tireless support and wise guidance kept my efforts focused. Next, to Dr. Geoff Fair for sharing his knowledge and testing experience in the field of composites. Then to my fellow students Maj Clint Armani and Lt Brad Diedrick, for their questions, suggestions, and camaraderie during long hours in the lab. Also to the ENY laboratory technicians for their help in setting up and maintaining the laboratory equipment. Above all I have to thank my family for their love and encouragement.

Devon T. Christensen

Table of Contents

List of Figures

List of Tables

FATIGUE BEHAVIOR OF AN ADVANCED SiC/SiC COMPOSITE AT ELEVATED TEMPERATURE IN AIR AND IN STEAM

I. Introduction and Background

Arguably the most difficult obstacle to technological advancement in the aerospace industry is material limitations. Since the invention of the aircraft, flight performance has been a delicate balance of required strength and necessary weight. Aircraft engineers, including the Wright brothers, have always sought increased performance by increasing the former and reducing the latter. The introduction of advanced composite materials greatly simplified achieving these performance improvements. While most composite materials are found in airframe design, the benefits of advanced composite materials have also improved the field of aircraft propulsion, notably modern afterburning turbine engines. The Air Force's participation in the Versatile, Affordable, Advanced Turbine Engines (VAATE) program, which seeks a 200% increase in engine thrust-to-weight ratios, 25 % improvement in efficiency, and a 60% reduction in lifecycle development, procurement, and maintenance cost, is the main impetus for the following work [1].

Composites are engineered materials made from two or more constituents with different physical or chemical properties, with the properties of the final material superior to the properties of either constituent material [4:1]. The two materials, or phases, included in a composite material are classified as matrix, the continuous and usually weaker material, and reinforcement, a discontinuous and generally stiffer and stronger material. In some cases, an interphase material is used between the matrix and reinforcement to prevent undesired chemical interactions, or to promote desired energy dispersion and failure modes in the final composite [3:460; 4:1].

The use of composite materials dates to ancient Egypt where straw reinforced the clay used to make bricks (Exodus). Historians also note composites have been used in aeronautical

applications since the airplane was invented, an example being the doped-fabric covered wings of the Wright Flier [11]. While these are examples of simple composites, doped-fabric can easily be related to the most abundant advanced composite presently in use, fiberglass; both are fibrous reinforcement materials impregnated with curable resin to form a solid final product. As seen in these examples, composites can be classified as either simple or complex. Within the class of complex composites are many groups of advanced composite materials. The main categories are polymer matrix composites, metal matrix composite, and ceramic matrix composites which are the focus of this study [4:25].
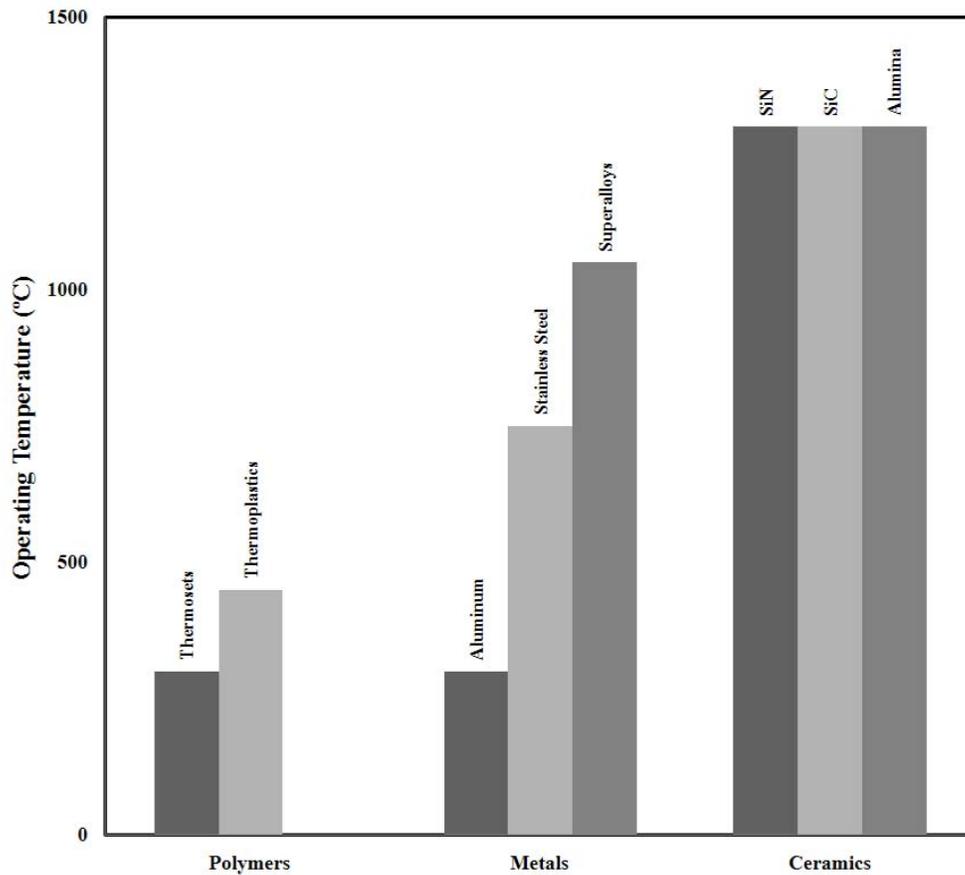
Figure 1: Comparison of Material Operating Temperatures.

The use of advanced composites as primary materials in modern aircraft began in the 1970's. However, their use in propulsion technology lagged, requiring the development of composite materials capable of withstanding the extreme temperature and pressure environments of a jet turbine engine. Predominantly, only high strength steel alloys, Titanium alloys, or metal superalloys such as those based on Nickel or Cobalt were capable of maintaining their structural integrity in these operating conditions, and their performance was still severely temperature-limited. Figure 1 outlines the operating temperatures of the main classes of materials.

Ceramic materials are able to withstand the high temperatures components experience in jet turbine engine. Ceramics are divisible into two classes: traditional and advanced. Traditional ceramics are items such as bricks, pottery, or tiles. Advanced ceramics are usually obtained through sophisticated chemical processes and have improved performance over traditional ceramics. Despite their high temperature capabilities, both classes of ceramics suffer from extremely low fracture toughness, that is, minor crack defects will cause catastrophic failure of the whole item [3:4; 2:460]. To combat this catastrophic failure mode, material engineers began developing ceramic matrix composites (CMCs). While polymer and metal matrix composites use the reinforcement material to increase strength, CMCs use reinforcement to increase toughness.

The primary reason monolithic ceramics fail catastrophically is that they lack energy dissipating mechanisms within the material. For example, when a metal experiences an impact, the impact energy is distributed along the many dislocations within the metal's crystalline structure, allowing the metal to deform plastically before failing [5:41-42]. Ceramics cannot dissipate energy in the same manner. The main advantage of CMCs over monolithic ceramics is their graceful failure mode. Engineers accomplish this by focusing on the interaction between

3

the matrix and the reinforcing fibers. If the fiber-matrix bond is too strong, any matrix cracks will continue to grow through the fiber as in monolithic ceramics. However, weak fiber-matrix interaction allows damage energy to be dispersed through the material via fiber-matrix debonding, crack deflection, fiber bridging, or fiber pull out [2:460; 3:4-5]. Since most CMC use very similar materials as matrix and reinforcement the fiber-matrix bond is naturally quite strong, therefore several types of interphase material (i.e. fiber coatings) are used to create a weak fiber-matrix interface.
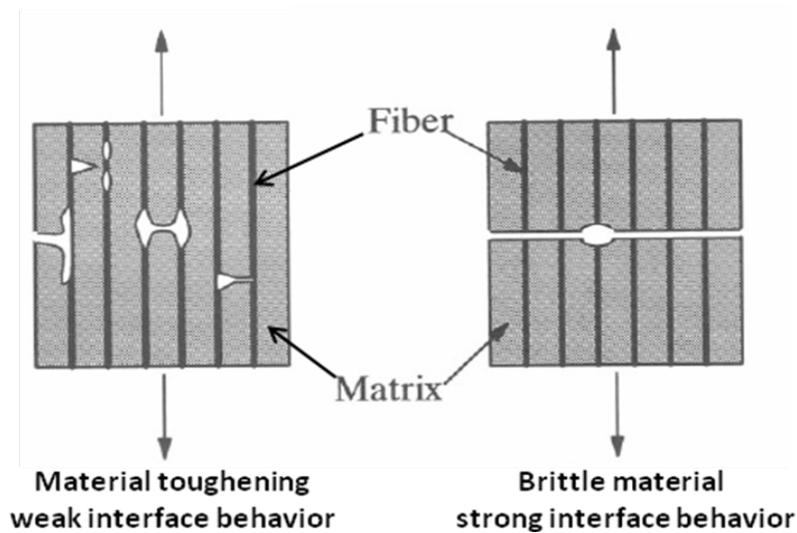
Figure 2: Fracture damage comparison between CMCs with weak versus strong interface bonds.

Material selection for all CMC components is very specific to the final application of the CMC. CMC matrix and reinforcements are either oxide or non-oxide materials. Oxides are oxidation resistant at almost any temperature. Non-oxide materials often have better high temperature mechanical properties than oxides, but they start to suffer from oxidation at those temperatures. Due to their excellent high temperature material properties, non-oxide materials are a common choice in CMCs, provided the fibers are protected with an oxidation and temperature resistant interphase coating [2:470].

One of the most important non-oxide ceramic materials developed and used as both a matrix and a fiber material is Silicon Carbide (SiC). This very hard, abrasive material has a high melting point and excellent high temperature mechanical properties, and is resistant to erosion and chemical degradation in reducing environments. However, it does not occur naturally so production can be difficult and expensive, and it will oxidize to Silicon Oxide at temperatures between 900-1100 °C. As manufacturing processes matured, the use of SiC/SiC CMCs in turbine engine components such as exhaust cones, nozzle flaps, flame stabilizers and casing struts increased [13:340]. Continued research seeks to expand the applications of CMC in the aerospace industry.

A number of experimental research efforts were undertaken to determine the suitability of CMCs for aerospace applications. Some of the earliest work was performed by Mizuno and co-workers at the Japan Fine Ceramics Center in Nagoya, Japan [15: 3065-3077]. Mizuno's work focused on 2D-woven, chemical-vapor-infiltrated (CVI) SiC/SiC composites. The tensile properties of these materials were evaluated at room temperature in air, and at 1000 °C in argon. The use of argon provides an inert environment for testing. The room-temperature test results provided baseline material properties and tensile stress-strain behavior. Differences in properties and behaviors were then measured during the tests conducted at high temperature in the inert environment. The high-temperature fatigue tests were performed at 20 Hz using an atmosphere controlled furnace. At room temperature, the ultimate tensile strength (UTS) was 209 MPa with a proportional limit of 80 MPa and a modulus of 250 GPa, while at high temperature the proportional limit increased to 100 MPa and the modulus increased to 260 MPa. At high temperature, Mizuno et al. reported a fatigue limit of 75 MPa, which is about 30% of the UTS.

Since the high-temperature tests were performed in an inert environment, it is assumed that the observed responses reflected pure material behaviors.

Zawada and co-workers at the Air Force Research Laboratory extended Mizuno's work by investigating the behavior of three Nicalon fiber containing composites at 1000°C subjected to fatigue at 1.0 Hz in oxidizing environments of steam and salt fog [24: 1282-1291]. The composites tested by Zawada et al. were produced using a polymer infiltration and pyrolysis (PIP) process. Unlike the CVI process, PIP involves infusing the fiber pre-forms with a polymer then pyrolyzing the material, to convert the polymer to a ceramic matrix. Zawada et al. followed Mizuno's procedure of first performing tensile tests to establish baseline material properties, then performing cyclic fatigue. Zawada et al. employed a temperature chamber with steam generating capability and performed periods of cyclic fatigue followed by periods of exposure to the oxidizing environment. Figure 3 below summarizes Zawada's finding with Nicalon/SiNC.
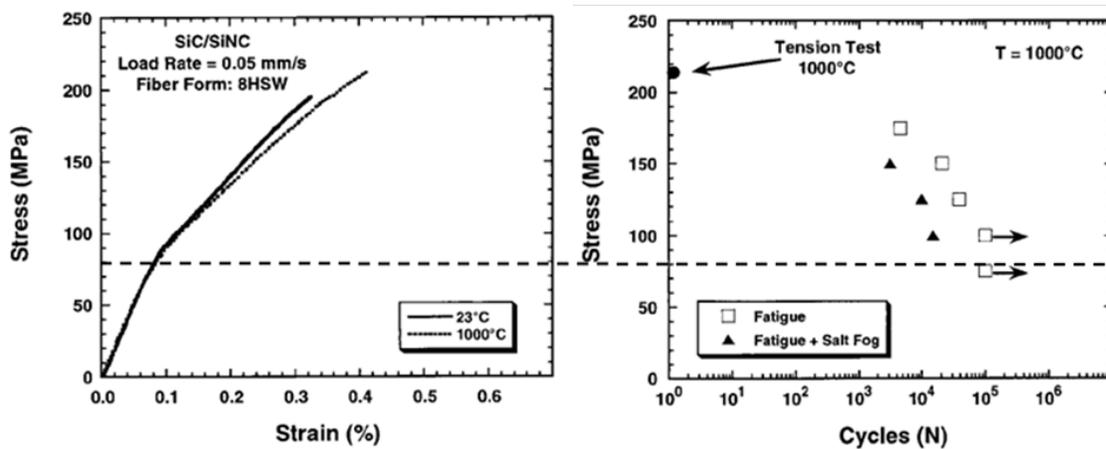
Figure 3: Room and high temperature tensile behavior vs. high temperature fatigue behavior of a Nicalon/SiNC CMC in an oxidizing environment as reported by Zawada [24: 1284, 1286]. The dashed line corresponds to the proportional limit.

Both Mizuno and Zawada show that the tensile stress-strain curves of the CMCs tested had a nearly bi-linear appearance with an initial linear elastic region extending up to the proportional

limit, which corresponded to initial matrix cracking. Once the stresses exceed the proportional

limit, load is transferred to the fibers, with the upper portion of the curve terminating once the

ultimate tensile strength is reached. During fatigue testing, the fatigue limit was 100 MPa, which

was higher than the proportional limit of 75 MPa. However, in the presence of salt fog, failure

behavior was influenced by aggressive degradation. None of the specimens tested in salt fog

achieved fatigue run-out. However, a significant decrease in fatigue life was observed for fatigue

stresses ≥ 100 MPa.

Sharma at the Air Force Institute of Technology, structured his research effort using an

approach similar to that employed by Zawada et al. Sharma examined three CMCs with similar

constituents and compared the fatigue performance of two CMCs (C1 and C2) in air and in steam

at 1300 ℃. For the third material (C3), Sharma aged the specimens in air and in steam and then

tested them in order to determine the effects of prior aging on tensile properties. The

proportional limit for the material C1 was 140 MPa, and the proportional limit for material C2

was 100 MPa. Sharma determined that for material C1 the presence of steam did not affect the

fatigue limit of 100 MPa. However, the lifetime of specimens tested in steam was reduced as the

fatigue stress level approached the proportional limit. The reduction is fatigue life was attributed

to the increased matrix cracking near the proportional limit allowing the oxidizing environment

to access and degrade the fibers. In the case of material C2, the fatigue limit and the fatigue

lifetime decreased in the oxidizing steam environment, showing higher susceptibility of this

material to the degrading presence of steam.

Although previous tests investigated the effects of environment on fatigue behavior, all

the fatigue testing was conducted at one frequency. In many aerospace applications the

component will experience different fatigue frequencies during service. For that reason, it is

important to determine the effect not only of the oxidizing test environment, but also of the fatigue frequency on the fatigue behavior of CMC materials.

The present effort aims to evaluate the fatigue performance of the Hi-Nicalon/BN/SiC ceramic composite produced via the CVI process at 1200°C in air and in steam. In addition, the effects of loading frequency on the fatigue durability of this CMC are assessed.

<center>**II. Materials and Specimens**</center>

This chapter provides an overview of the advanced SiC/SiC composite material tested, the preparation of the test specimens, the test equipment used, testing procedures, and concludes with a description of the post failure specimen analysis.

2.1 Test Material

The material studied in this research effort was manufactured by Hyper-Therm High-Temperature Composites, Inc., Huntington Beach CA, by chemical vapor infiltration (CVI) of SiC into the woven Hi-Nicalon fiber preforms. The composite was supplied in the form of three 3.1 mm thick plates. The composite consisted of eight plies of Hi-Nicalon [0°/90°] fabric woven in an 8 harness satin weave (8HSW). To produce the laminated preforms, the 8 [0°/90°] plies were laid-up symmetric about mid-plane with warp and fill plies alternated. Prior to matrix densification, the preforms were coated with boron nitride (BN) in order to decrease interface bonding between fibers and matrix, thereby increasing composite strength and toughness. The thickness of fiber coating was ~0.25 μm. The SiC matrix was densified by CVI. The volume fraction of the fibers was 34.6% and the porosity of the composite was 9.5%. The density of the composite was 2.70 g/cm^3. The tensile specimens (dimensions are given in Section 2.2 below) had an outer seal coating of SiC that was applied by chemical vapor deposition (CVD) after the specimens had been machined.

<center>**Table 1: Specifications of the as-processed Hi-Nicalon/BN/SiC plates**</center>

Panel ID	Mass (g)	Planform Size (in x in)	Average thickness (in)	Density (g/cm^3)	Fiber Volume (%)	Calculated Fiber Coating Volume (%)	Calculated Matrix Volume (%)	Calculated Porosity (%)
9C-316-P1	215.70	6.25 x 6.25	0.124	2.72	34.4	2.5	54.3	8.8
9C-316-P2	210.92	6.25 x 6.25	0.122	2.70	34.9	2.5	53.2	9.4
9C-316-P3	210.30	6.25 x 6.25	0.123	2.67	34.6	2.5	52.5	10.3

Average Density: 2.70 g/cm^3
Average Fiber Volume: 34.6%

2.1.1 SiC Matrix

Selection of a matrix material is usually governed by thermal stability requirements and processing considerations [2:467]. SiC is an obvious choice for turbine applications due to its excellent high temperature mechanical properties and high melting point. SiC is not without drawbacks, which include oxidation of any free silicon remaining after production using methods such as melt infiltration, and the SiC itself as temperatures near 1000 °C. These effects can be mitigated through processing.

Production of the Hi-Nicalon/BN/SiC material for this study used the Chemical Vapor Infiltration (CVI) method, outlined below.
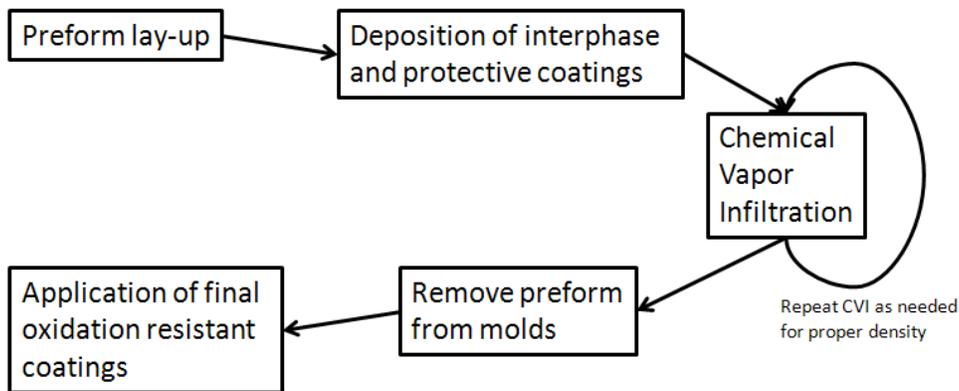
Figure 4: Chemical Vapor Infiltration process.

To obtain SiC via CVI, manufacturer place a porous reinforcement material in an autoclave in which the chemical methyltrichlorosilane (CH_3SiCl_3) is decomposed with Hydrogen (H_2) at temperatures between 1000 °C – 1350 °C. The reaction is as follows:

$$CH_3SiCl_3(g) \rightarrow SiC(s) + 3HCl(g)$$

The resulting solid SiC infiltrates and densifies the porous areas of the reinforcement while the resultant gaseous HCl is vented. To increase the melting and working temperatures of the final SiC matrix, the CVI processing temperature is increased [2:482-484; 3:122-123].

The major drawback to CVI processing of matrix material is porosity. As the reaction

starts, SiC deposits preferentially at the first surfaces encountered, often sealing off deeper

portions of the reinforcement material forming voids [2:483]. This void porosity has three

modes, within the fiber bundles, between the layers, and as conjoined holes through fiber layers.

The first two modes account for over 95% of the porosity in CVI produced materials [3:123].

Hyper-Therm reported 8.8-10.2% porosity in the parent Hi-Nicalon/BN/SiC panels, which is

seen in the following microstructure image.
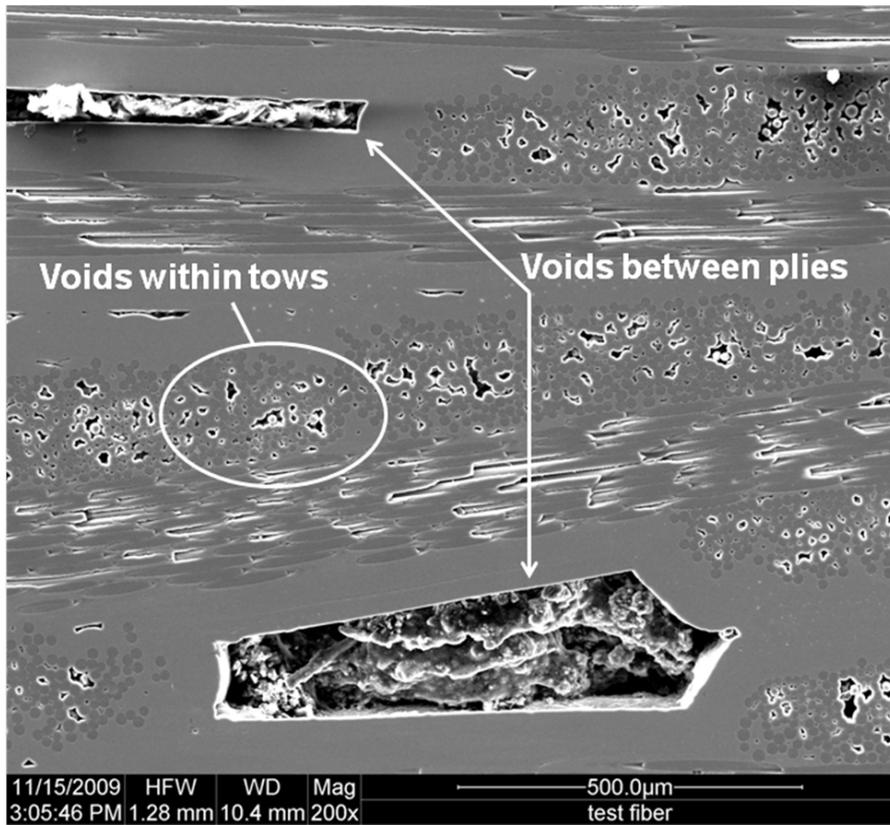
Figure 5: SEM micrograph of polished, as-processed Hi-Nicalon/BN/SiC specimen showing a) voids between plies and b) voids within tows.

2.1.2 SiC Reinforcement

The design parameters which make SiC the primary choice as a matrix material also drive

its viability as a reinforcement material. Process research and improvement have advanced

ceramic fibers from single crystal carbon whiskers to continuous SiC fibers to the advanced Hi-Nicalon fibers used to produce the CMC studied in this work.

The primary production method for monofilament SiC fibers such as SCS-6 is Chemical Vapor Deposition (CVD). While the chemical reaction for CVD is identical to the CVI reaction used to produce SiC matrices, the production of fibers happens in a long heat reactor, and the SiC material is deposited on a substrate core drawn through the reactor. Original SiC fibers produced by CVD used a tungsten core. The resulting fibers had diameters on the order of 100-150μm. Bend radii of about 7mm limited the shapes which these fibers could form. Another limitation was operational temperature; at ~800^{0}C the tungsten reacted with the SiC degrading fiber strength [2:464].

In the 1970's, work began on alternate production methods for SiC fibers, ultimately leading to the polymer pyrolysis process for producing Nicalon fibers. Polymer Pyrolysis is a multi-step process consisting of synthesizing a spinnable polymer, spinning a precursor fiber, crosslinking the fiber through curing so it won't melt during pyrolysis, then pyrolyzing the fiber into a ceramic. Since there was no substrate core, this process produced fibers of solid Nicalon. These fibers had higher operating temperatures than the SiC fiber produced via the CVD process. Also, the Nicalon fibers produced by the PIP had smaller diameters than earlier fibers, giving them a tighter bend radius thus making it easier to form then into smaller, more compact shapes. The flow diagram of this process is shown in Figure 6.
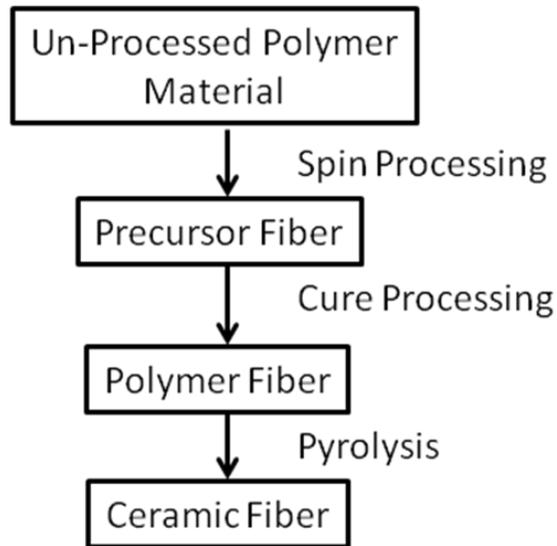
Figure 6: Flow diagram for making ceramic fibers from a polymeric precursor.

Early Nicalon fibers had Oxygen contents around 12%, limiting their working temperature to below 1200 ^{0}C. Refinements in production practices including radiation curing via an electron beam in a Helium environment reduced the Oxygen content and produced Hi-Nicalon fibers. The Oxygen content of Hi-Nicalon fibers is only 0.5%, greatly increasing the fiber's thermal stability and creep resistance. The following table compares properties of Hi-Nicalon fibers with those of other ceramic fibers.

Table 2: Properties of Hi-Nicalon fiber reinforcement and other common ceramic fibers [2:465].

Fiber	Composition	Tensile Strength (ksi)	Tensile Modulus (msi)	Density (g/cm^3)	Diameter (mil)	Critical Bend Radii (mm)
SCS-6	SiC on C Monofilament	620	62	3.00	5.5	7.0
Nextel 312	62Al$_2$O$_3$-14B$_2$O$_3$-15SiO$_2$	250	22	2.7	0.4	0.48
Nextel 440	70Al$_2$O$_3$-2B$_2$O$_3$-28SiO$_2$	300	27	3.05	0.4–0.5	–
Nextel 480	70Al$_2$O$_3$-2B$_2$O$_3$-28SiO$_2$	330	32	3.05	0.4–0.5	–
Nextel 550	73Al$_2$O$_3$-27SiO$_2$	290	28	3.03	0.4–0.5	0.48
Nextel 610	99 α-Al$_2$O$_3$	425	54	3.88	0.6	–
Nextel 720	85Al$_2$O$_3$-15SiO$_2$	300	38	3.4	0.4–0.5	–
Almax	99 α-Al$_2$O$_3$	260	30	3.60	0.4	–
Altex	85Al$_2$O$_3$-15SiO$_2$	290	28	3.20	0.6	0.53
Nicalon NL200	57Si-31C-12O	435	32	2.55	0.6	0.36
Hi-Nicalon	62Si-32C-0.5O	400	39	2.74	0.6	–
Hi-Nicalon-S	68.9Si-30.9C-0.2O	375	61	3.10	0.5	–
Tyranno LOX M	55.4Si-32.4C-10.2O-2Ti	480	27	2.48	0.4	0.27
Tyranno ZM	55.3Si-33.9C-9.8O-1Zr	480	28	2.48	0.4	–
Sylramic	66.6Si-28.5C-2.3B-2.1Ti-0.8O-0.4N	465	55	3.00	0.4	–
Tonen Si$_3$N$_4$	58Si-37N-4O	360	36	2.50	0.4	0.80

2.1.3 Interphase Material

Interphase coatings are often required to 1) protect the fibers from degradation during high temperature processing, 2) aid in slowing oxidation during service, and 3) provide the weak fiber-to-matrix bond required for toughness [2:470]. The interphase material of the CMC studied in this effort is Boron Nitride (BN). Several features of BN make it the primary interphase choice for the advanced SiC/SiC CMC studied in this research.

To start, the CVD apparatus used to produce the SiC matrix material can first be used to deposit a thin, ~0.25µm, layer of BN on the Hi-Nicalon fiber. This reduces processing time and cost in an already lengthy and expensive production process.

The second advantage of BN is its crystalline structure. Through careful control of the BN CVD process, the interphase layer will be of α-BN, which has a hexagonal, layered structure.
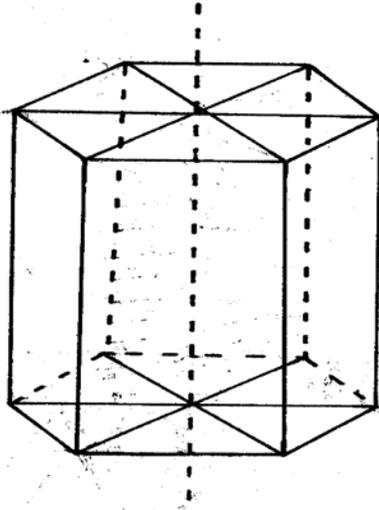
Figure 7: Hexagonal close-packed α-BN crystal structure.

This hexagonal structure easily undergoes cleavage under loading making it a mechanical lubricant [3:37]. Hexagonal BN is sometime referred to as White Graphite. This lubricating effect weakens the bond between the Hi-Nicalon fibers and the SiC matrix, producing the toughness desired in the final CMC.

Finally, BN can provide a minor degree of protection for the Hi-Nicalon fibers. For example, while both Hi-Nicalon fibers and SiC matrix are conductive material, BN is an insulator [3:37]. Unfortunately, BN degrades in ambient environments. Without protection, this degradation is accelerated in aggressive environments such as high temperature oxygenated atmospheres and water vapor [3:37]. Accordingly, these are the test environments for this Hi-Nicalon/BN/SiC CMC study.

2.1.4 Lamina Geometry

As reported by the CMC manufacturer, the Hi-Nicalon/BN/SiC CMC consisted of 8, $[0^0/90^0]$ layers woven in an 8-harness-satin weave. The composite lay-up was symmetric about the midplane with warp and fill plies alternated.

By definition, a ply, or lamina, is a single layer of reinforcement material within a composite structure. The overall structure with its total number of plies is termed the laminate [4:26]. The plies in this case were woven preforms, meaning they had a defined structure before being processed into the final CMC. The orientation of the preforms was [0^0/90^0], meaning the bundles of fibers woven into the preform fabric were perpendicular to each other. This is a two dimensional (2-D) woven fabric, intended to withstand in-plane loading in two orthogonal direction, x- and y-, respectively.

The preform fabric was woven in an eight-harness-satin (8HS) weave (8HSW). Woven fabrics contain warp, lengthwise bundles of fibers, and weft, transverse bundles of fiber. As seen in the weave comparison below, in an 8HS weave, each warp interlaces with the eighth weft. Each [0^0/90^0] weave pattern will have a slight variation in strength arising from the different number of warp/weft overlays. In production, however, the main factor in choosing a weave pattern is the fabric formability. Weaves with higher harness-satin counts are usually more flexible and can form parts with tighter corner radii than plane or twill weaves. For the Hi-Nicalon/BN/SiC CMC this is not an issue since the parent panels are flat and the test specimens were loaded along one axis only.
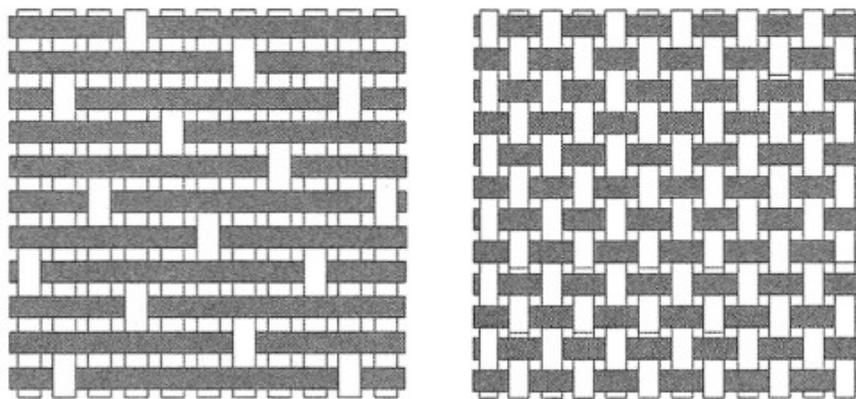
Figure 8: Comparison of eight-harness-satin (8HS) to plain weave.

The comment that the composite lay-up was symmetric about a midplane refers to fairly standard composite manufacturing technique. A laminate's midplane splits the laminate into two halves of identical thickness, so there were 4 plies above and 4 plies below the midplane in the test Hi-Nicalon/BN/SiC. A laminate is called symmetric when for each layer on one side of the midplane there is a corresponding layer at an equal distance on the other side of the midplane with identical thickness, orientation, and properties [4:167]. While woven plies can be stacked so fibers run at various orientations to tailor the properties of the final laminate, in the test material the warp bundles in every ply ran at 0^0, and the weft bundles ran at 90^0.

2.2 Test Specimen Preparation

Bomas Machine Specialties, Inc. used diamond grinding to "cut" the parent panels into standard AFIT tensile test specimens according to the specifications shown in Figure 9. To prevent fraying of the test specimen edges during machining, the parent material was sandwiched between pieces of sacrificial material. Following machining, the test specimens were returned to the manufacturer for a seal coating through an additional SiC CVI treatment. Prior to testing, fiberglass tabs were glued onto both sides of each end of the test specimens to protect the ends from being crushed by the hydraulic grips of the test machine. Throughout machining, sealing, and testing, strict documentation and control ensured traceability of each test specimen back to its parent panel. A specimen ready for testing is shown in Figure 10.
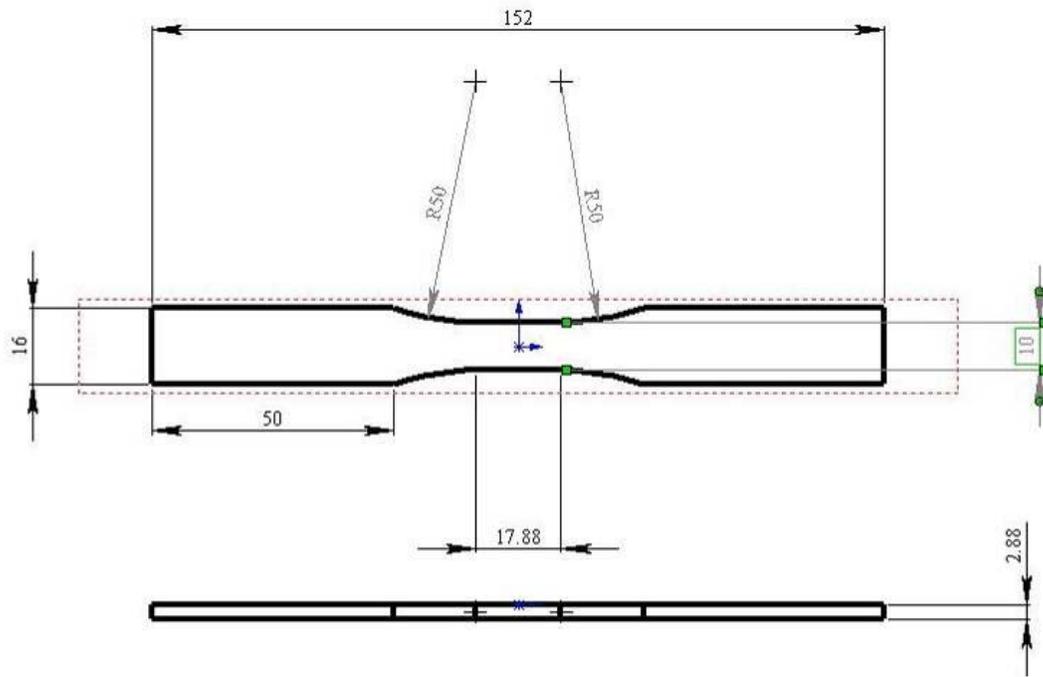
Figure 9: Test specimen. Dimensions in mm.

Figure 10: Hi-Nicalon/BN/SiC test specimen.

III. Experimental Arrangements and Procedures

3.1 Test Equipment

Testing of the Hi-Nicalon/BN/SiC employed several pieces of equipment in AFIT's

mechanical testing laboratory. The primary testing machine was the Material Test Systems

(MTS) vertical servo hydraulic test stand with a 25 kN (5.5 kip) load cell, hereafter referred to as

the 5 kip machine. Test specimens were mounted into the 5 kip machine via MTS 647 hydraulic,

water cooled, wedge grips. Grip pressure was set to 8 MPa. This grip pressure was high enough

to prevent slipping during the tests yet low enough not to crush the specimens. Machine

alignment was maintained with an MTS 609 alignment fixture. Figure 11 shows the 5 kip

machine.

Figure 11: MTS 5 kip vertical servo hydraulic test stand.

An MTS FlexTest 40 digital controller was used for input signal generation and data

acquisition. The use of MTS MultiPurpose Test Ware (MPTW) permitted user-defined test

histories which specified the desired test events, including applied forces, displacements, temperatures, cyclic or monotonic loading, and event detection, and enabled various modes of data collection.

An MTS Model 632.53 E-14 uniaxial low contact force, high temperature extensometer was employed for strain measurement. The gauge section of the extensometer was 12.7mm. The extensometer is shown in Figure 12.
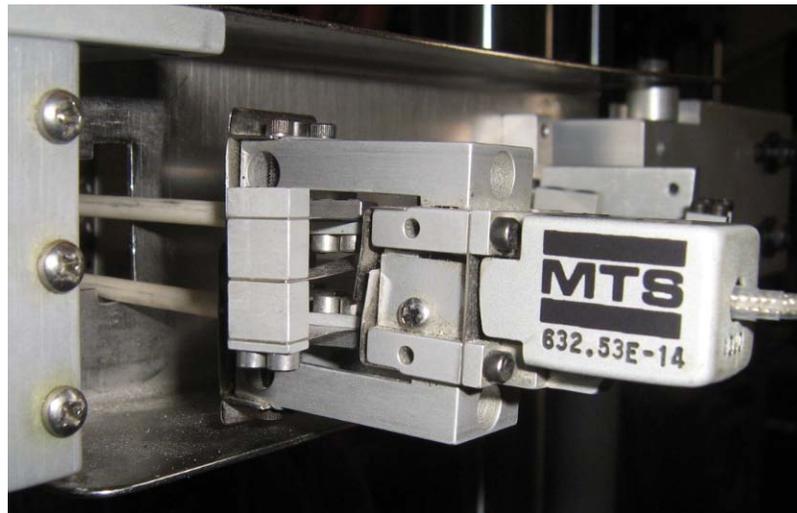
Figure 12: MTS uniaxial low contact force, high temperature extensometer.

Tests were performed at 1200 $^{\circ}$C in laboratory air and in steam environments. An AMTECO Hot Rail two zone furnace system, shown in Figure 13, and an MTS 409 temperature controller were used for elevated temperature testing.

(a)   (b)
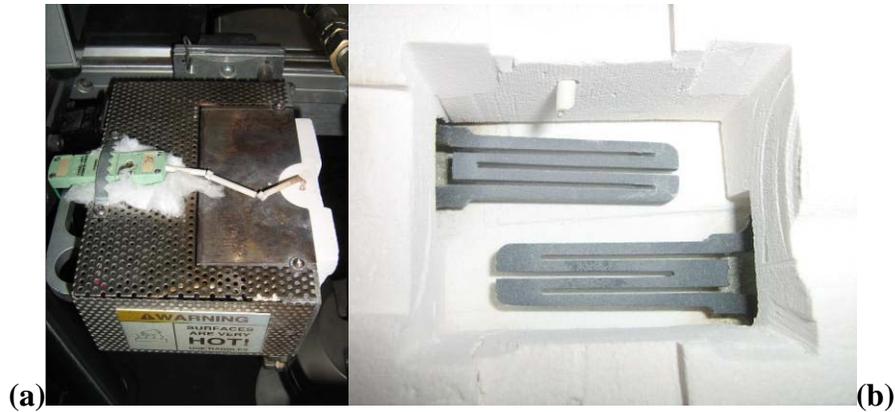
Figure 13: AMTECO Hot Rail Furnace (a) exterior and (b) interior.

Tests in steam employed an alumina susceptor (a tube with end caps), which fits inside

the furnace. The specimen gage section fits inside the susceptor with the grips ends of the

specimens passing through slots in the susceptor. Steam was generated by an AMTECO Steam

Generator and introduced into the susceptor in a continuous stream with a slightly positive

pressure creating a near 100% steam environment inside the susceptor (Figure 14). Cooling

water held at 15°C by a NESLAB Coolflow Model HX-75 refrigerated re-circulator and pumped

through the wedge grips protected them from the heat of the furnace during testing.
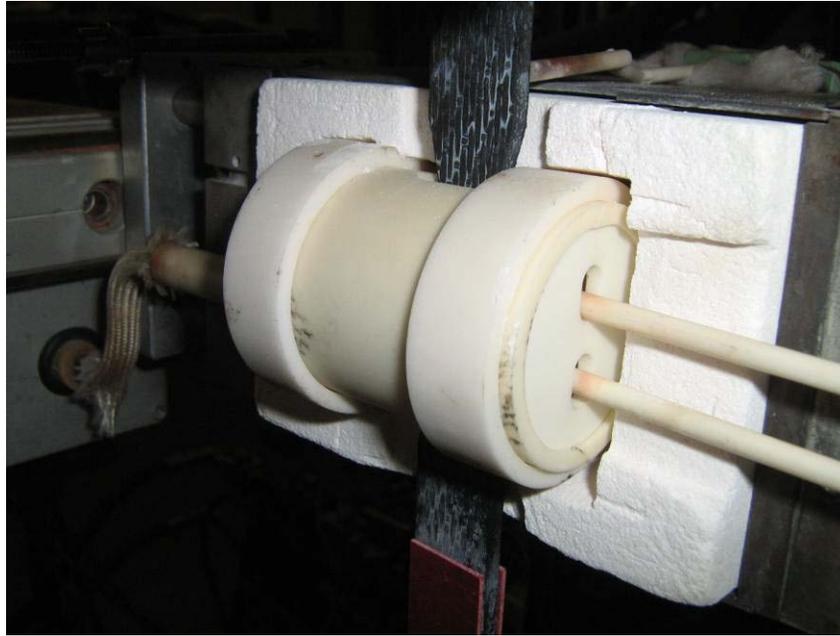
Figure 14: Test specimen mounted in Alumina susceptor.

3.1.1 Equipment Preparation

Prior to any MTS work, the 5 kip machine was warmed up to ensure proper hydraulic fluid operating temperature. Warm up consisted of using the MTS function generator to give the machine a 0.25in magnitude sine waveform input displacement command at 1 Hz for 30 minutes. During warm up, the HX-75 was turned on to chill the water for cooling the wedge grips. The cooling air for the extensometer was also turned on.

Prior to testing, the 5 kip machine was tuned to ensure the forces applied to the specimen matched the force command. Of course, it is impossible for the hydraulic mechanism of the 5 kip machine to respond instantaneously or with absolute precision to the controller input commanded by the MPTW. However, proper tuning minimized the lag and overshoot between the controller commands and the machine response.

Temperature calibration required a separate process. During temperature calibration, a test specimen was instrumented with two R-Type thermocouples mounted in the 5 kip machine

22

under load control with a load command of 0 lb, and the furnace was closed around the specimen. The temperature was slowly raised manually and an Omega CL3515A digital, hand held thermometer displayed the actual temperature of the specimen via two attached thermocouples. Once the thermocouples on both the left and right side of the specimen reached the desired 1200 ^{o}C test temperature the temperature command to each half of the oven was recorded as the temperature set point. The system was then allowed to cool and a verification procedure written. Verification consisted of commanding each furnace half to ramp up to its temperature set point at a constant rate then maintaining that temperature for two hours to ensure the specimen stabilized thermally. During the two hour hold period specimen temperature was checked periodically to ensure the commanded temperature was maintaining a constant specimen temperature of 1200 ^{o}C. After the temperature calibration in air was complete, the specimen was removed from the wedge grips, enclosed in the susceptor, and remounted in the 5 kip machine. With the steam generator supplying steam into the susceptor, the temperature calibration procedure was repeated to find the temperature set points in steam.

3.2 Microstructural Characterization

Prior to testing, virgin material left over from machining each parent panel was cut and prepared for observation under the scanning electron microscope (SEM). SEM samples were cut such that faces perpendicular and parallel to the loading axis could be examined. The cut pieces were mounted into phenolic pucks using a Buehler specimen preparation machine. The samples were then polished on a Buehler AutoMet Specimen polisher using progressively finer Metadi Diamond Suspension polishing fluids. The complete process is outlined in Table 3 below.

Table 3: SEM sample polishing process.

Polishing Media Grit Size	Polishing Pressure (lbs)	Polishing Time (min)
400	6	10
600	6	10
45 µm	4	8
30 µm	4	8
15 µm	4	8
6 µm	3	6
3 µm	3	6
1 µm	3	6
¼ µm	1	4

After testing, the failed samples were examined under 1) a Zeiss Stemi SV II optical microscope equipped with a Zeiss AxioCam HRc digital camera (Figure 15)

Figure 15: Zeiss Stemi SV II optical microscope with a Zeiss AxioCam HRc digital camera.

And 2) the Quanta 200 scanning electron microscope (Figure 16).

Figure 16: Quanta 200 Scanning Electron Microscope.

The failed specimens were cut ~4mm behind the fracture surface, and then the fracture surface was mounted on a metallic SEM sample tab. Viewing these specimens at progressively tighter magnifications allowed analysis and characterization of the fracture surface.

A second cut was made at ~4mm behind the first cut. This slice was mounted in a phenolic puck and polished as described above to characterize any microstructural damage sustained during cyclic fatigue loading.

3.3 Test Procedures

3.3.1 Monotonic Tensile Test

A monotonic tensile test provided the baseline material properties for the Hi-Nicalon/BN/SiC composite. The test specimens were heated under a zero load command at a rate of 1 ^{0}C/sec to 1200 ^{0}C then held for 20 minutes at 1200 ^{0}C. Data recorded at 0.1 sec intervals during the heating and dwell period included strain, load, load command, oven temperature, displacement, and time. After the dwell period, the specimen was loaded at a constant rate of 0.05mm.sec until failure.

25

3.3.2 Fatigue Tests

Tension-tension fatigue tests with an R ratio (ratio of minimum stress to maximum stress) of 0.1 were conducted in load control at frequencies of 0.1 Hz, 1.0 Hz, and 10 Hz in both laboratory air and in steam environments. Fatigue run-out was defined as 10^5 cycles at 0.1 Hz and as 2 x 10^5 cycles at 1.0 Hz and 10 Hz. In all tests, the specimen was heated under a zero load command at a rate of 1 ^{0}C/sec to 1200 ^{0}C, then the specimens tested in air were held at 1200 ^{0}C for 20 minutes and the specimens tested in steam were held at 1200 ^{0}C for 25 minutes. Before the cyclic loading began, the load was raised to the minimum stress level in 20 seconds. Once this minimum load level was reached the specimen was subjected to cyclic loading. Data collected during the test included strain, load, load command, displacement, cycle number, temperature and time. "Peak and valley" data were taken for every cycle. Full cycle data was taken for the following cycles: i) cycles 1 to 25, ii) every tenth cycle between cycles 30 and 100, iii) every 100th cycle between cycles 100 and 1000, iv) every 1000th cycle between cycles 1000 and 10000, and v) every 10000th cycle between cycles 10000 and run-out. Figure 17 shows a typical test procedure.
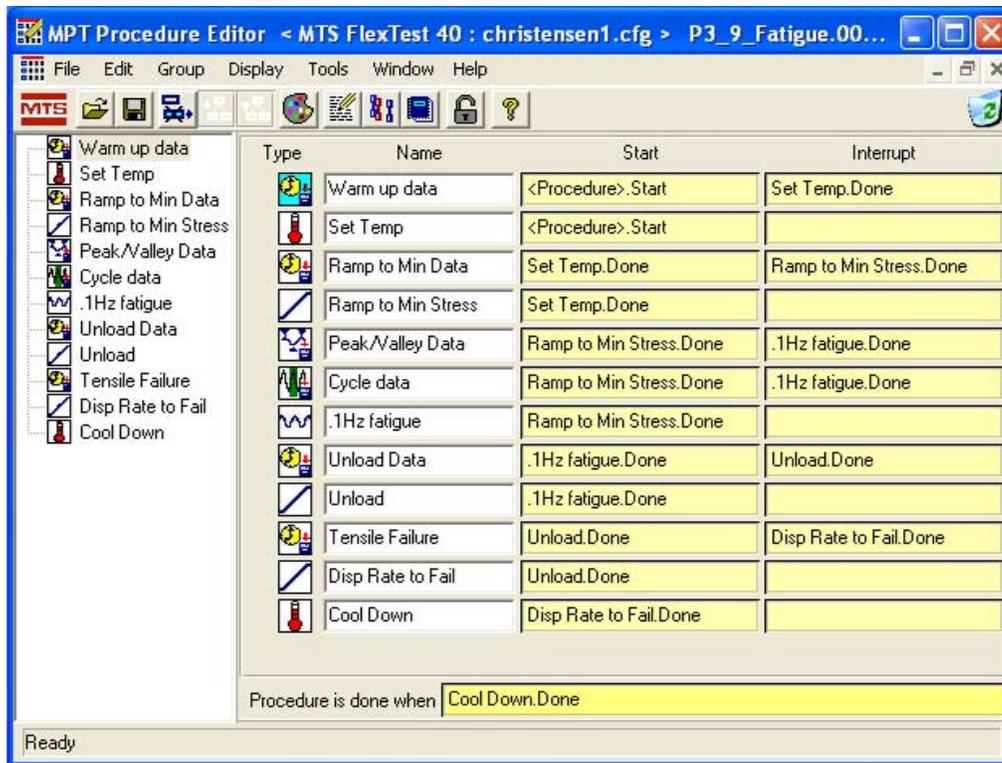
Figure 17: MTS FlexTest 40 fatigue test procedure.

Every specimen that achieved run-out was kept at 1200 ^{0}C and unloaded to zero load in

30 seconds. The specimens were then subjected to a tensile test to failure according to the

procedure in section 3.3.1 to determine the retained properties.

IV. Results and Discussion

4.1 Chapter Overview

The following chapter discusses results of all tests.   Section 4.2 presents results of the monotonic tensile tests to failure performed on as-processed specimens to determine tensile properties. Section 4.3 gives the results of the tension-tension fatigue tests performed in laboratory air. Section 4.4 discusses the results of the tension-tension fatigue tests conducted in steam. Section 4.5 discusses the results of the tensile tests on fatigued specimen to determine retained tensile properties. Section 4.6 presents microstructural analysis.

All tests were performed at 1200 ^{0}C. Fatigue testing was conducted with a ratio of minimum to maximum stress of R = 0.1. Fatigue run-out was set to 2 x 10^{5} cycles for tests conducted at 1.0 Hz and 10 Hz, and to 10^{5} cycles for tests performed at 0.1 Hz. Specimens were named so the first two characters indicate the original panel from which the specimen was cut and the last character indicates the specimen number from that panel, so P1-3 would be the third specimen from panel 1. Table 4 below shows all tests performed.

Table 4: Summary of Hi-Nicalon/BN/SiC specimen data. All tests conducted at 1200 ^{0}C.

Specimen	Fatigue Frequency (Hz)	Test Environment	Maximum Stress (MPa)	Elastic Modulus (GPa)	Cycles to Failure (N)	Time to Failure (h)	Failure Strain (%)
Tensile Tests							
P1-2[a]	-	Air	-	-	-	-	-
P1-3	-	Air	-	228.8	-	-	0.26
P2-4	-	Air	-	246.8	-	-	0.31
P3-1	-	Air	-	263.9	-	-	0.18
Tension-Tension Fatigue Tests							
P3-5	0.1	Air	120	335.6	2092	5.81	0.15
P2-6	0.1	Air	120	338	3780	10.5	0.058
P2-8	0.1	Air	110	322.9	100,000[b]	277.78	0.746
P2-7	0.1	Air	100	344.5	100,000[b]	277.78	0.384
P3-9	0.1	Steam	110	308.2	548	1.52	0.125
P3-8	0.1	Steam	100	352.1	13,726	38.13	0.131
P3-7	0.1	Steam	88	275.9	88,575[a]	246.04	0.159
P1-4	1	Air	120	232.4	3766	1.05	0.147
P1-8	1	Air	110	290.3	59,641	16.57	0.132
P1-6	1	Air	100	302.7	94,022	26.12	0.031
P1-7	1	Air	100	276.9	200,000[b]	55.56	0.496
P1-5	1	Air	80	268.1	200,000[b]	55.56	0.503
P1-9	1	Steam	110	302	5620	1.56	0.059
P2-1	1	Steam	100	N/A	1128	0.31	0.221
P2-3	1	Steam	100	N/A	1650	0.46	0.246
P1-1	1	Steam	100	283	11,447	3.18	0.674
P3-2	1	Steam	80	157.6	200,000[b]	55.56	0.395
P3-3	10	Air	100	330.1	96,721	2.69	0.085
P2-5	10	Air	80	438.7	200,000[b]	5.56	0.614
P3-4	10	Steam	80	194.6	33,451	0.93	0.05
P3-6	10	Steam	60	306	200,000[b]	5.56	0.305
Temperature Calibration Specimen							
P2-2	-	Both	-	-	-	-	-
Untested Specimen							
P2-9	-	-	-	-	-	-	-

[a] Failure of specimen did not occur when the test was terminated due to equipment malfunction.
[b] Run-out, failure of specimen did not occur when the test was terminated.

In each high-temperature test, thermal strain was calculated at the conclusion of the

heating stage. Thermal strain measurements were used to determine the linear thermal expansion

coefficient of the material. Thermal expansion results are summarized in Table 5, where test

temperature, corresponding thermal strain and coefficient of linear thermal expansion are

presented for each specimen tested. Expansion of the extensometer extension rods contributes to

the total measured strain, but it is expected that this contribution was negligible.

Table 5: Thermal expansion of Hi-Nicalon/BN/CVI SiC between 23^{0}C and 1200 ^{0}C.

Specimen	Thermal Strain (%)	Coefficient of Linear Thermal Expansion, α ($10^{-6}/^0$C)
P1-1	0.518	6.10
P1-3	0.530	6.24
P1-4	0.517	6.09
P1-5	0.510	6.00
P1-6	0.517	6.09
P1-7	0.510	6.00
P1-8	0.493	5.80
P1-9	0.500	5.89
Average		6.02
Standard Deviation		0.14
P2-1	0.610	7.18
P2-3	0.370	4.35
P2-4	0.552	6.50
P2-5	0.506	5.96
P2-6	0.500	5.89
P2-7	0.535	6.30
P2-8	0.527	6.20
Average		6.05
Standard Deviation		0.86
P3-1	0.533	6.27
P3-2	0.543	6.39
P3-3	0.502	5.91
P3-4	0.539	6.34
P3-5	0.503	5.92
P3-6	0.532	6.26
P3-7	0.480	5.65
P3-8	0.525	6.18
P3-9	0.526	6.19
Average		6.12
Standard Deviation		0.25

It is seen in Table 5 that specimens from all three panels produced similar values of the coefficient of thermal expansion, α, at 1200 °C. These coefficient of thermal expansion values are noticeably higher than the 3.5×10^{-6}/°C typically reported for Hi-Nicalon/SiC composites [22].

4.2 Monotonic Tension

Three specimens, one from each panel, were subjected to tensile tests to failure at 1200 °C. Test results are summarized in Table 6. The tensile stress–strain behavior is shown in Figure 18. The average ultimate tensile strength (UTS) was 217.0 MPa, the average elastic modulus was 246.5 GPa, and the average strain to failure was 0.25 %. The stress-strain curves are nearly linear up to the proportional limit. The average proportional limit was 110 MPa, which is ~ 55 % of the average UTS. At the proportional limit, the nonlinear behavior caused by matrix cracking occurs over a short strain range. After the "knee" in the stress-strain curve, the non-linear behavior appears to terminate, the stress-strain behavior becomes nearly linear and remains almost linear to failure.

It is seen in Figure 18 that the three specimens produced qualitatively similar stress-strain behavior. The minor differences in tensile properties produced by different specimens are within expected specimen-to-specimen and panel-to-panel scatter. However, statistically significant variations in tensile properties could not be determined because of the limited number of specimens.

Table 6: Tensile properties obtained for Hi-Nicalon/BN/SiC composite at 1200 ^{0}C in laboratory air at a constant displacement rate of 0.05mm/s.

Specimen	Elastic Modulus (GPa)	Proportional Limit (MPa)	UTS (MPa)	Failure Strain (%)
P1-3	228.8	110	217.1	0.26
P2-4	246.8	115	234.0	0.31
P3-1	263.9	105	199.8	0.18
Average	246.5	110	217.0	0.25
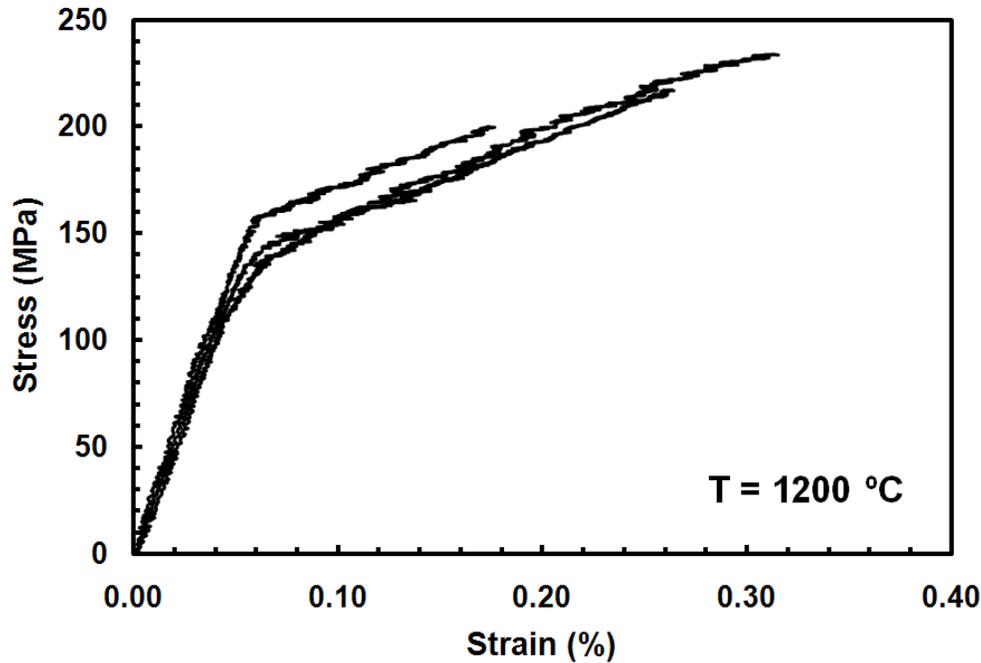
Figure 18: Tensile stress-strain curves for Hi-Nicalon/BN/SiC ceramic composite at 1200 °C in air.

4.3 Tension-Tension Fatigue at 1200 °C in Laboratory Air

Tension-tension fatigue tests were conducted at frequencies of 0.1 Hz, 1.0 Hz and 10 Hz at 1200 °C in laboratory air. Fatigue run-out was set to 2 x 10^5 cycles for the frequencies of 1.0 and 10 Hz and to 10^5 cycles for the frequency of 0.1 Hz. These run-out conditions approximate the number of loading cycles expected in aerospace applications at 1200 °C. Results are summarized in Table 7. Results are also presented in Figure 19 as the stress vs. cycles to failure curves (i.e. S-N curves) for the three frequencies.

Results in Table 7 and Figure 19 reveal that increasing the fatigue frequency by an order of magnitude resulted in decreasing fatigue limit. While the fatigue limit was 110 MPa for the frequency of 0.1 Hz, the fatigue limit for 1.0 Hz was a lower 100 MPa. For the frequency of 10

Hz the fatigue limit further decreased to 80 MPa. These fatigue limits are based on the run-out conditions specified above. It is recognized that a more rigorous run-out condition could have resulted in lower fatigue limits. Note that the fatigue limits produced at 1.0 Hz and 10 Hz are below the average proportional limit obtained in tensile tests. This indicates that at 1.0 Hz and 10 Hz the fatigue limit is less than the stress of matrix cracking. The fatigue limit obtained at 0.1 Hz is at a level equal to the stress of matrix cracking.

Table 7: Summary of fatigue results obtained for the Hi-Nicalon/BN/SiC composite at 1200 ^{0}C in laboratory air.

Test Environment	Max Stress (MPa)	Cycles to Failure	Time to Failure (h)	Failure Strain (%)
Fatigue at 0.1 Hz				
Laboratory Air	120	3780	10.5	0.058
Laboratory Air	120	2092	5.8	0.06
Laboratory Air	110	100,000 [b]	277.8 [b]	0.08
Laboratory Air	100	100,000 [b]	277.8 [b]	0.09
Fatigue at 1.0 Hz				
Laboratory Air	120	3766	1	0.03
Laboratory Air	110	59,641	16.6	0.02
Laboratory Air	100	94,022[a]	26.1	-
Laboratory Air	100	200,000 [b]	55.6 [b]	0.026
Laboratory Air	80	200,000 [b]	55.6 [b]	0.022
Fatigue at 10 Hz				
Laboratory Air	100	96,721	2.7	0.06
Laboratory Air	80	200,000 [b]	5.6 [b]	0.05

[a] Failure of specimen did not occur when the test was terminated due to equipment malfunction.
[b] Run-out, failure of specimen did not occur when the test was terminated.
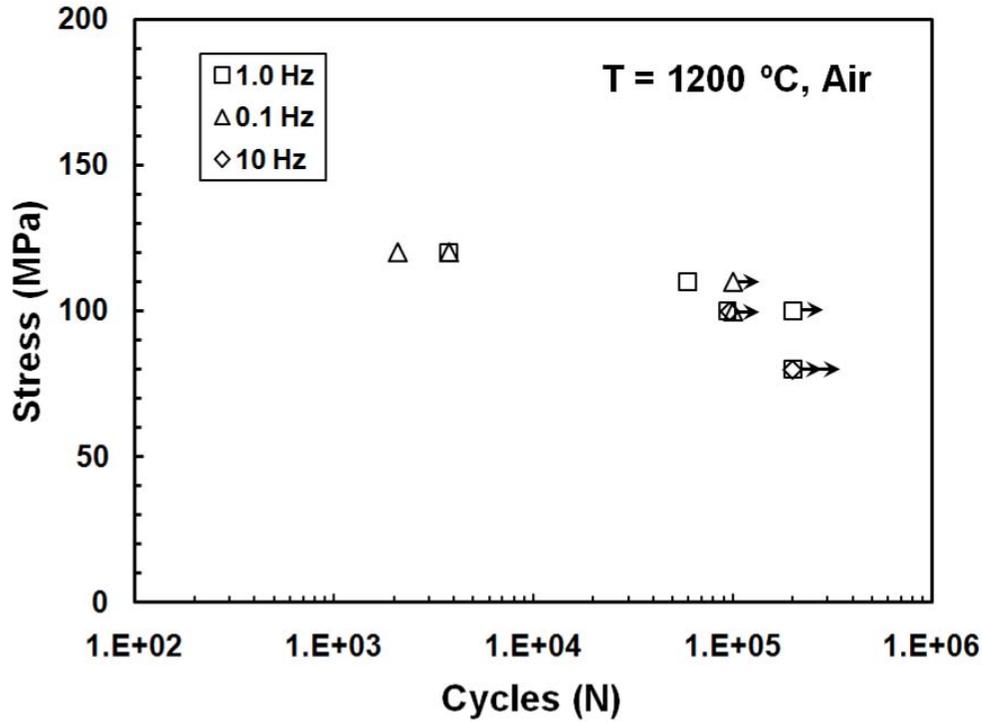
Figure 19: Fatigue stress vs. cycles to failure results (S-N curves) for Hi-Nicalon/BN/SiC ceramic composite at 1200 °C in laboratory air. Arrow indicates that failure of specimen did not occur when the test was terminated.

The fatigue data in Figure 19 can also be plotted as a function of time to failure (see Fig. 20). The results in Figure 20 and data in Table 7 show that, for a given stress level (consider, for example, 100 MPa), time to failure decreases with increasing frequency.
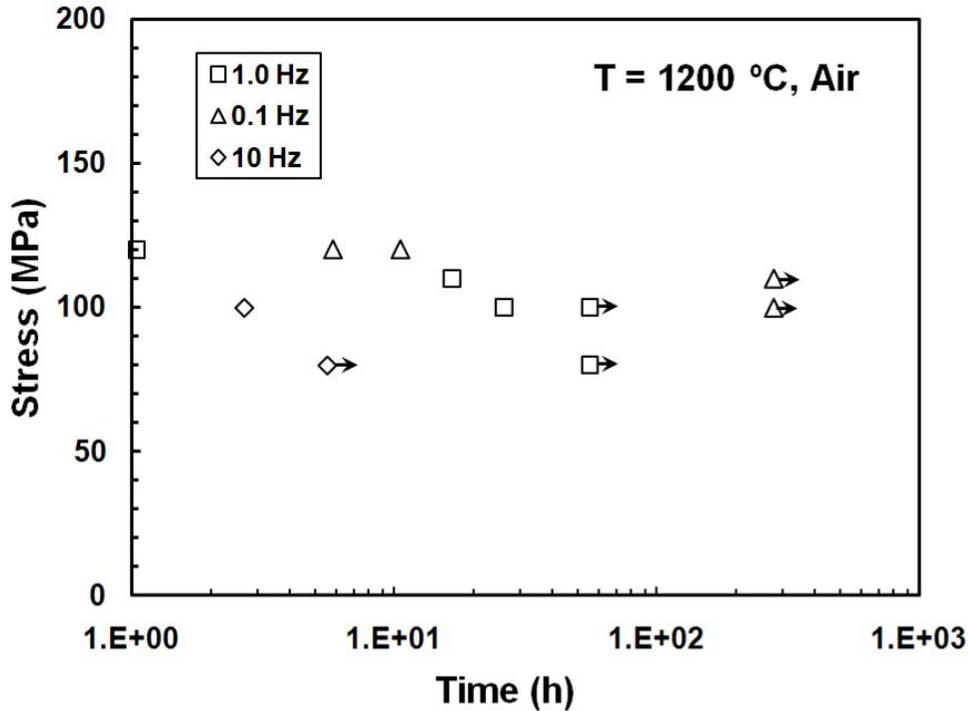
Figure 20: Fatigue stress vs. time to failure for Hi-Nicalon/BN/SiC ceramic composite at 1200 °C in laboratory air. Arrow indicates that failure of specimen did not occur when the test was terminated.

Of importance in cyclic fatigue is the reduction in stiffness (hysteresis modulus determined from the maximum and minimum stress-strain data points during a load cycle), which reflects the damage development during fatigue cycling. Modulus evolution with fatigue cycles is shown in Figure 21, where normalized modulus (i.e. modulus normalized by the modulus obtained in the first cycle) is plotted vs. fatigue cycles. It is noteworthy that although some tests achieved run-out, a decrease in normalized modulus with cycling was still observed. Contrary to expectations, modulus loss remained relatively independent of the fatigue stress level for all fatigue frequencies. Furthermore, the loading frequency also appears to have little effect on the modulus change with cycles. At 0.1 Hz the normalized modulus decreased by 22% in the 100 MPa test and by 26% in the 120 MPa test. At 1.0 Hz the normalized modulus decreased by

21% in the 80 MPa test and by 20% in the 120 MPa test. At 10 Hz the normalized modulus

decreased by 24% in the 80 MPa test and by 25% in the 100 MPa test. The modulus loss of 22%

observed in the 100 MPa test at 0.1 Hz is not significantly different from the 25% modulus loss

noted in the 100 MPa test at 10 Hz.
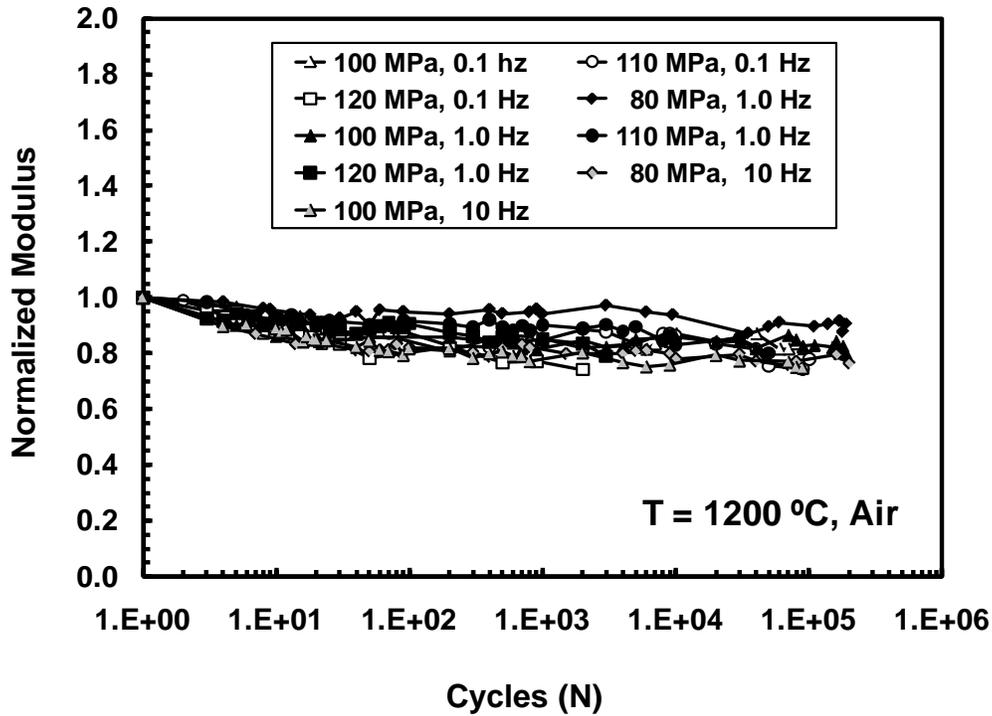
Figure 21: Normalized modulus vs. fatigue cycles for Hi-Nicalon/BN/SiC ceramic composite at 1200 °C in laboratory air.

Maximum cyclic strains as functions of fatigue cycles are presented in Figure 22. It is

seen that at 1200 °C in air continual strain accumulation with cycling occurs until failure or run-

out. The loading frequency does not appear to have a profound effect on the rate of strain

accumulation or on the accumulated strains. All strains accumulated in fatigue tests conducted at

1200 °C in air are below 0.1%.
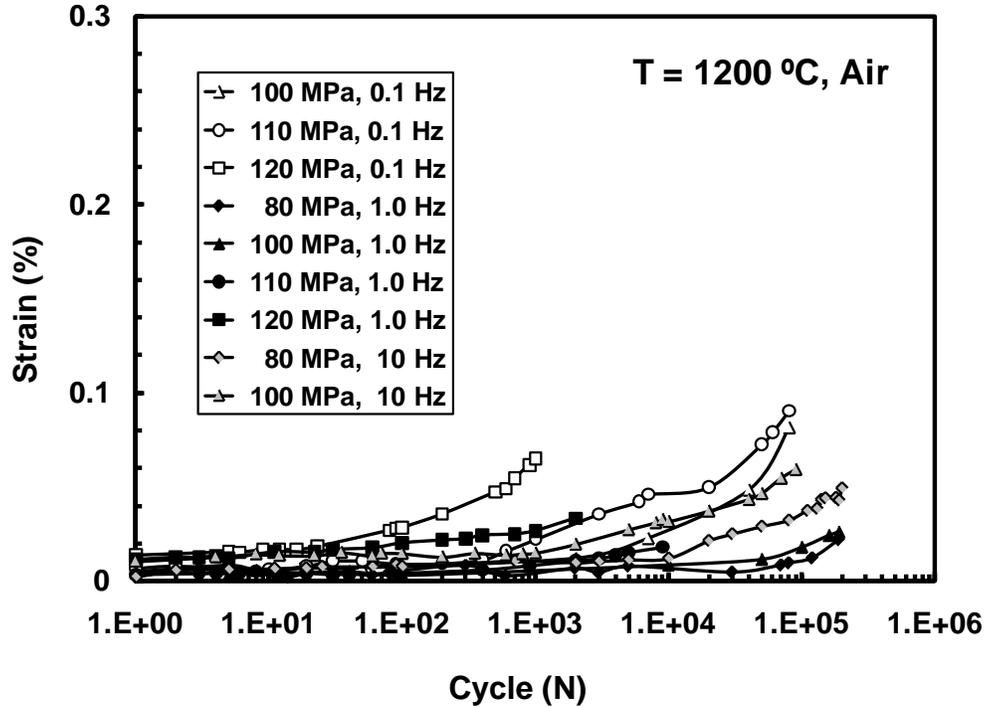
Figure 22: Maximum strain vs. fatigue cycles for Hi-Nicalon/BN/SiC ceramic composite at 1200 °C in laboratory air.

4.4 Tension-Tension Fatigue at 1200 °C in Steam

Tension-tension fatigue tests were conducted at frequencies of 0.1 Hz, 1.0 Hz and 10 Hz at 1200 °C in steam environment. Fatigue run-out was set to 2×10^5 cycles for the frequencies of 1.0 Hz and 10 Hz and to 10^5 cycles for the frequency of 0.1 Hz. Results are summarized in Table 8. Results are also presented in Figure 23 as the stress vs. cycles to failure curves (i.e. S-N curves) for the three frequencies. Results obtained in laboratory air are included in Table 8 and in Figure 23 for comparison.

Table 8: Summary of fatigue results obtained for the Hi-Nicalon/BN/SiC composite at 1200 ^{0}C in laboratory air and in steam environment

Test Environment	Max Stress (MPa)	Cycles to Failure	Time to Failure (h)	Failure Strain (%)
Fatigue at 0.1 Hz				
Laboratory Air	120	3780	10.5	0.058
Laboratory Air	120	2092	5.8	0.06
Laboratory Air	110	100,000 [b]	277.8 [b]	0.08
Laboratory Air	100	100,000 [b]	277.8 [b]	0.09
Steam	110	548	1.5	0.04
Steam	100	13,726	38.1	0.03
Steam	88	88575 [a]	246.0 [b]	0.065
Fatigue at 1.0 Hz				
Laboratory Air	120	3766	1	0.03
Laboratory Air	110	59,641	16.6	0.02
Laboratory Air	100	94,022[a]	26.1	-
Laboratory Air	100	200,000 [b]	55.6 [b]	0.026
Laboratory Air	80	200,000 [b]	55.6 [b]	0.022
Steam	110	5620	1.6	0.022
Steam	100	11,447	3.2	0.025
Steam	80	200,000 [b]	55.6 [b]	0.04
Fatigue at 10 Hz				
Laboratory Air	100	96,721	2.7	0.06
Laboratory Air	80	200,000 [b]	5.6 [b]	0.05
Steam	80	33,451	0.9	0.025
Steam	60	200,000 [b]	5.6 [b]	0.024

[a] Failure of specimen did not occur when the test was terminated due to equipment malfunction.
[b] Run-out, failure of specimen did not occur when the test was terminated.

Results in Table 8 and Figure 23 show that at all fatigue frequencies investigated the presence of steam causes severe degradation in fatigue performance. For the frequency of 0.1 Hz the reduction in cyclic life due to the presence of steam was 86% in the 100 MPa test and 99% in the 110 MPa test. While the fatigue limit at 0.1 Hz in air was 110 MPa, the fatigue limit in steam was below 90 MPa. At 1.0 Hz the cyclic lifetimes were reduced by >90% in tests with the maximum stress of 100 and 110 MPa. The fatigue limit obtained at 1.0 Hz in steam was only 80 MPa, noticeably lower than the fatigue limit of 100 MPa produced in air. At 10 Hz the cyclic

lifetime in the 80 MPa test was reduced by 83% due to the presence of steam. Furthermore, the fatigue limit at 10 Hz was reduced from 80 MPa to 60 MPa due to steam.

The effect of fatigue frequency on the fatigue performance in steam was no more pronounced than that observed in laboratory air. In steam, an increase in fatigue frequency by an order of magnitude also resulted in decreasing fatigue limit. At 1200 °C in steam, as the fatigue frequency increased from 0.1 Hz to 1.0 Hz, the fatigue limit decreased from ~90 MPa to 80 MPa. Likewise, as the fatigue frequency increased from 1.0 Hz to 10 Hz, the fatigue limit decreased from 80 MPa to 60 MPa.
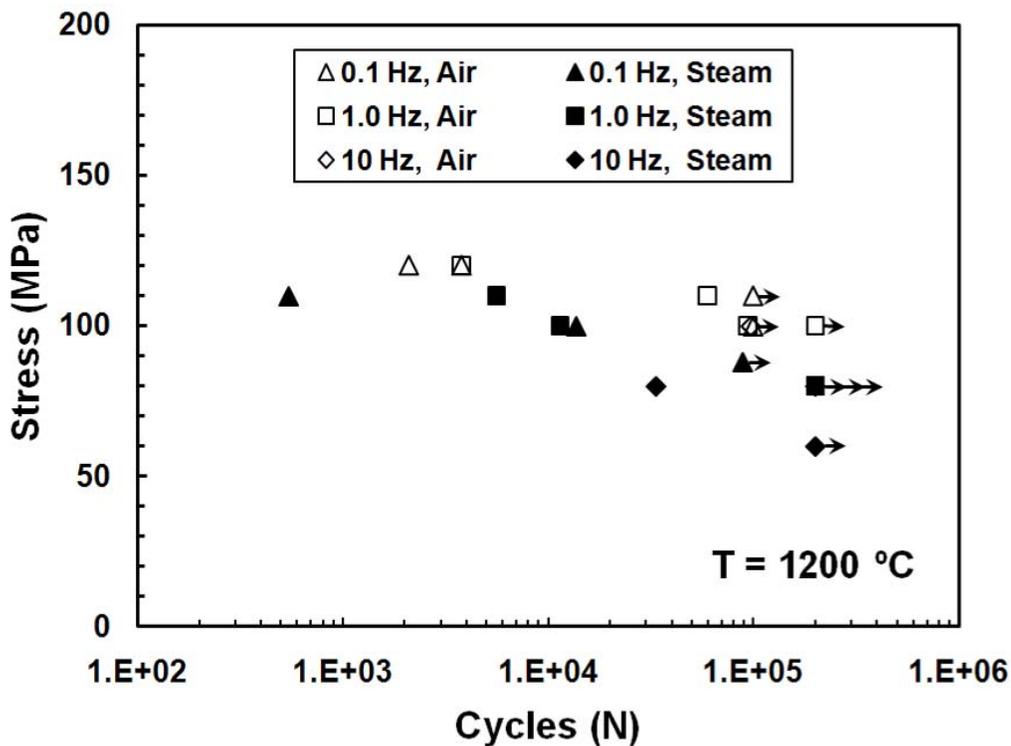
Figure 23: Fatigue stress vs. cycles to failure results (S-N curves) for Hi-Nicalon/BN/SiC ceramic composite at 1200 °C in laboratory air and in steam environment. Arrow indicates that failure of specimen did not occur when the test was terminated.

The fatigue data in Figure 23 obtained in steam were also plotted as a function of time to failure in Figure 24. The results in Figure 24 and data in Table 8 show that in steam, for a given stress level, time to failure decreases with increasing frequency.
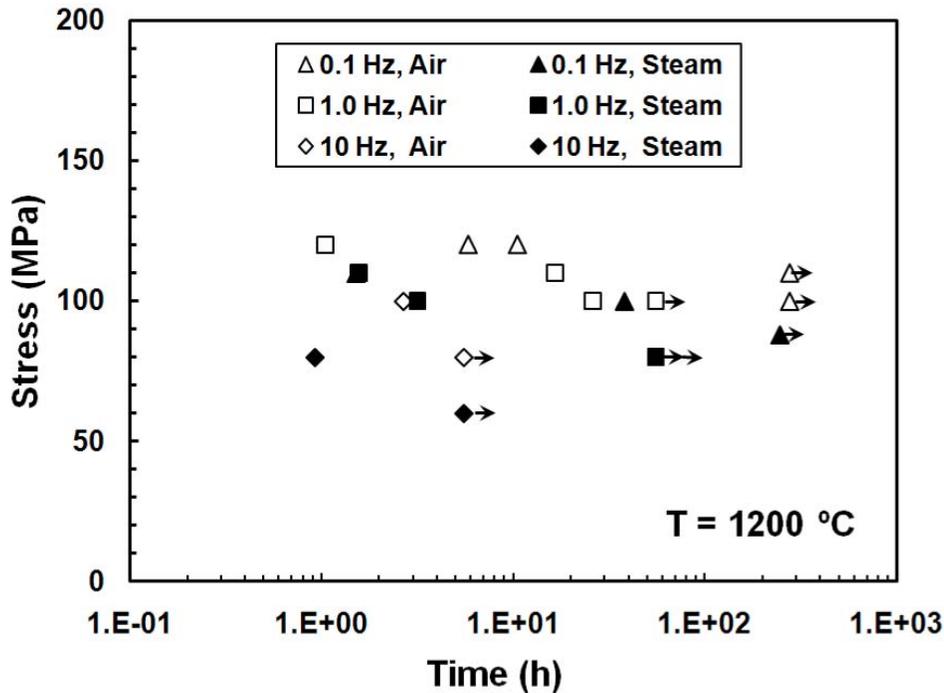
Figure 24: Fatigue stress vs. time to failure for Hi-Nicalon/BN/SiC ceramic composite at 1200 °C in laboratory air. Arrow indicates that failure of specimen did not occur when the test was terminated.

Change in hysteresis modulus (determined from the maximum and minimum stress-strain data points during a load cycle) with fatigue cycling at 1200 °C in steam was evaluated. Results are presented in Figure 25, where normalized modulus (i.e. modulus normalized by the modulus obtained in the first cycle) is plotted vs. fatigue cycles. A decrease in normalized modulus with cycling was observed in all tests conducted in steam. Changes in normalized modulus are somewhat more pronounced in steam. While at 1200 °C in air the modulus loss was limited to 26%, in steam modulus loss of 30% was observed in the 110 MPa test at 0.1 Hz. As in air environment, in steam the modulus change with cycles appears to be relatively independent of

40

the loading frequency. At 0.1 Hz in steam the normalized modulus decreased by 25% in the 88 MPa test and by 30% in the 110 MPa test. At 1.0 Hz in steam the normalized modulus decreased by 27% in the 100 MPa test and by 28% in the 110 MPa test. At 10 Hz in steam the normalized modulus decreased by 27% in the 60 MPa test and by 20% in the 80 MPa test. The modulus loss of 30% noted in the 110 MPa test at 0.1 Hz is close to the modulus loss of 28% recorded in the 110 MPa test at 1.0 Hz.
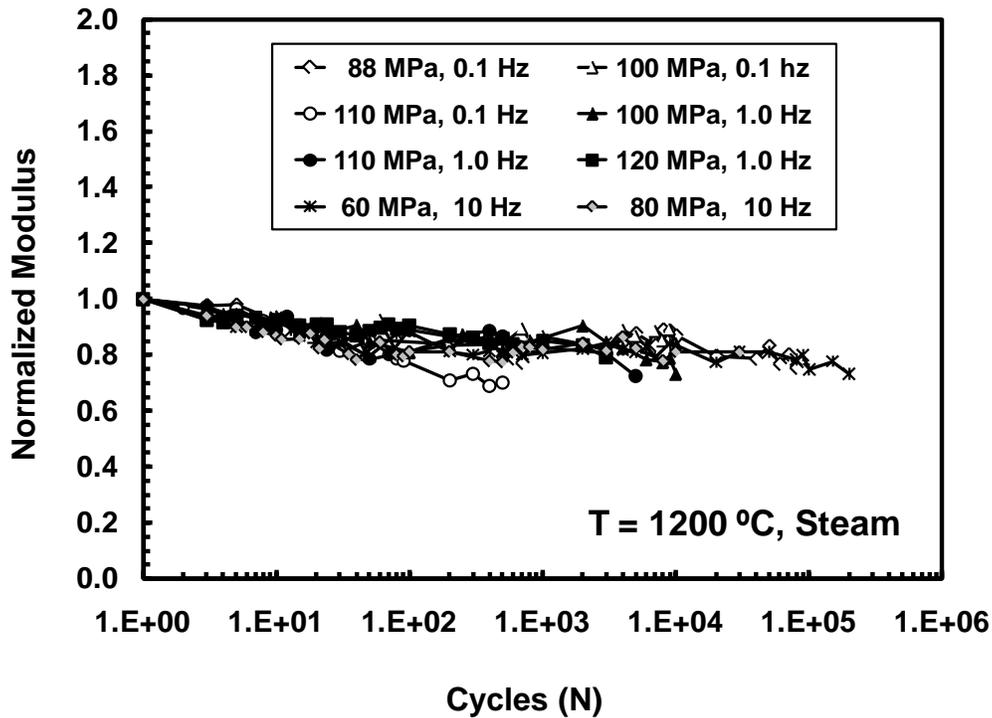
Figure 25: Normalized modulus vs. fatigue cycles for Hi-Nicalon/BN/SiC ceramic composite at 1200 °C in steam.
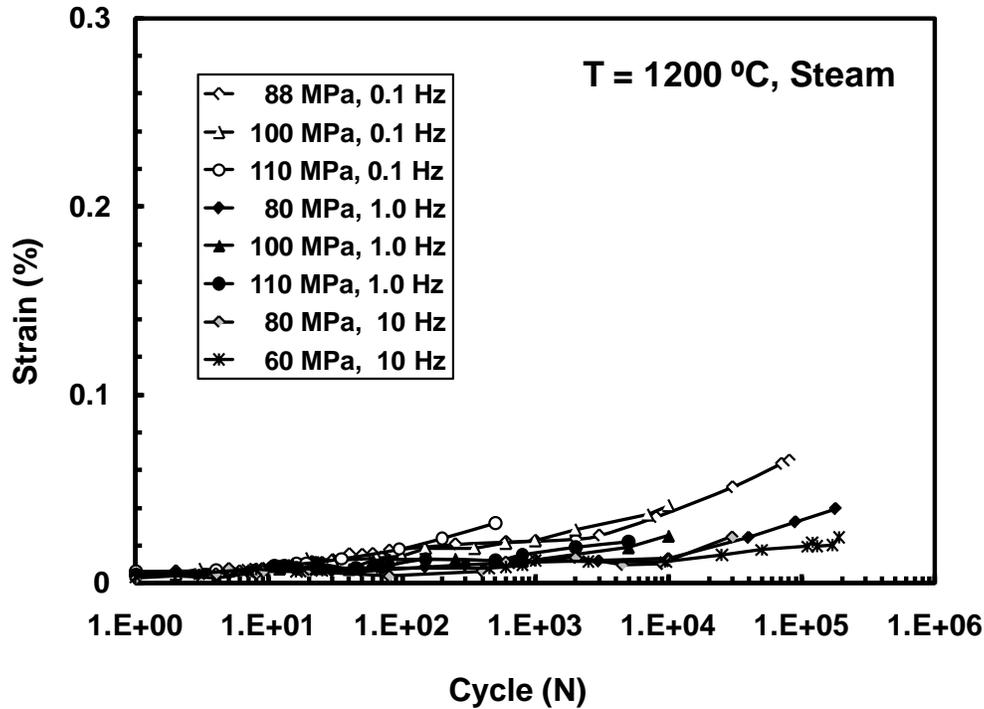
Figure 26: Maximum strain vs. fatigue cycles for Hi-Nicalon/BN/SiC ceramic composite at 1200 °C in steam.

Maximum cyclic strains produced at 1200 °C in steam are presented as functions of fatigue cycles in Figure 26. It is seen that the strains accumulated in steam are somewhat lower than those accumulated in air at the same fatigue stress and loading frequency. In steam, the largest strain (0.06%) was accumulated in the 88 MPa test conducted at 0.1 Hz. In air, the largest strain (0.09%) was accumulated in the 110 MPa test conducted at 0.1 Hz. Typically, lower strain accumulation with fatigue cycles indicates that less damage has occurred, and that it mostly limited to some additional matrix cracking. However, lower strains accumulated in steam generally correspond to shorter fatigue lifetimes. As in air, in steam the loading frequency does not have a strong effect on the rate of strain accumulation or on the accumulated strains.

4.5 Retained Tensile Properties

All specimens that achieved fatigue run-out were subjected to tensile tests to failure in order to measure the retained tensile properties. The tensile tests on run-out specimens were performed at 1200 ^{0}C in air. Retained strength and stiffness of the run-out specimens are summarized in Table 9.

Table 9: Retained properties of the Hi-Nicalon/BN/SiC specimens subjected to prior fatigue in laboratory air and in steam environment at 1200 °C.

Fatigue stress (MPa)	Fatigue environment	Retained strength (MPa)	Strength retention (%)	Retained modulus (GPa)	Modulus retention (%)	Strain at failure (%)
Prior fatigue at 0.1 Hz						
110	Air	242.5	≥100	248.5	≥100	0.384
100	Air	277.5	≥100	229.8	97.3	0.746
Prior fatigue at 1.0 Hz						
100	Air	248.2	≥100	208.3	88.2	0.496
80	Air	267.0	≥100	224.1	94.9	0.503
80	Steam	229.3	≥100	221.0	93.6	0.395
Prior fatigue at 10 Hz						
80	Air	257.9	≥100	273.8	≥100	0.614
60	Steam	205.3	94.6	211.4	89.5	0.305

It is seen that all specimens subjected to prior fatigue retained 100% of their tensile strength, irrespective of the fatigue stress level, test environment, or loading frequency. The only exception is seen in the case of the specimen subjected to prior fatigue at 10 Hz in steam, which retained only ~95% of its tensile strength.

Stiffness loss was observed in most cases. However, stiffness loss was limited to 12%. Stiffness degradation does not appear to depend on frequency of prior fatigue. Likewise, in the case of prior fatigue at 1.0 Hz the presence of steam does not have a pronounced effect on stiffness degradation. Conversely, in the case of prior fatigue at 10 Hz the presence of steam

results in greater degradation in strength and stiffness. Note that the discrepancy between the retained modulus of a run-out specimen and the decrease in modulus observed during fatigue testing most likely stems from different methods used to determine the retained and hysteresis moduli.

The tensile stress-strain curves produced by pre-fatigued specimens are compared to the tensile stress-strain curves obtained for the as-processed composite in Figures 27 and 28. The stress-strain curves obtained for the pre-fatigued specimens are qualitatively similar to those produced by the as-processed composite.
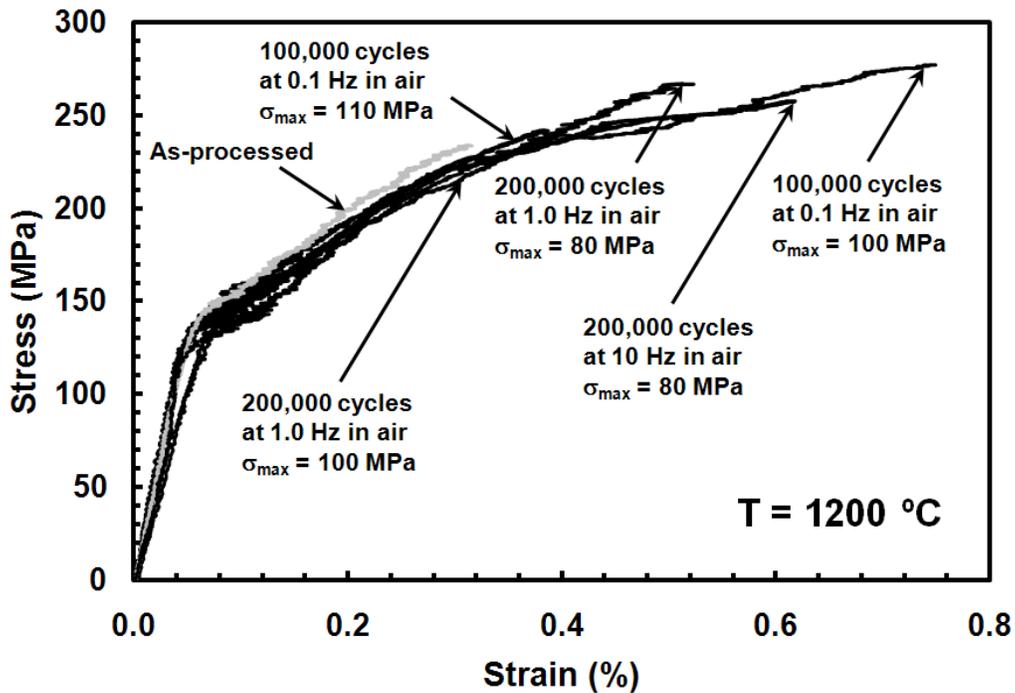
Figure 27: Stress-Strain response of Hi-Nicalon/BN/SiC specimens fatigued in air at 1200 °C then subjected to a monotonic tensile test to failure in laboratory air at 1200 °C at a displacement rate of 0.05mm/s.

44
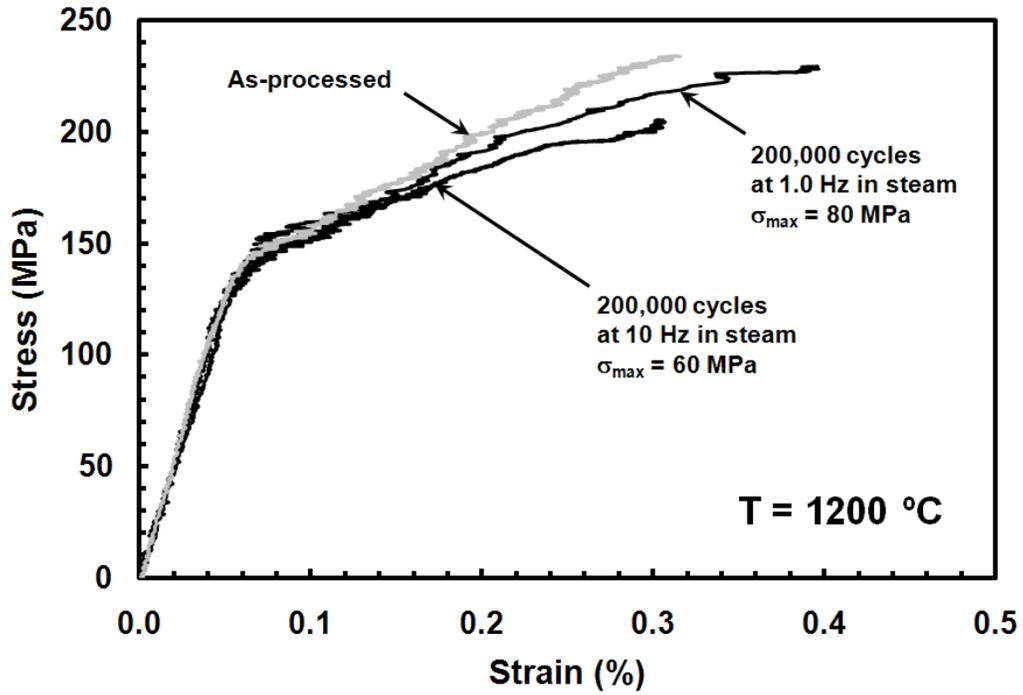
Figure 28: Stress-Strain response of Hi-Nicalon/BN/SiC specimens fatigued in steam at 1200 °C then subjected to a monotonic tensile test to failure in laboratory air at 1200 °C at a displacement rate of 0.05mm/s.

4.6 Microstructural Characterization

A qualitative analysis of the fracture surfaces of selected failed specimens and of the untested as-processed material was completed using both an optical microscope and a scanning electron microscope.

4.6.1 Microstructure of the As-Processed Material

Sections of material from the three composite panels were mounted and polished for viewing under the SEM. As seen in Figures 29-31, similar microstuctural features were present in all three parent panels. First, large voids were observed between adjacent plies (see Figure 29 (A)). Next, Figure 29 (B) shows smaller voids within the fiber tows of the woven fabric. Also seen in figure 29 B are the various fiber shapes and sizes. Since the BN fiber coating is quite soft and reacts with water, which was the base of the polishing fluids, it is most likely not present at the surface of these specimens; however, the space occupied by the BN layer is clearly visible and of uniform thickness, Figure 29 (C). Finally, a multi-step manufacturing technique produces a "flash" layer of SiC around the fibers, Figure 29 (D). Despite the difference in appearance, this "flash" layer is the same material and has the same properties as the rest of the SiC matrix densified by the CVI process.
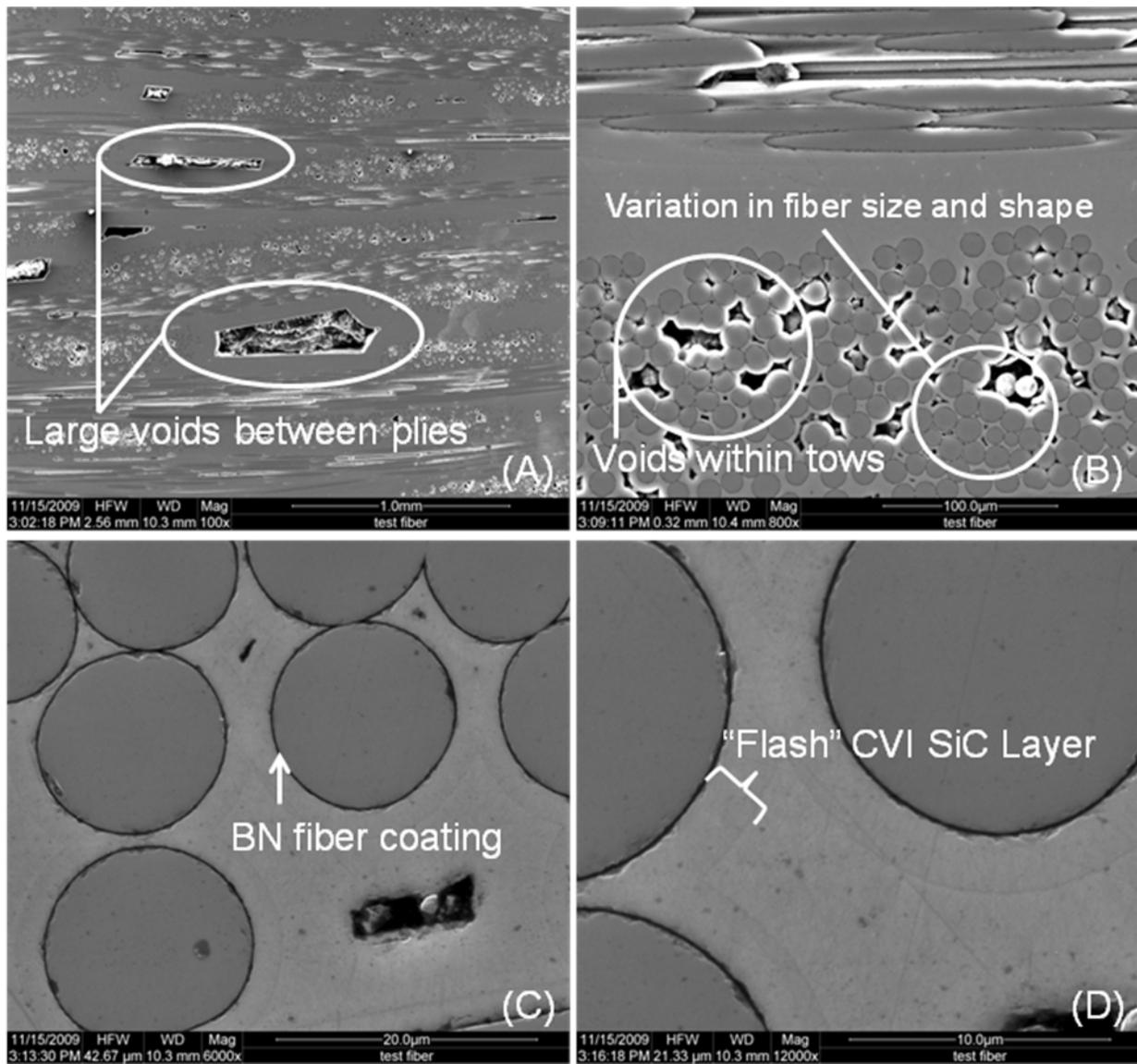
Figure 29: SEM micrographs of the as-processed material from Panel 1 showing A) voids between plies, B) voids within tows of the 8HS weave, C) the BN fiber coating and D) the "flash" CVI SiC layer.
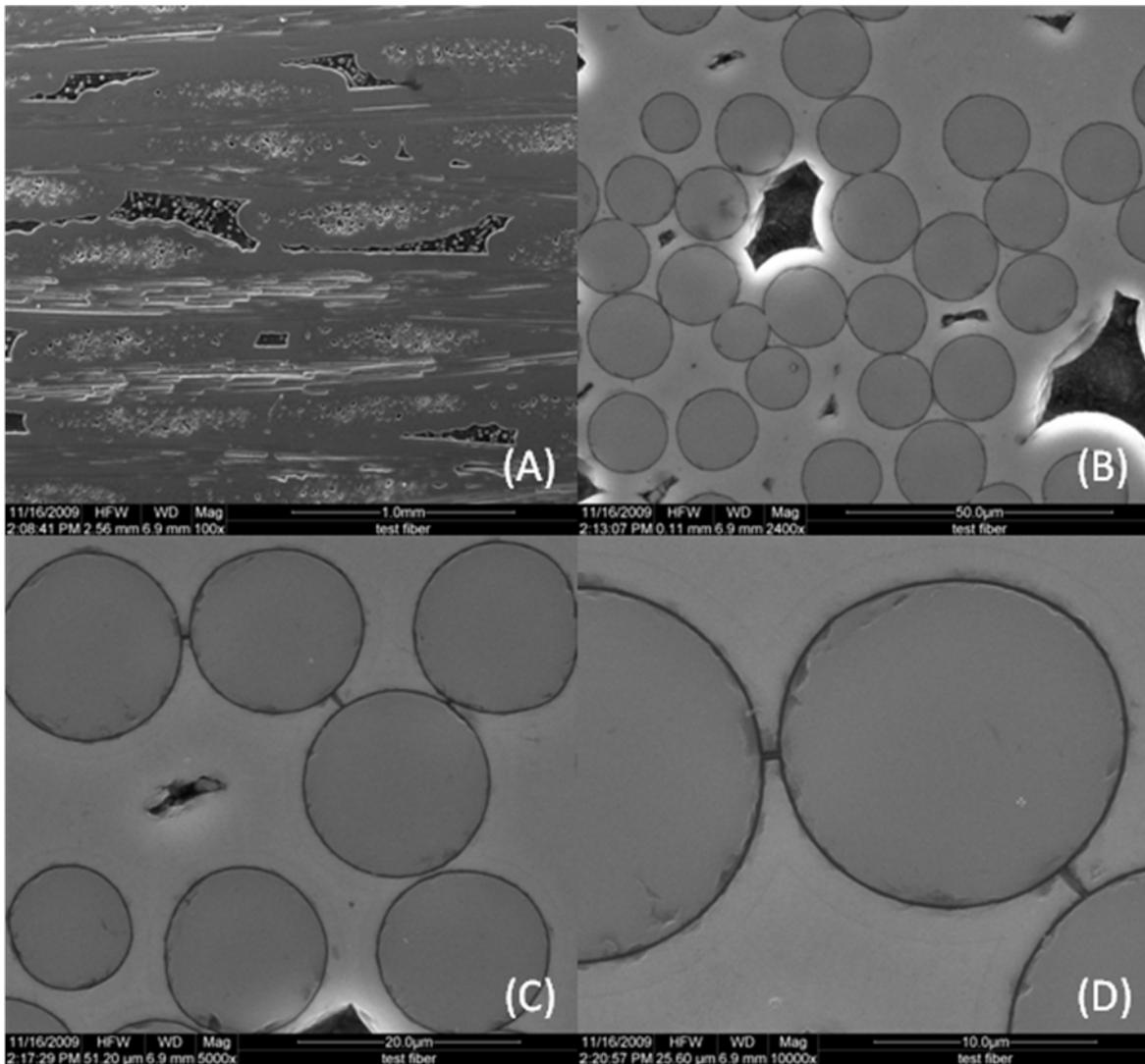
Figure 30: SEM micrographs of the as-processed material from Panel 2 at various magnifications showing similar microstructural features as those observed in Panel 1.
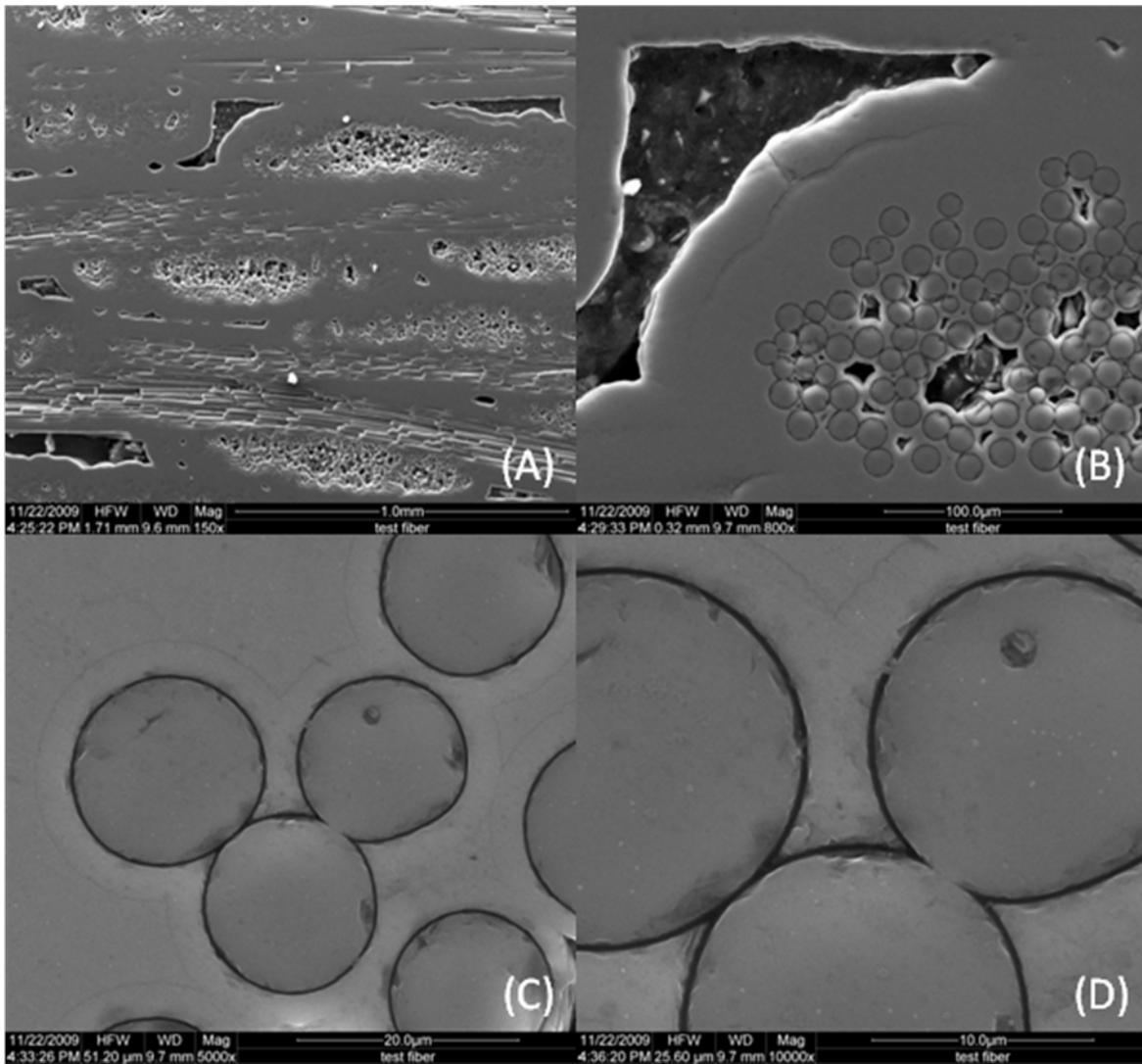
Figure 31: SEM micrographs of virgin material from Panel 3 at various magnifications showing similar microstructural features as those observed in Panel 1.

4.6.2 Microstructure of the Specimens tested in Tension to Failure

To characterize the failure behavior of the Hi-Nicalon/BN/SiC test material, the failed specimens were examined using both a Zeiss optical microscope and a Quanta scanning electron microscope. Figures 32-34 show the optical micrographs of the specimens failed in monotonic tension. It is interesting to note that in these cases little or no fiber pull-out was observed. The fracture surfaces are nearly perpendicular to the 0^0 tows, as seen in Figure 32. The side views of these specimens show no signs of ply delamination.
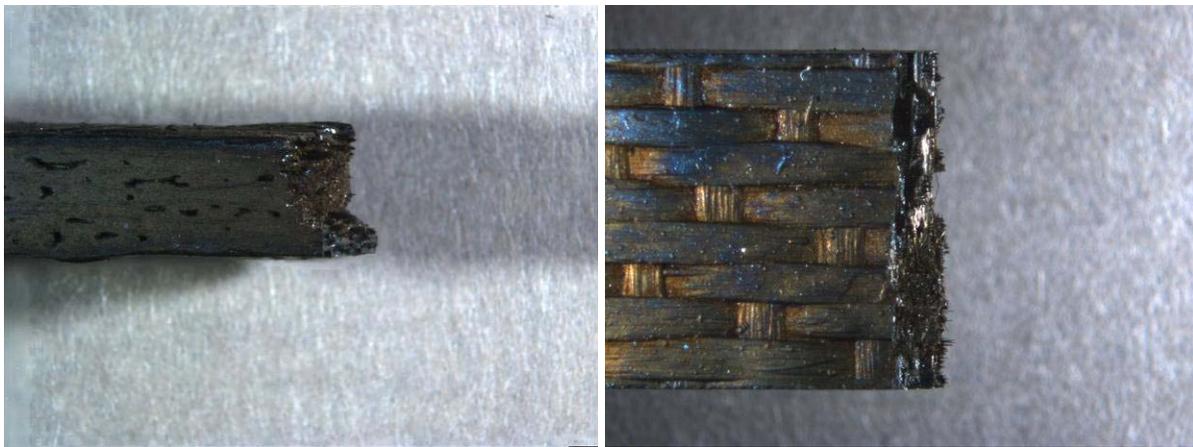
Figure 32: Optical Micrographs of the fracture surfaces produced in tensile test to failure conducted at 0.05mm/sec at 1200 ^{o}C in air on specimen P1-3.
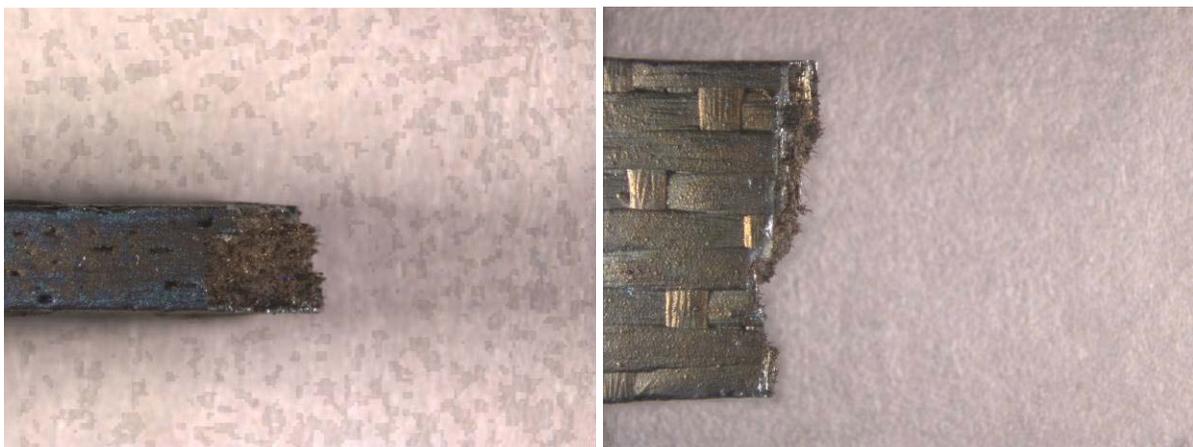
Figure 33: Optical Micrographs of the fracture surfaces produced in tensile test to failure conducted at 0.05mm/sec at 1200 ^{o}C in air on specimen P2-4.
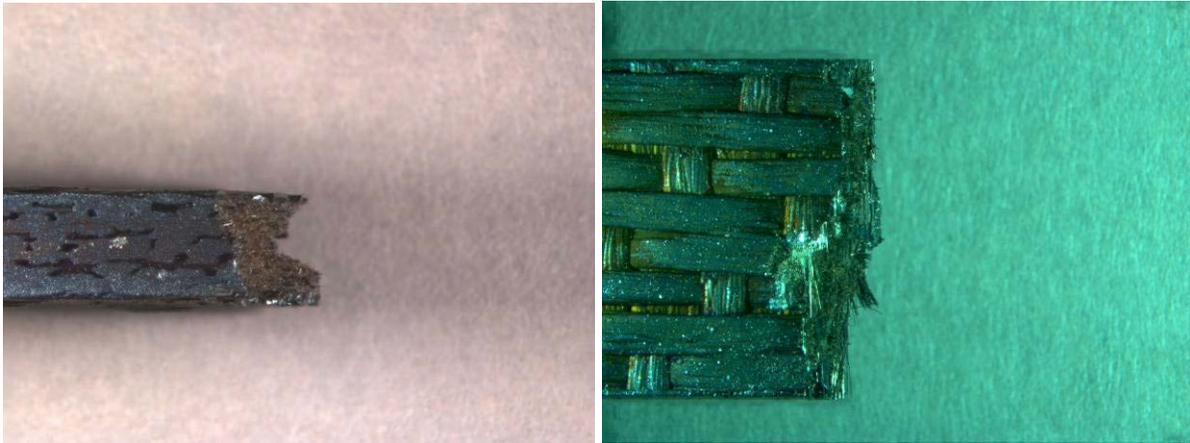
Figure 34: Optical Micrographs of the fracture surfaces produced in tensile test to failure conducted at 0.05mm/sec at 1200 ^{o}C in air on specimen P3-1.

The SEM micrographs of the fracture surface of the three specimens failed in tensile tests also reveal several interesting features. The BN coating appears to be intact indicating that no degradation by oxidation took place. This was expected due to the short duration of the tests. While there is evidence of crack deflection around fibers, as seen in Figure 35 B, cracks also propagated between the "flash" SiC layer and the bulk SiC matrix material, which can be seen in Figures 36 C and D.
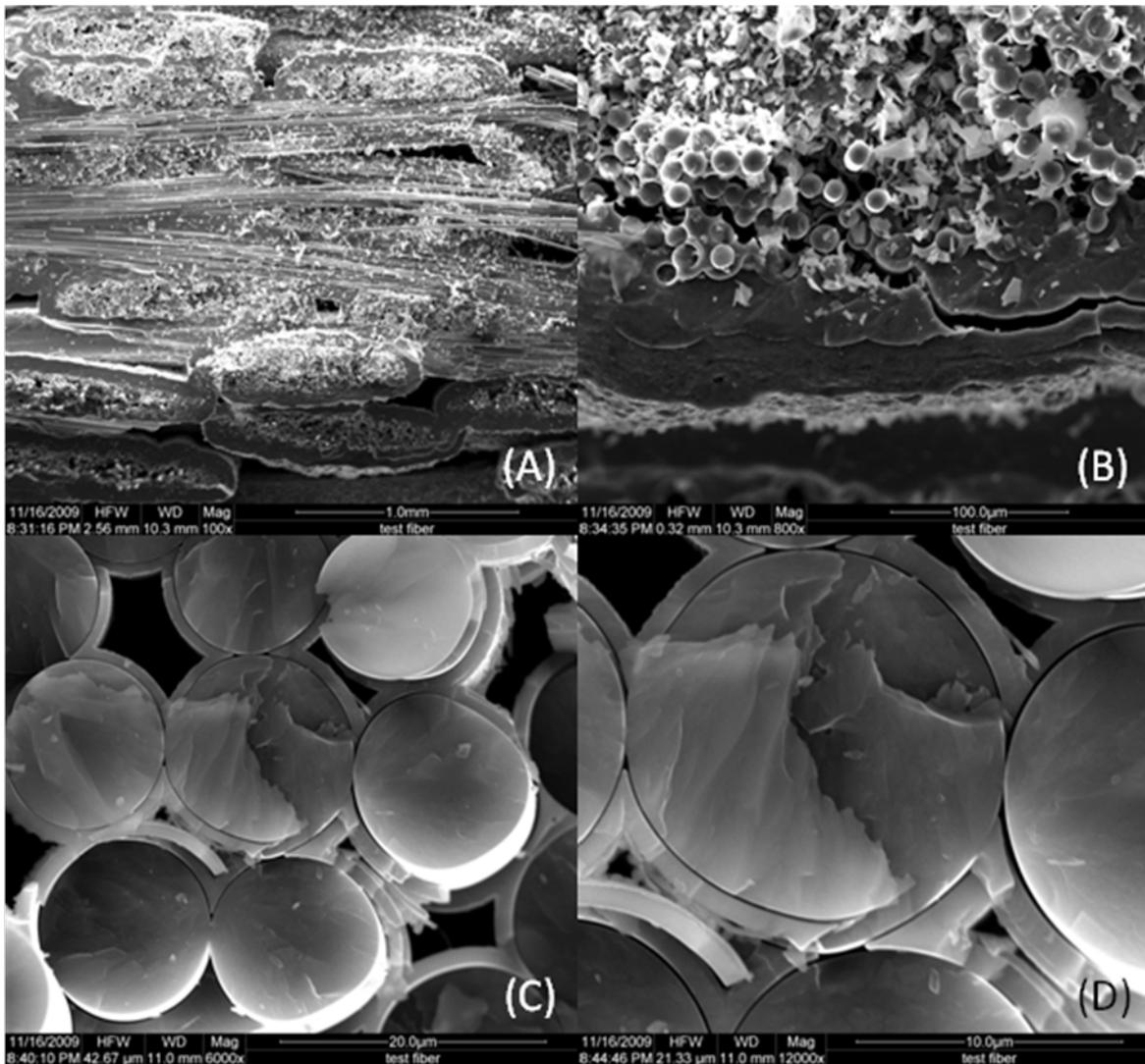
Figure 35: SEM micrographs of fracture surfaces produced in tensile test to failure conducted at 0.05mm/sec at 1200 $^{\circ}$C in air on specimen P1-3.
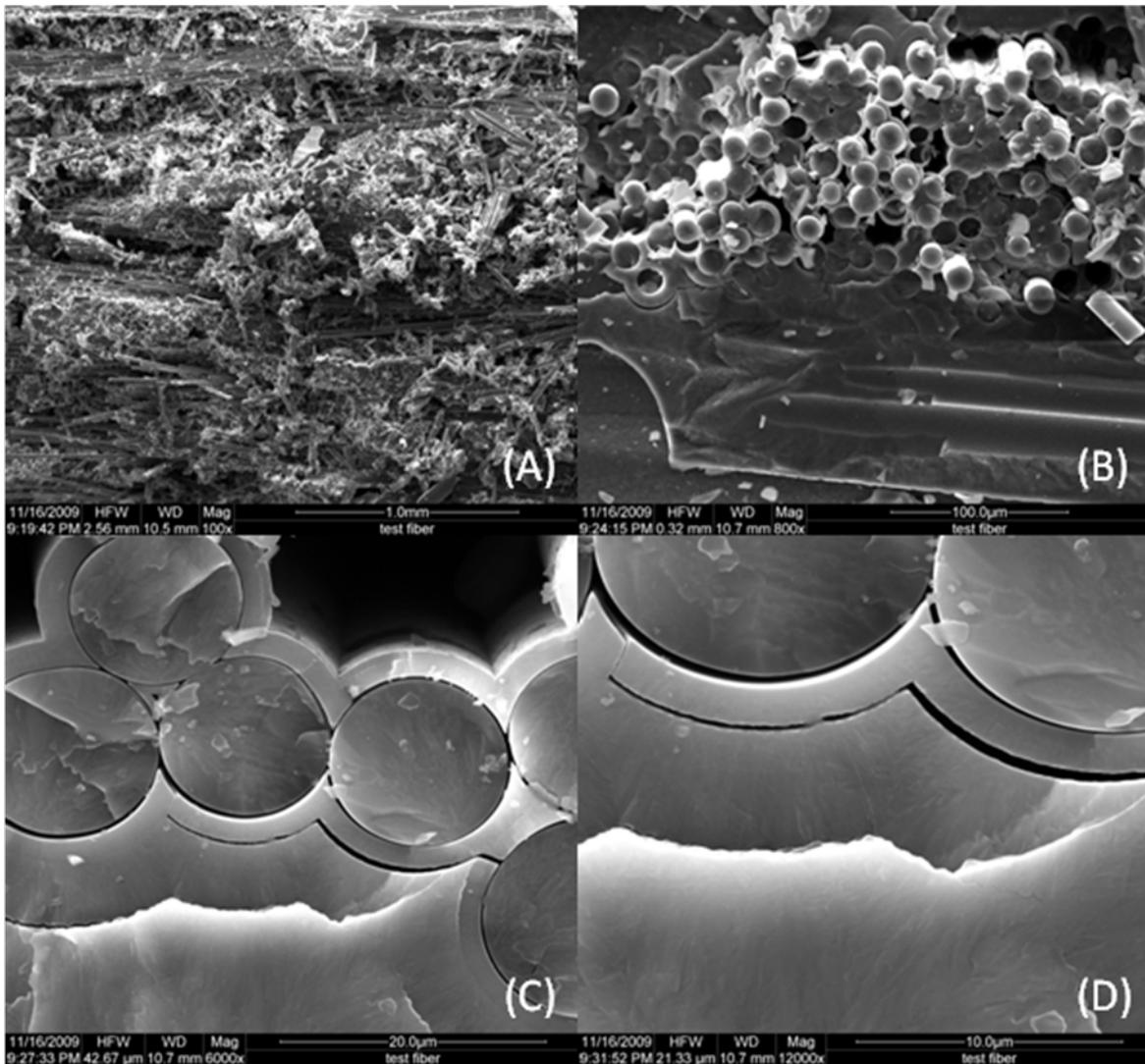
Figure 36: SEM micrographs of fracture surfaces produced in tensile test to failure conducted at 0.05mm/sec at 1200 ^{o}C in air on specimen P2-4.
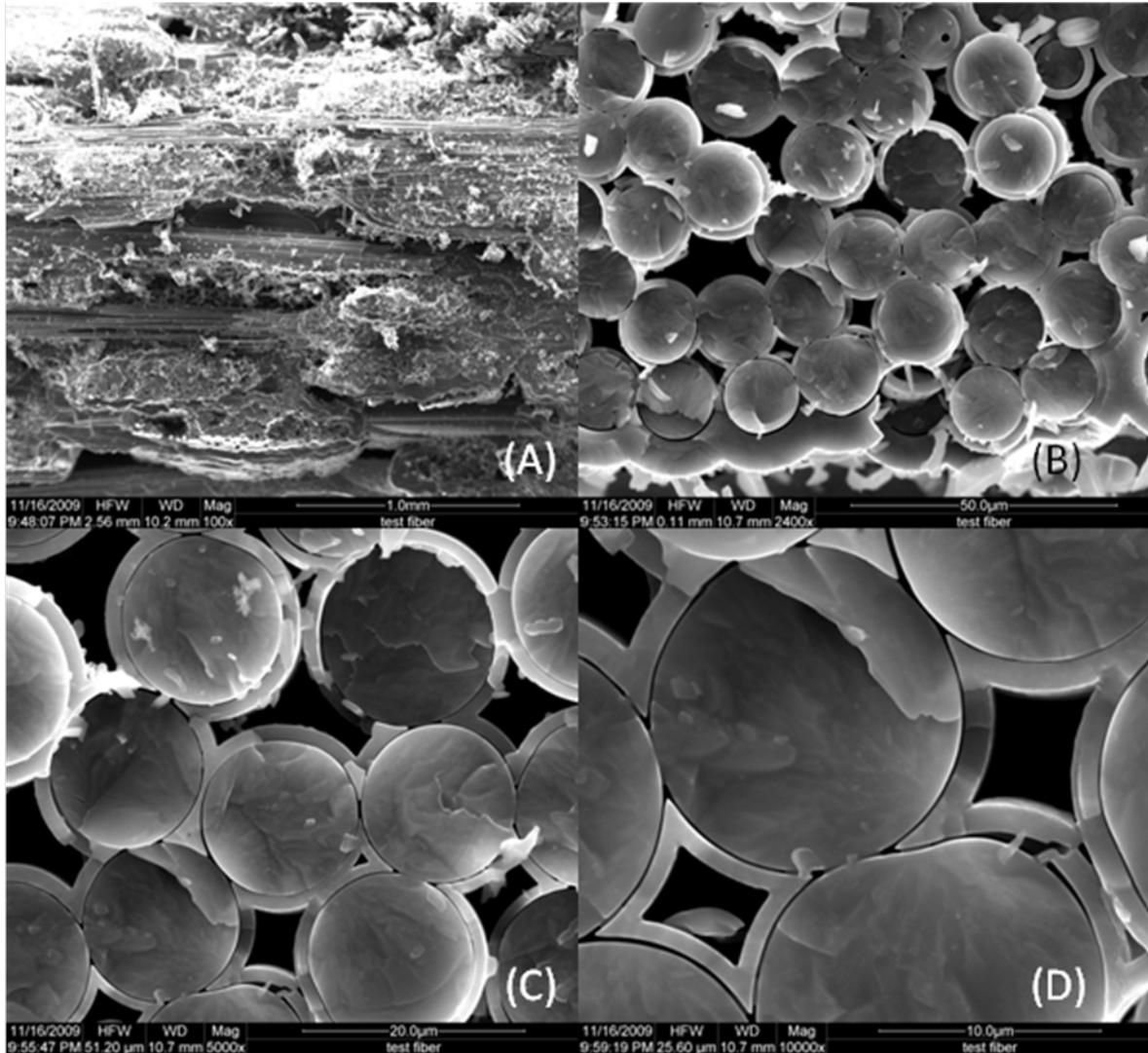
Figure 37: SEM micrographs of fracture surfaces produced in tensile test to failure conducted at 0.05mm/sec at 1200 ^{o}C in air on specimen P3-1.

Analysis of the polished surfaces of these specimens further supports the conclusion that the BN fiber coating was not damaged during the tensile test to failure. Micrographs in Figures 38-40 show the fiber coating remains smooth and uniform in all specimens failed in monotonic tension. There was no apparent damage to the 90^0 fibers. Figures 40 (B) and (C) show what appears to be cracks propagating between fibers; however, closer examination of the micrograph

in Figure 40 (D) suggests this is most likely a BN bridge between fibers, or a gap in the SiC

matrix between adjacent fibers, both of which would have formed during processing.
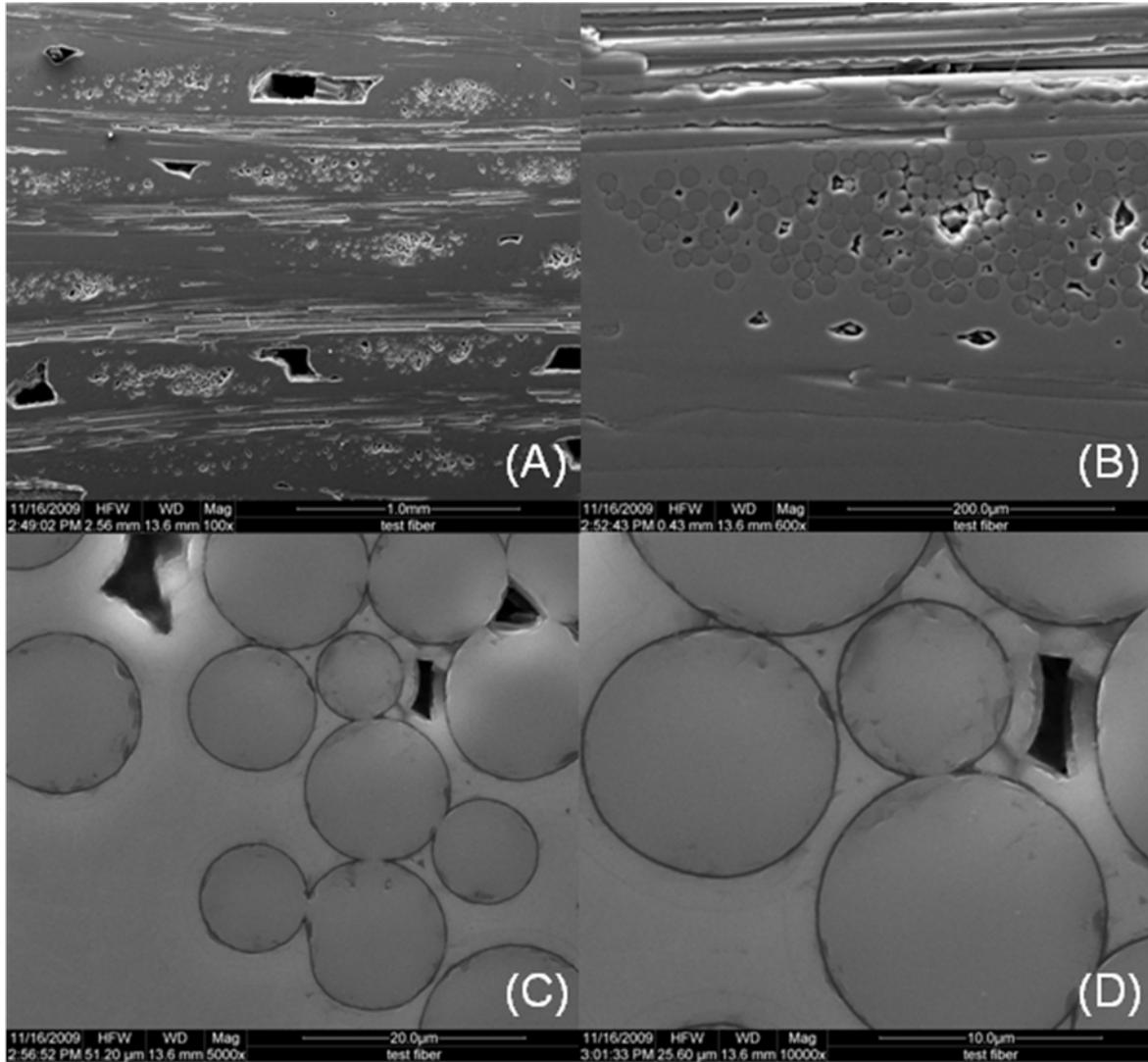
Figure 38: SEM micrographs of polished section from specimen P1-3 failed in tensile test.
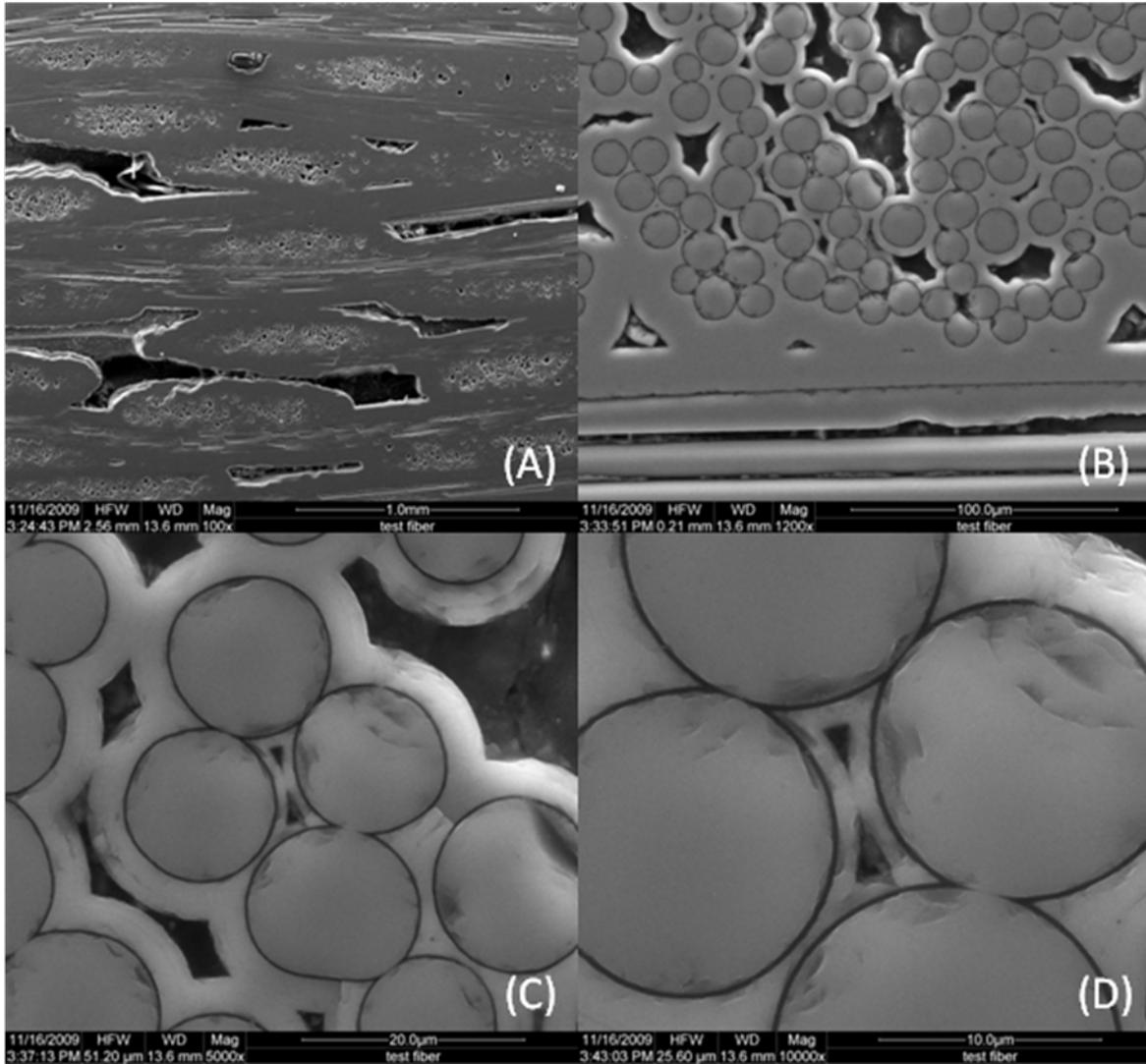
Figure 39: SEM micrographs of polished section from specimen P2-4 failed in tensile test.
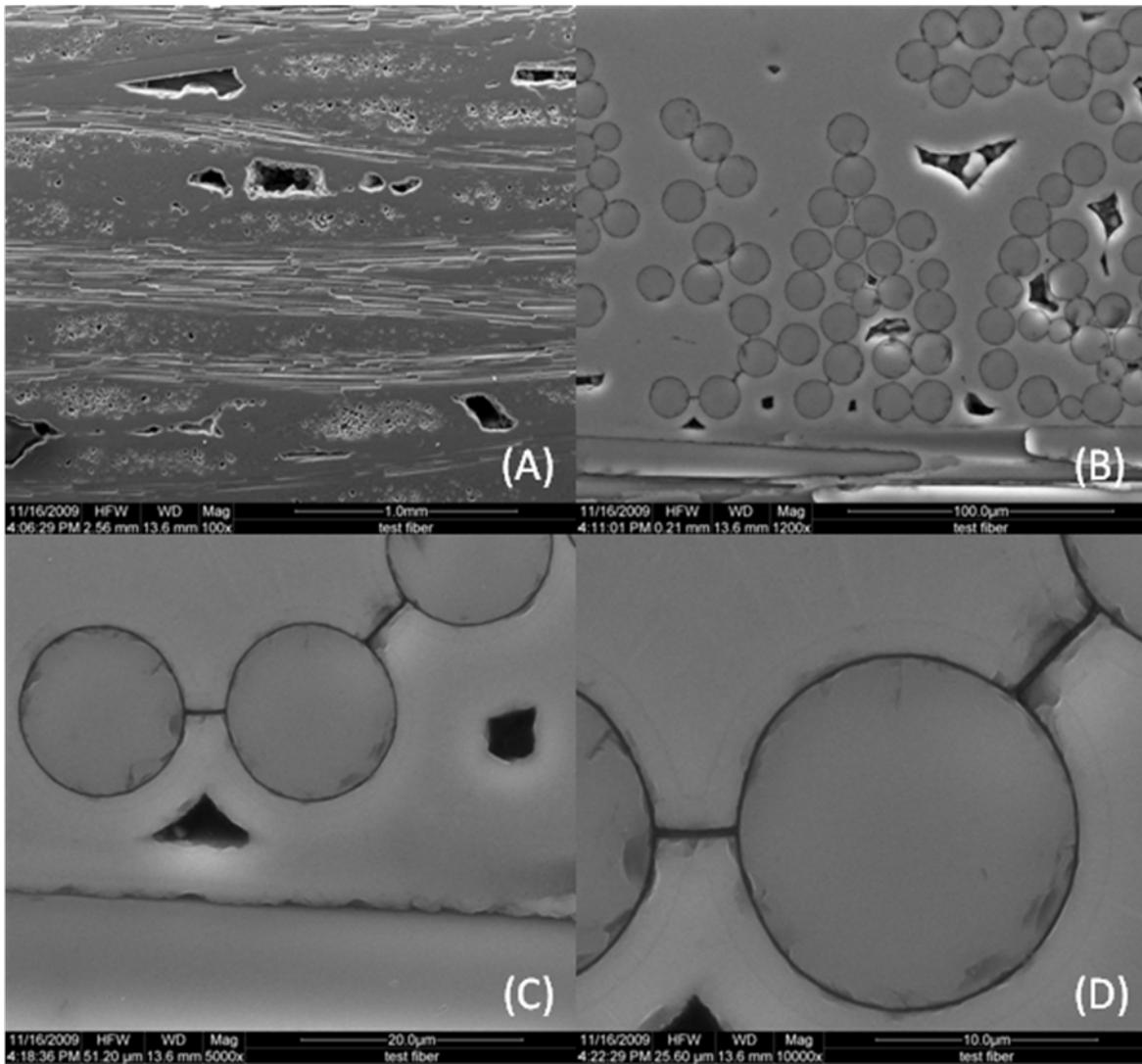
Figure 40: SEM micrographs of polished section from specimen P3-1 failed in tensile test.

4.6.3 Microstructure of the Specimens tested in Fatigue at 0.1 Hz

Figures 41-44 show the optical micrographs of specimens P2-6 and P2-7 which were subjected to fatigue at 0.1 Hz in air and specimens P3-9 and P3-7 which were subjected to fatigue at 0.1 Hz in steam. It is interesting to note that fiber pull-out occurred in specimen P2-6, which was tested with the high fatigue stress in air and produced short time to failure. Fiber pull out is also observed for specimen P3-7 which was tested with the low fatigue stress and achieved fatigue run-out in steam.
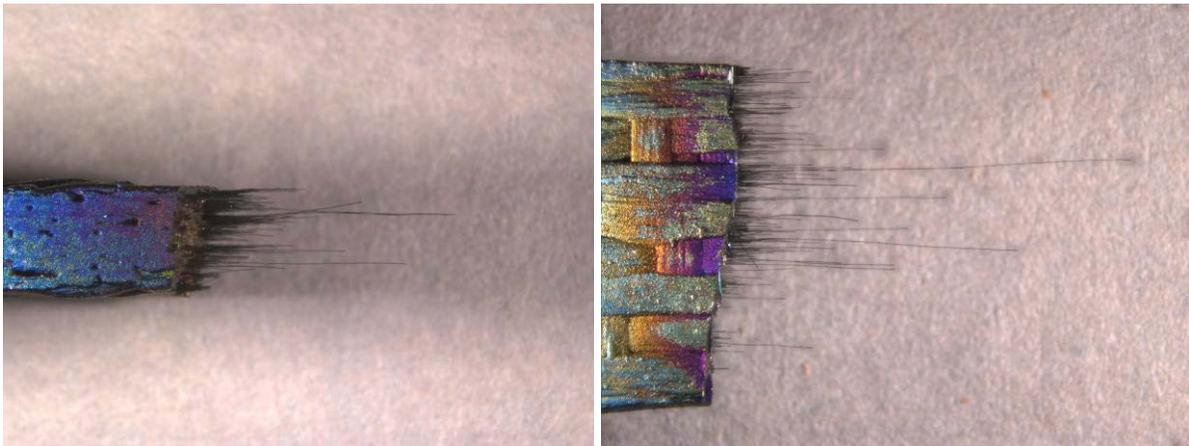
Figure 41: Optical micrographs of specimen P2-6 tested in fatigue at 0.1 Hz in air at 1200 ^{o}C. σmax = 120 MPa, Nf = 3780, tf = 10.5 h.
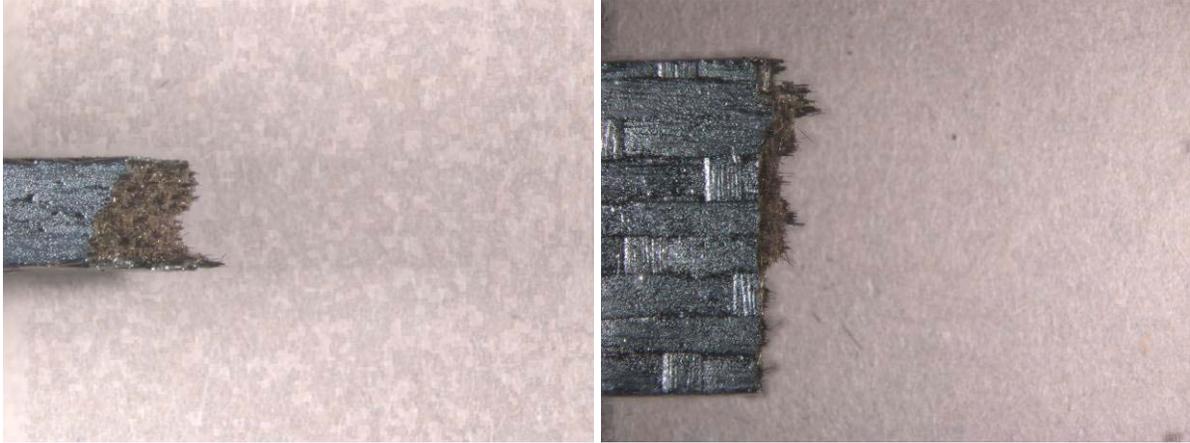
Figure 42: Optical micrographs of specimen P2-7 tested in fatigue at 0.1 Hz in air at 1200 ^{o}C. σmax = 100 MPa, Nf = 100,000, tf = 277.78 h.
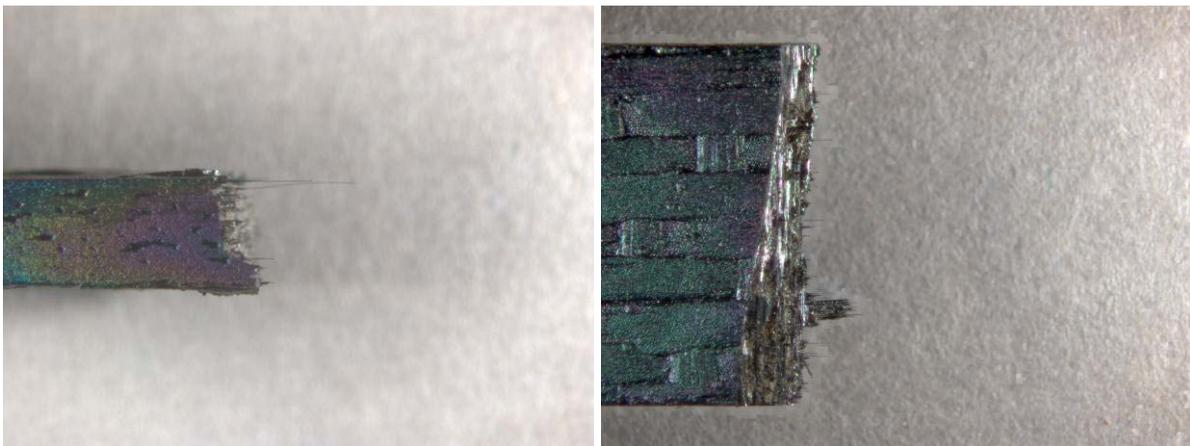
Figure 43: Optical micrographs of specimen P3-9 tested in fatigue at 0.1 Hz in steam at 1200 ^{o}C. σmax = 110 MPa, Nf = 548, tf = 1.52 h.
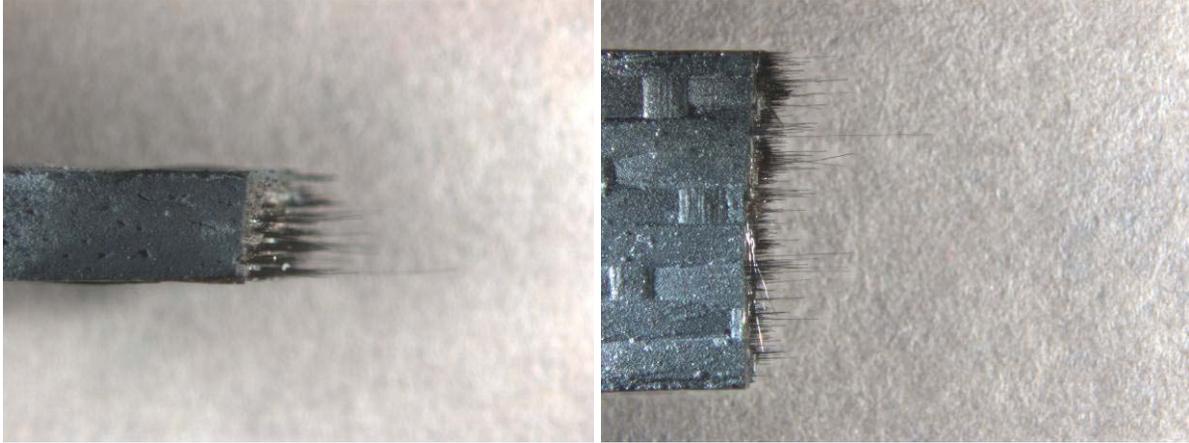
Figure 44: Optical micrographs of specimen P3-7 tested in fatigue at 0.1 Hz in steam at 1200 ^{o}C. σmax = 88 MPa, Nf = 88,575, tf = 246.04 h.

The SEM micrographs of the specimens P2-6 and P2-7 tested in fatigue at 0.1 Hz in air are shown in Figures 45 and 46. The SEM micrographs of the specimens P3-9 and P3-7 tested in fatigue at 0.1 Hz in steam are shown in figures 47 and 48. Figures 45 (B) and (C) show damage occurring in the 90^{0} fibers. Figure 46 B shows a matrix crack originating at the sharp corner of a void. Such voids produce stress concentrations. Several notable features are seen on the fracture surfaces of the specimens tested in steam. Figure 47 (C) shows oxidation of the fracture surface. The fracture edges are rounded and the fracture surfaces of the fibers are smoothed. Small, nearly round glassy deposits, a common result of oxidation, are also observed. However, while some regions of the fracture surface show evidence of oxidation, other regions of the fracture surface, such as that in Figure 47 (B) and 47 (D), show sharp fracture surfaces of the fibers and the presence of BN fiber coatings. The regions showing no evidence of oxidative degeneration were the last to fail.
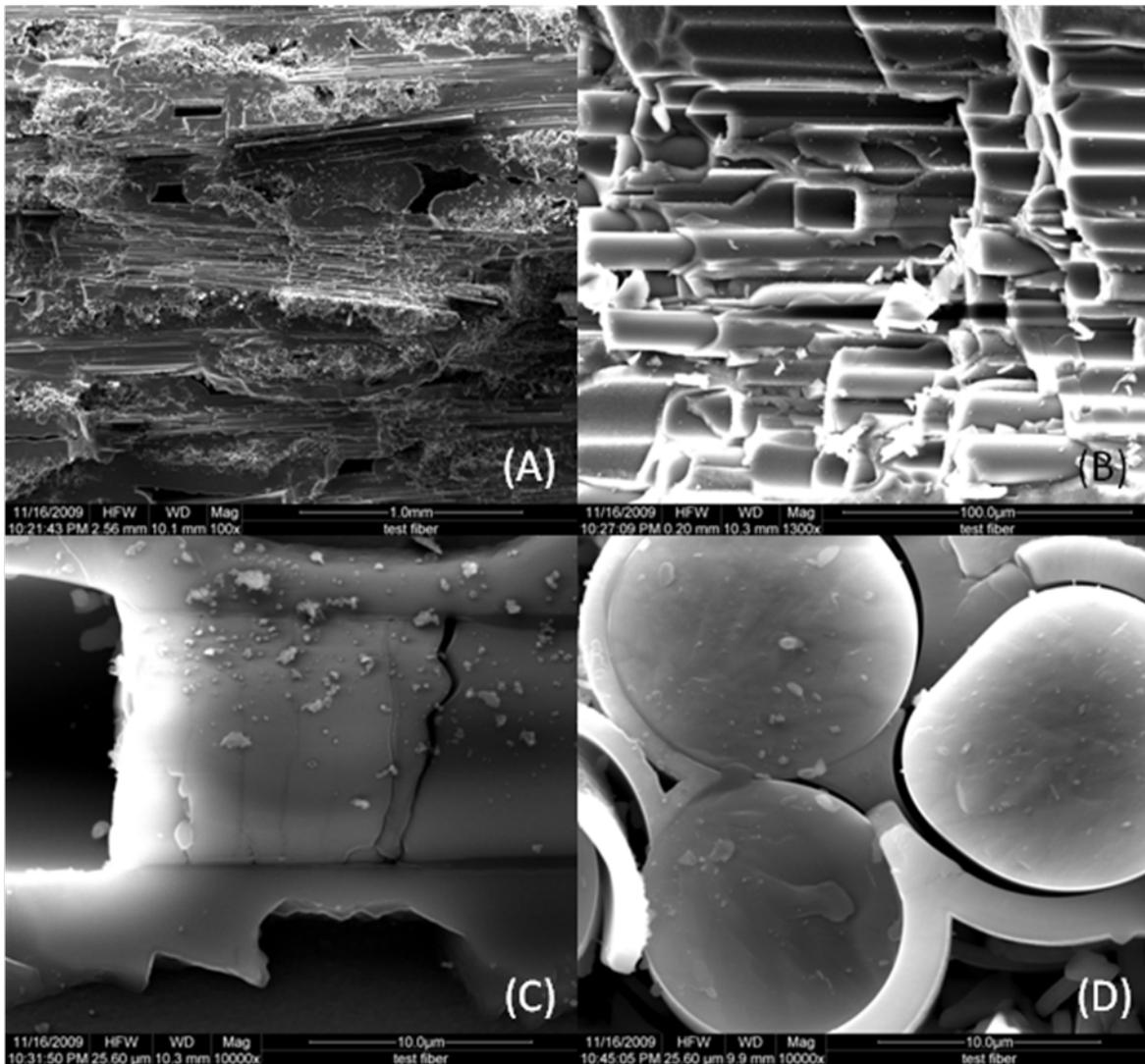
Figure 45: SEM micrographs of fracture surface of specimen P2-6 tested in fatigue at 0.1 Hz in air at 1200 ^{o}C. σmax = 120 MPa, Nf = 3780, tf = 10.5 h.
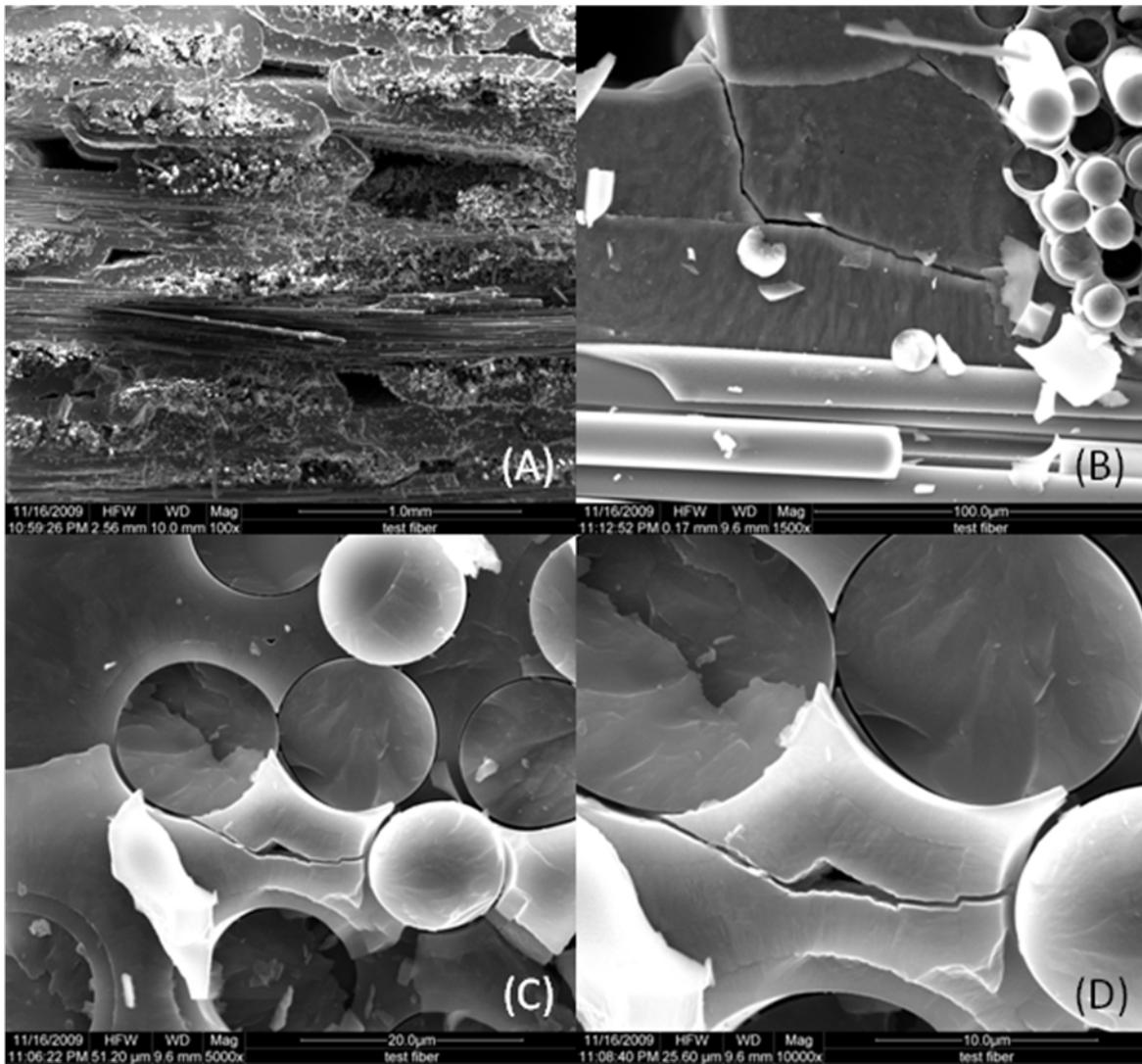
Figure 46: SEM micrographs of fracture surface of specimen P2-7 tested in fatigue at 0.1 Hz in air at 1200 ^{o}C. σmax = 100 MPa, Nf = 100,000, tf = 277.78 h.
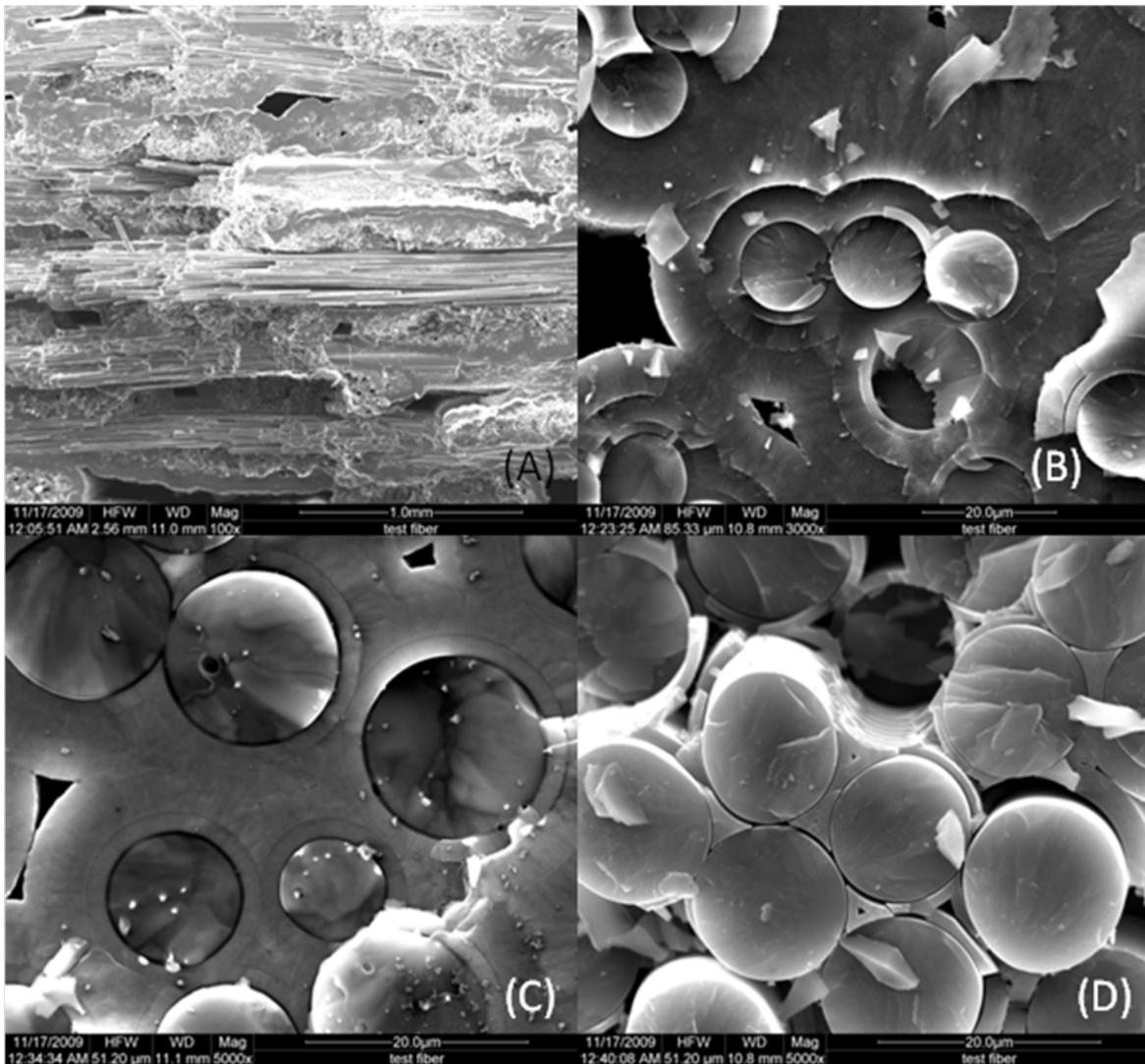
Figure 47: SEM micrographs of fracture surface of specimen P3-9 tested in fatigue at 0.1 Hz in steam at 1200 ^{o}C. σmax = 110 MPa, Nf = 548, tf = 1.52 h.
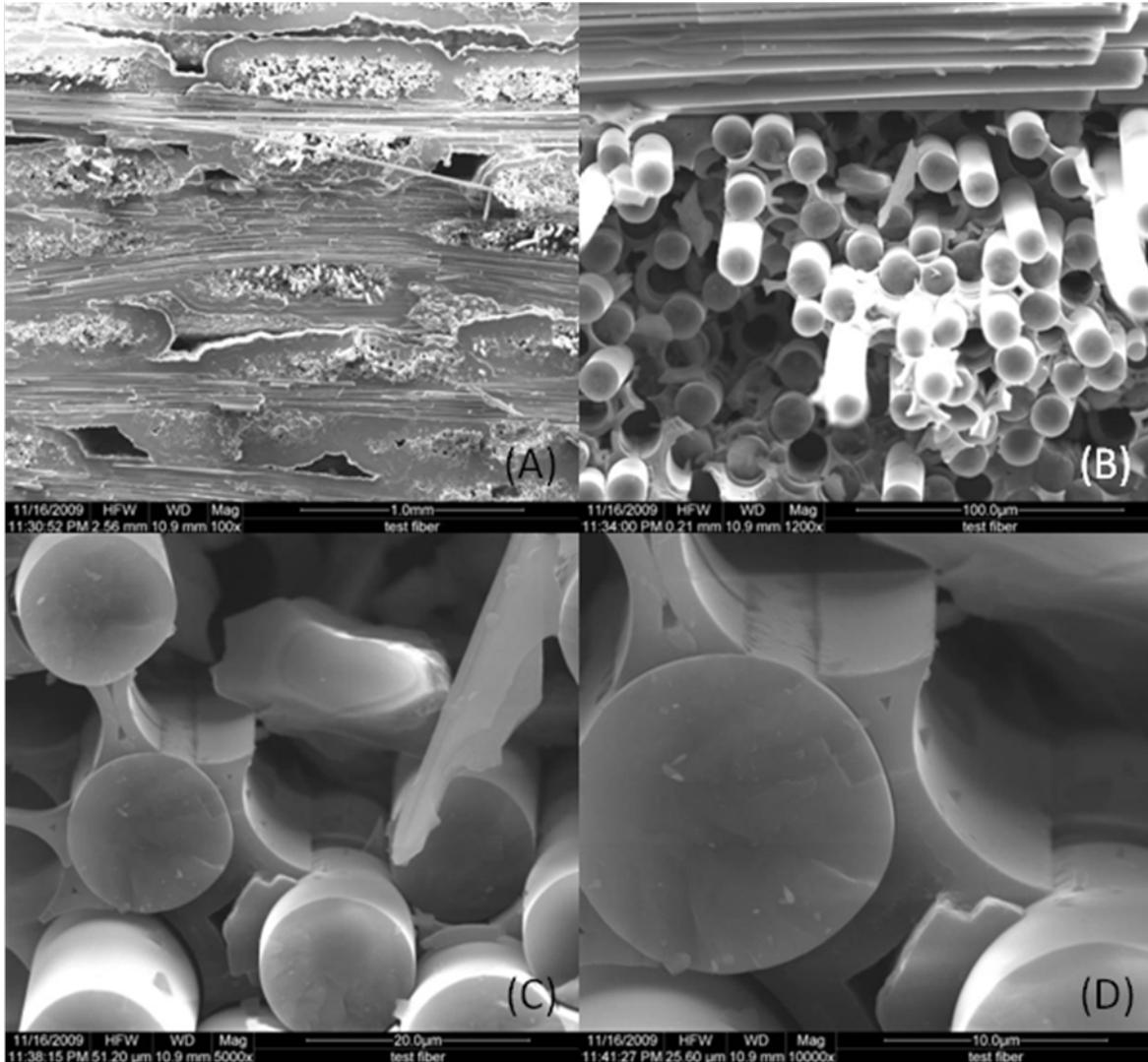
Figure 48: SEM micrographs of fracture surface of specimen P3-7 tested in fatigue at 0.1 Hz in steam at 1200 ^{o}C. σmax = 88 MPa, Nf = 88,575, tf = 246.04 h.

The polished sections from specimens P2-6 and P2-7 subjected to fatigue at 0.1 Hz in air are shown in Figures 49 and 50. Figure 49 shows no apparent matrix damage. Conversely, Figure 50 (A) shows matrix cracks originating at voids. Figure 50 (B) shows a matrix crack damaging a 0^0 fiber. However, other areas of specimen P2-7 do not show matrix damage or fiber damaged as seen in Figures 50 (C) and 50 (D).
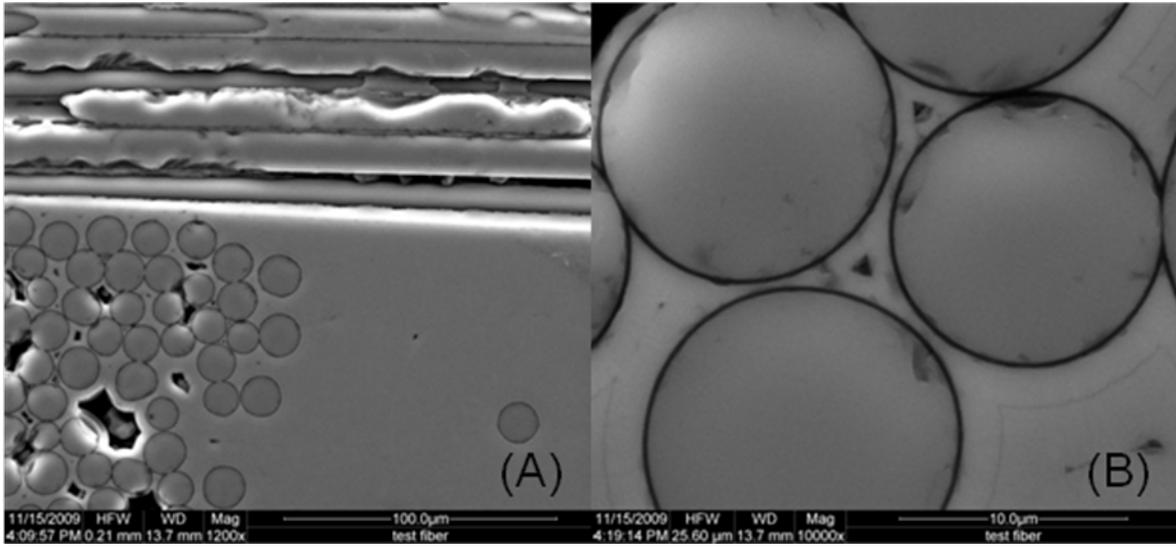
Figure 49: SEM micrographs of polished surface of specimen P2-6 tested in fatigue at 0.1 Hz in air at 1200 ^{o}C. σmax = 120 MPa, Nf = 3780, tf = 10.5 h.
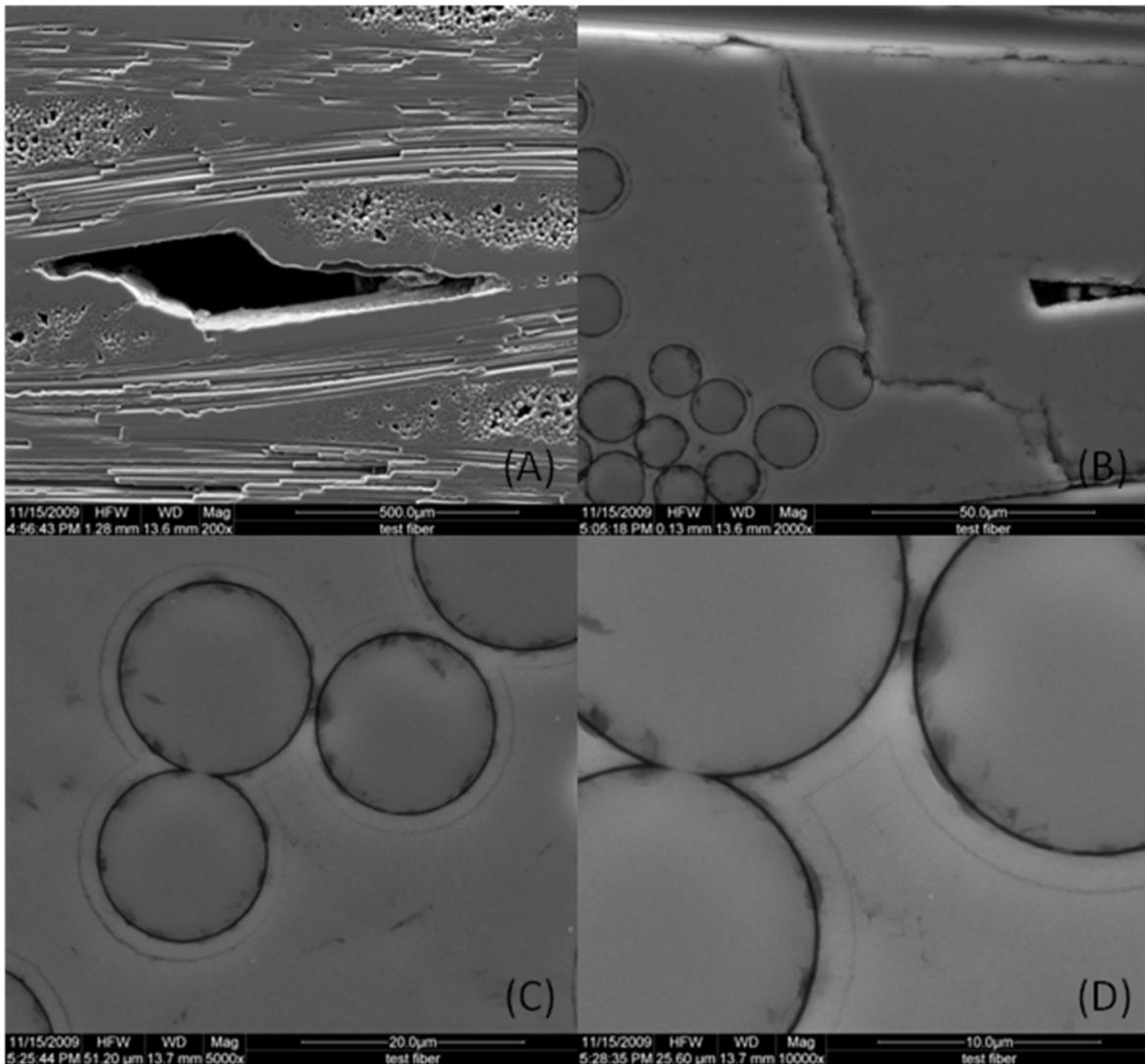
Figure 50: SEM micrographs of polished surface of specimen P2-7 tested in fatigue at 0.1 Hz in air at 1200 °C. σmax = 100 MPa, Nf = 100,000, tf = 277.78 h.

The SEM micrographs of the polished section of specimens P3-9 and P3-7 subjected to fatigue at 0.1 Hz in steam are shown in Figures 51 and 52. Micrographs of both specimens show significant matrix cracking with cracks propagating between 0^0 fibers as seen in Figure 51 (A), or along the "flash" SiC layer/SiC matrix interface as seen in Figure 52 (B).
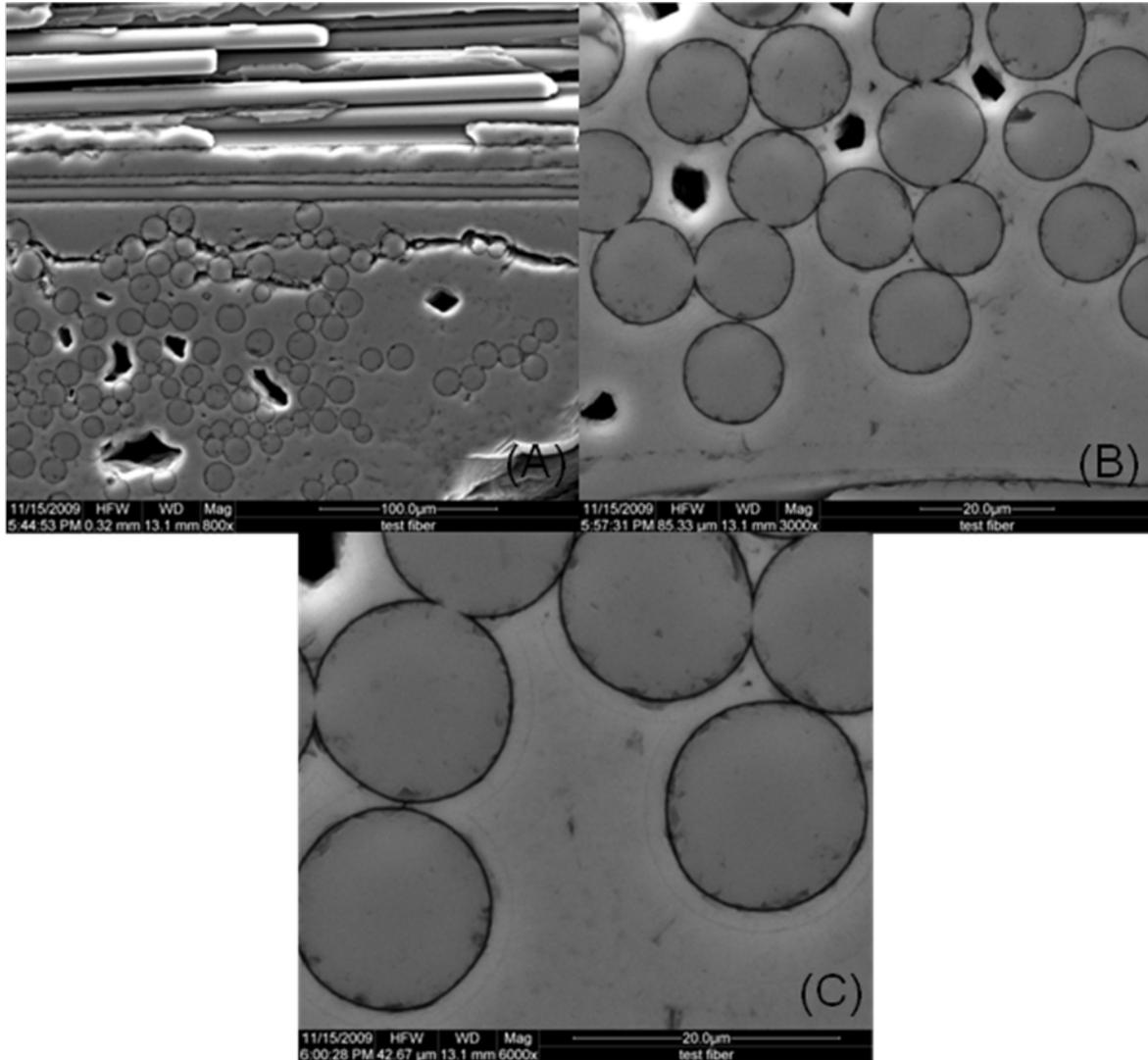
Figure 51: SEM micrographs of polished surface of specimen P3-9 tested in fatigue at 0.1 Hz in steam at 1200 ^{o}C. σmax = 110 MPa, Nf = 548, tf = 1.52 h.
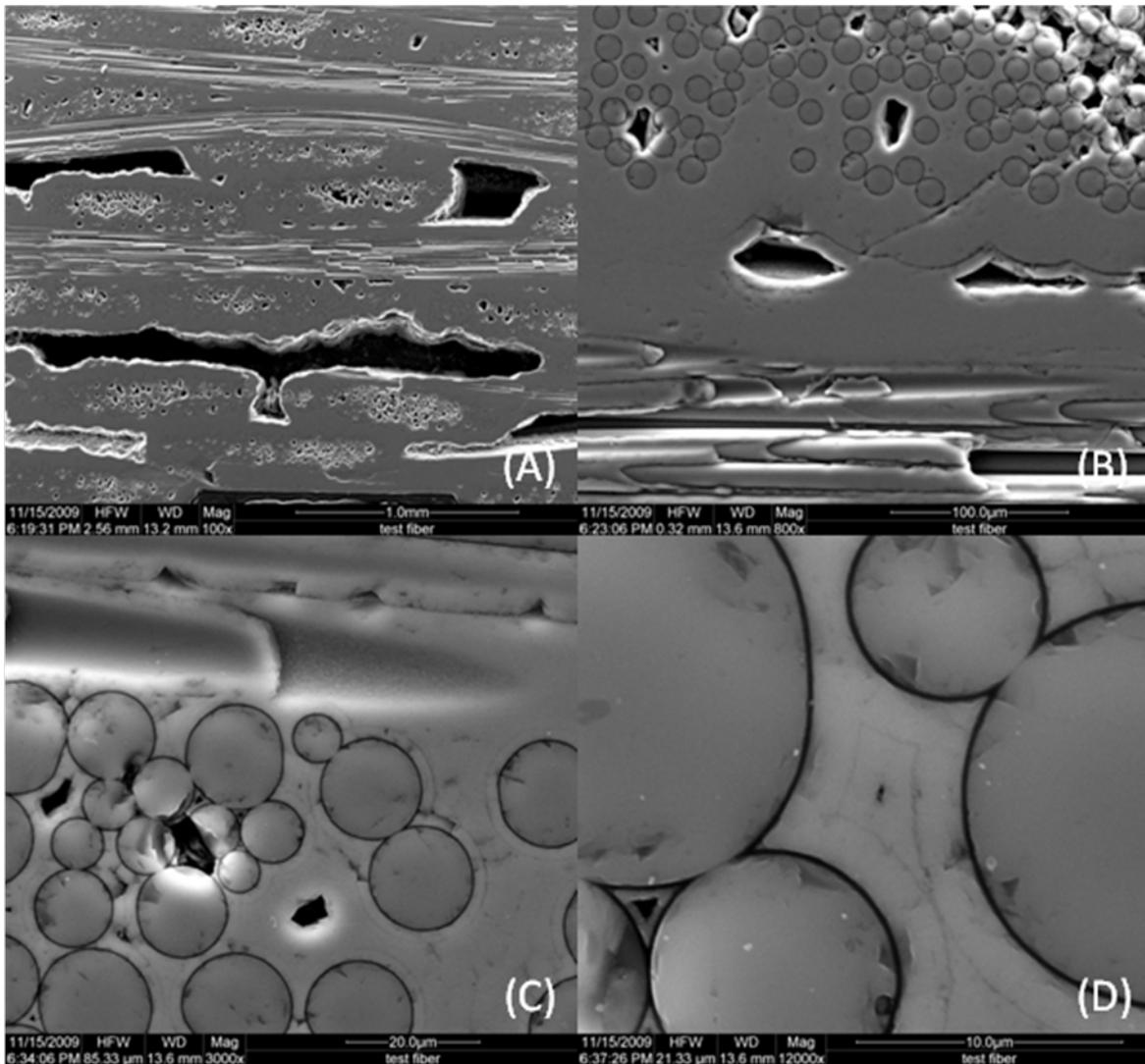
Figure 52: SEM micrographs of polished surface of specimen P3-7 tested in fatigue at 0.1 Hz in steam at 1200 ^{o}C. σmax = 88 MPa, Nf = 88,575, tf = 246.04 h.

4.6.4 Microstructure of the Specimens tested in Fatigue at 1.0 Hz

Figures 53-56 show the optical micrographs of the fracture surfaces produced in fatigue tests conducted at 1.0 Hz in air and in steam. Micrographs Figures 53-56 show no delamination between plies irrespective of the fatigue stress level or test environment. With the exception of specimen P1-4 tested in air with a fatigue stress of 120 MPa, none of the specimens tested at 1.0 Hz exhibited significant fiber pull-out.
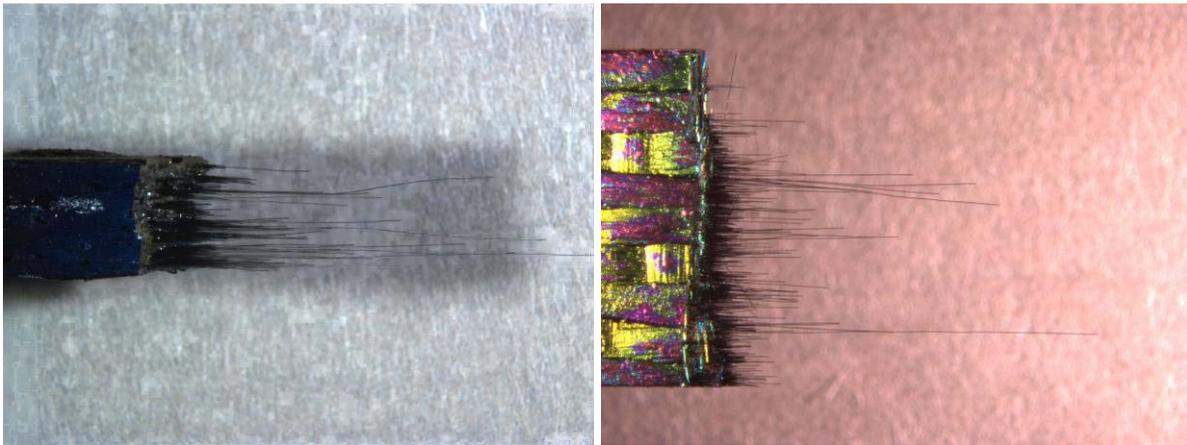
Figure 53: Optical micrographs of specimen P1-4 tested in fatigue at 1.0 Hz in air at 1200 $^{\circ}$C. σmax = 120 MPa, Nf = 3766, tf = 1.05 h.
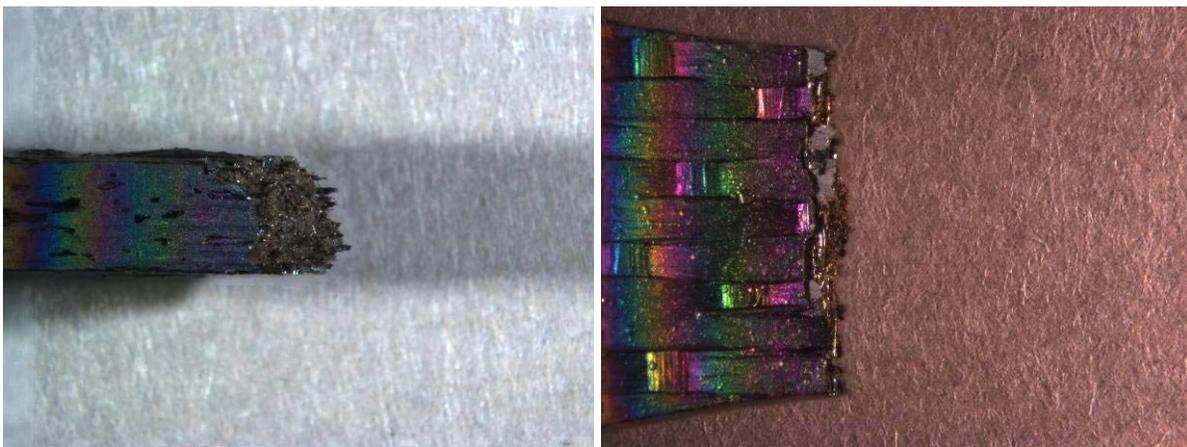
Figure 54: Optical micrographs of specimen P1-5 tested in fatigue at 1.0 Hz in air at 1200 $^{\circ}$C. σmax = 80 MPa, Nf = 200,000, tf = 55.56 h.
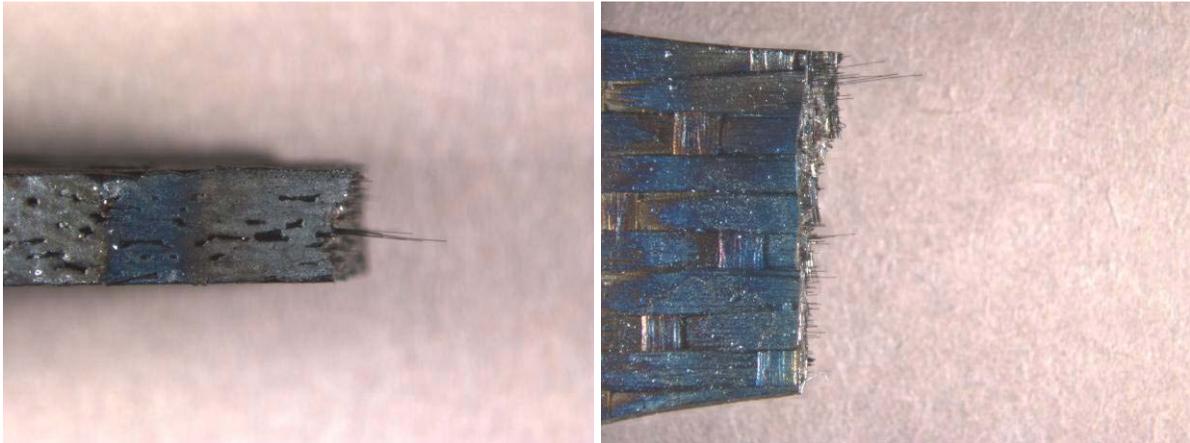
Figure 55: Optical micrographs of specimen P1-9 tested in fatigue at 1.0 Hz in steam at 1200 °C. σmax = 110 MPa, Nf = 5620, tf = 1.56 h.
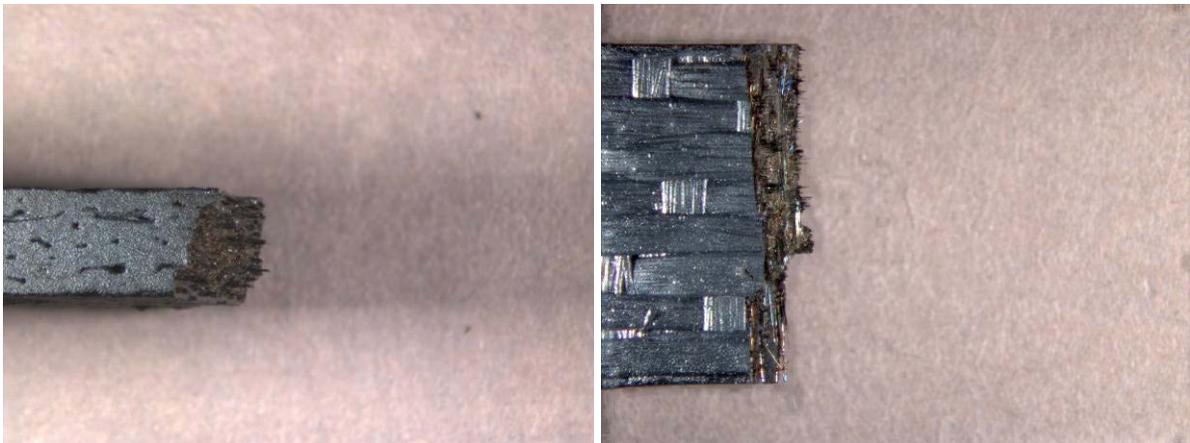
Figure 56: Optical micrographs of specimen P3-2 tested in fatigue at 1.0 Hz in steam at 1200 °C. σmax = 80 MPa, Nf = 200,000, tf = 55.56 h.

Figures 57 and 58 show the SEM micrographs of the fracture surfaces of specimen P1-4 and figure 59 shows specimen P1-5 tested in fatigue at 1.0 Hz in air. Areas near the edge of the fracture surface of specimen P1-4 tested in air show the glassy, smoothed over topography caused by oxidation. Although the fracture surface of the specimen P1-4, which failed after 1.05 h, showed evidence of oxidation, the fracture surface of specimen P1-5, which achieved fatigue

run-out, revealed no signs of oxidative degradation. As was the case with the fracture surfaces obtained in fatigue tests in air, the fracture surfaces produced in steam showed evidence of oxidation near the edges. The oxidative damage was much less evident in the center where matrix cracks had not propagated.

Another unusual failure mode is seen in Figure 58. This view of the fracture surface of specimen P1-4 shows what appears to be "islands" of matrix material pulled out along with the 0^0 fibers. A possible explanation is that matrix microcracks perpendicular to those fibers coalesced allowing these plates of matrix material to form and cleave off intact.

Figures 60 and 61 show the SEM micrographs of the fracture surfaces of specimens P1-9 and P3-2, respectively. These specimens were tested in fatigue at 1.0 Hz in steam. Both specimens had fracture surfaces with rugged, brittle-fracture areas, and smooth areas which exhibited oxidative damage. In figure 60, the oxidative damage appears more severe than on the fracture surfaces after the 1.0 Hz tests conducted in air. Otherwise, similar fracture behavior was observed in both environments.
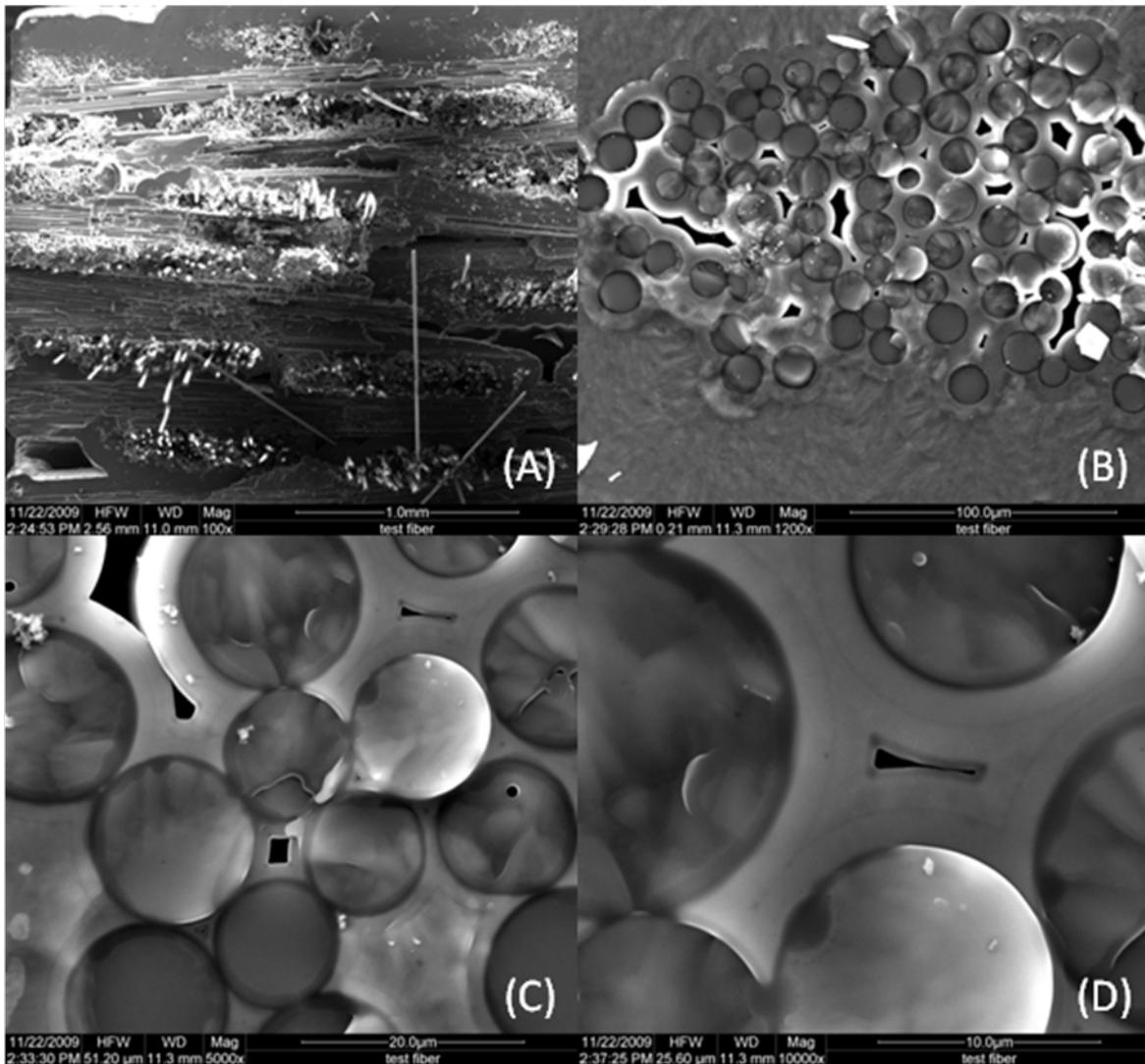
Figure 57: SEM micrographs of the fracture surface of specimen P1-4 tested in fatigue at 1.0 Hz in air at 1200 °C. σmax = 120 MPa, Nf = 3766, tf = 1.05 h.
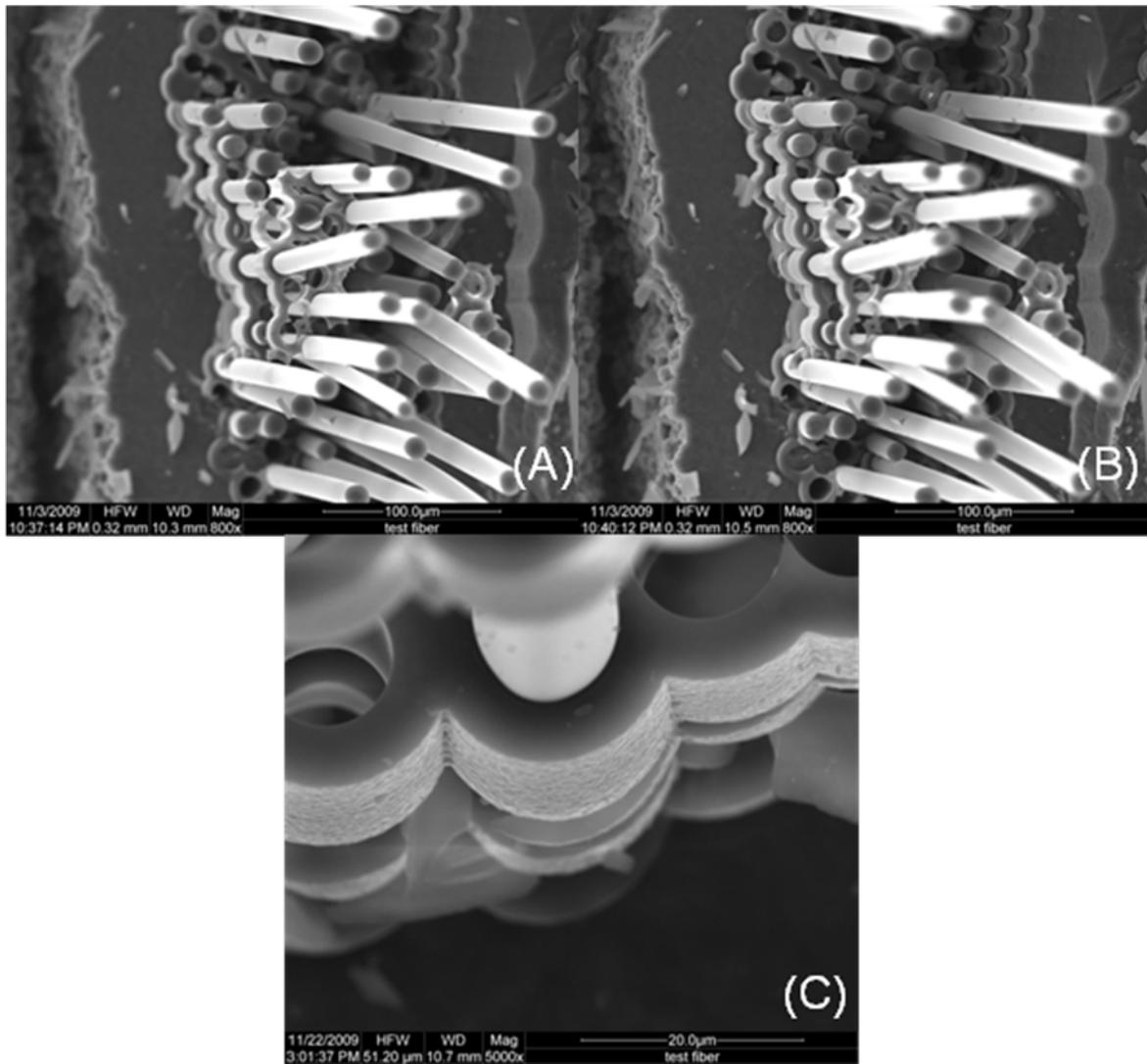
Figure 58: SEM micrographs of the fracture surface of specimen P1-4 showing "islands" of matrix material pulled out along with the 0^0 fibers.
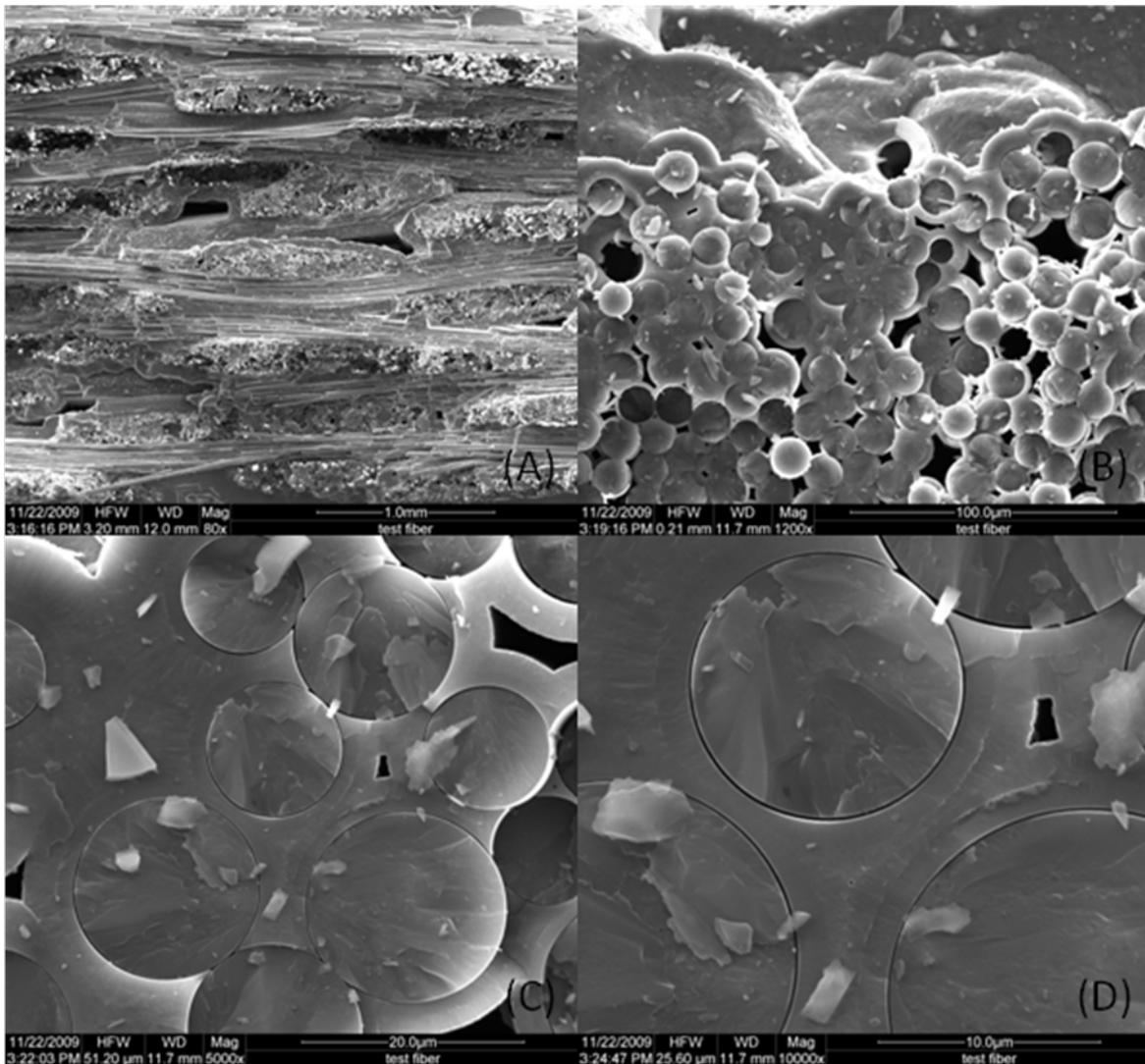
Figure 59: SEM micrographs of the fracture surface of specimen P1-5 tested in fatigue at 1.0 Hz in air at 1200 ^{o}C. σmax = 80 MPa, Nf = 200,000, tf = 55.56 h.
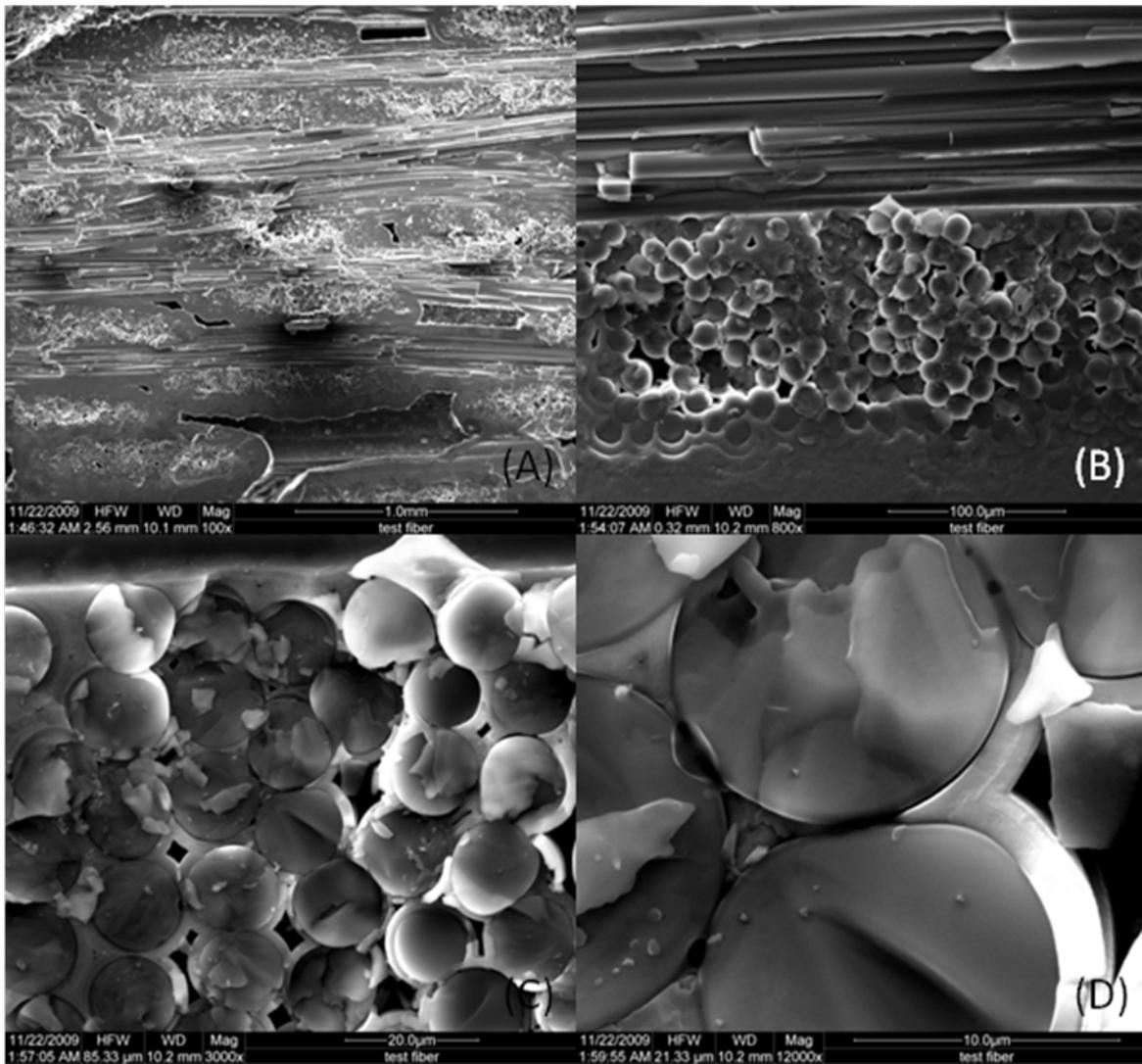
Figure 60: SEM micrographs of the fracture surface of specimen P1-9 tested in fatigue at 1.0 Hz in steam at 1200 ^{o}C. σmax = 110 MPa, Nf = 5620, tf = 1.56 h.
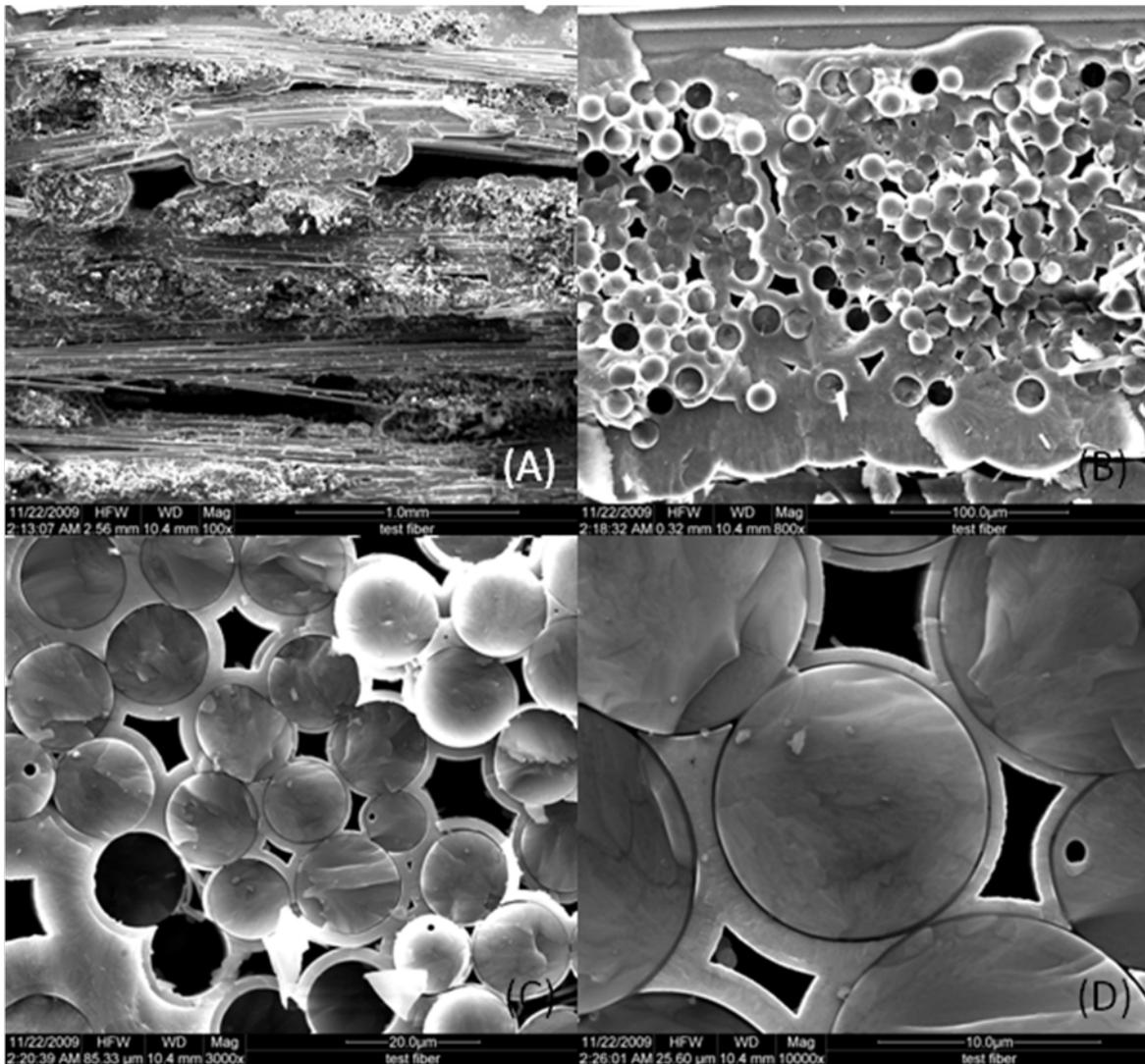
Figure 61: SEM micrographs of the fracture surface of specimen P3-2 tested in fatigue at 1.0 Hz in steam at 1200 $^{\circ}$C. σmax = 80 MPa, Nf = 200,000, tf = 55.56 h.

SEM micrographs of the polished sections of specimens tested in fatigue at 1.0 Hz are shown in Figures 62-65. In Figure 62 (B) a matrix crack is seen growing and causing the failure of a 90^0 fiber. Matrix cracks are seen forming at the sharp corners of voids, then propagating along the "flash" SiC layer/SiC matrix interface (see Figure 63 B). Figure 63 D, however, shows cracks growing through the matrix and stopping at the "flash" SiC layer.
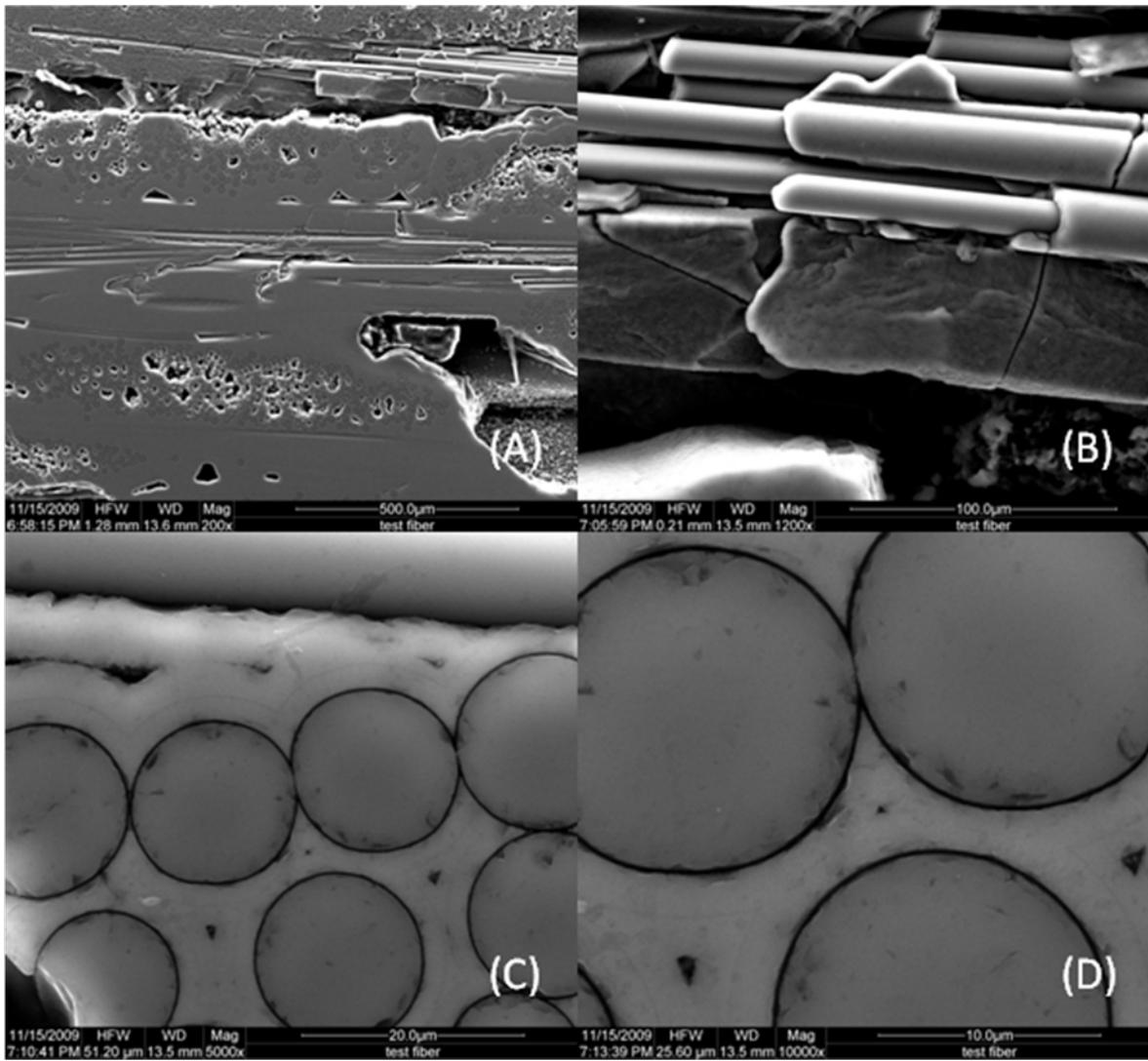
Figure 62: SEM micrographs of the polished surface of specimen P1-4 tested in fatigue at 1.0 Hz in air at 1200 ^{o}C. σmax = 120 MPa, Nf = 3766, tf = 1.05 h.
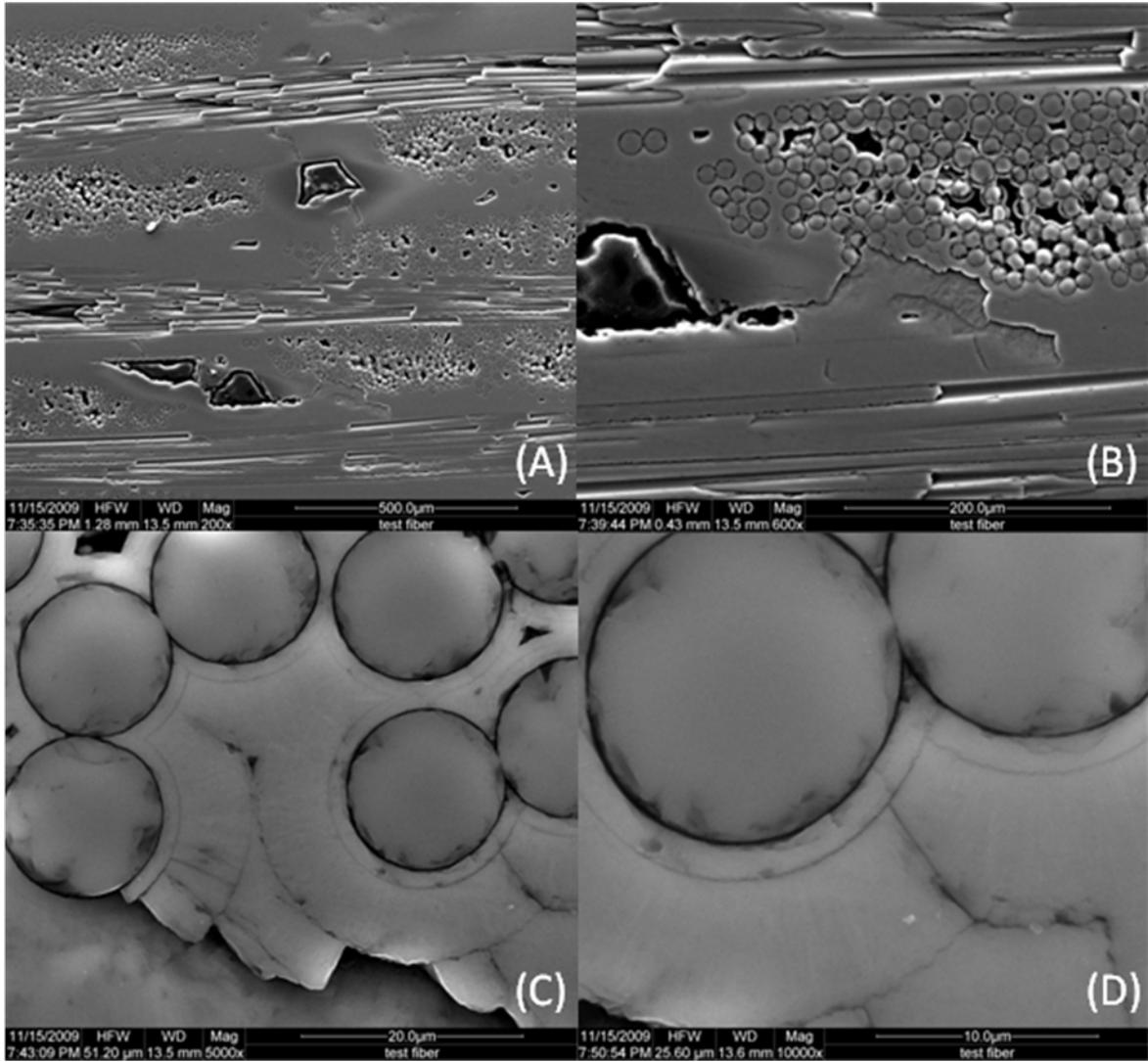
Figure 63: SEM micrographs of the polished surface of specimen P1-5 tested in fatigue at 1.0 Hz in air at 1200 $^\circ$C. σmax = 80 MPa, Nf = 200,000, tf = 55.56 h.
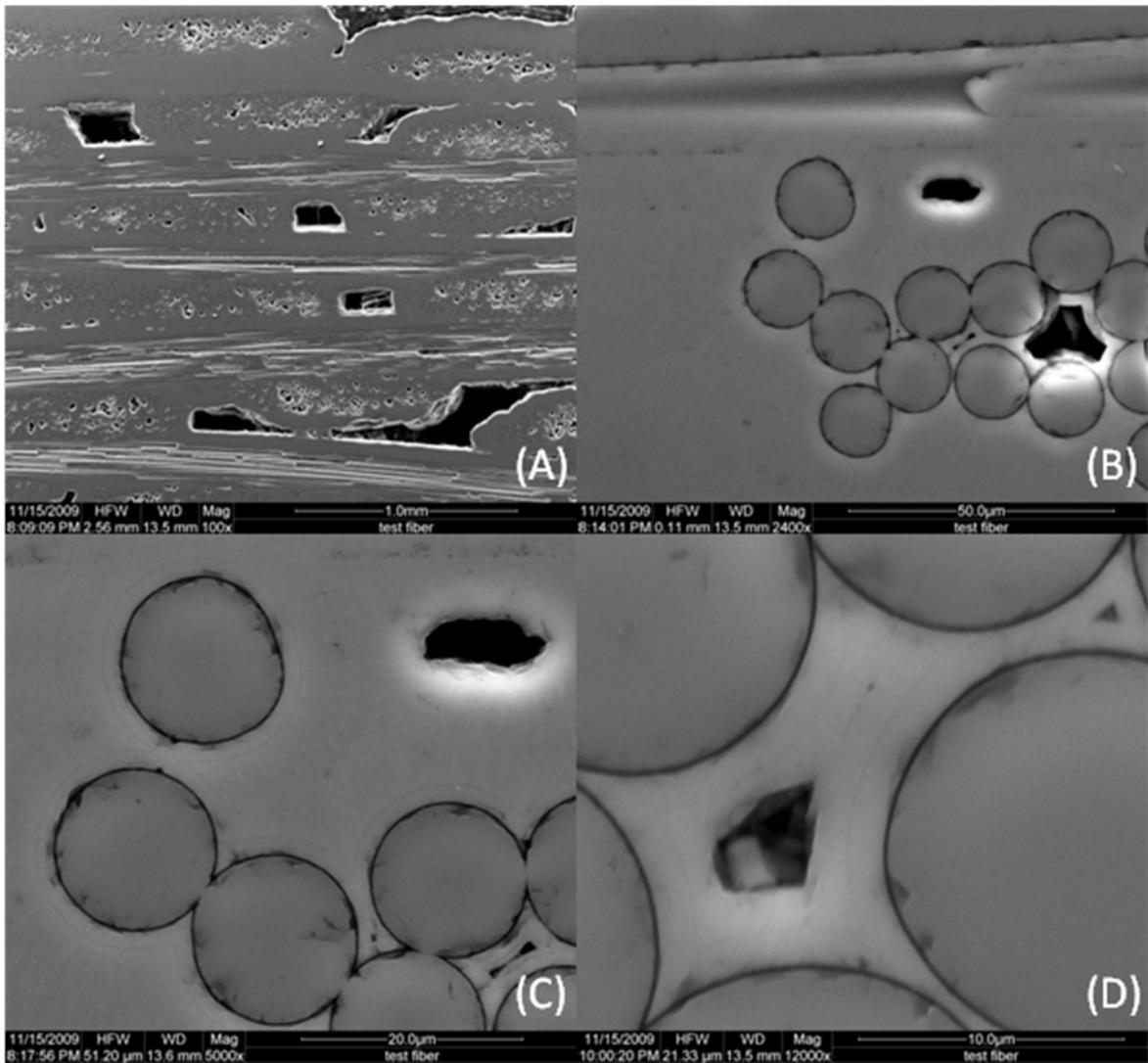
Figure 64: SEM micrographs of the polished surface of specimen P1-9 tested in fatigue at 1.0 Hz in steam at 1200 ^{o}C. σmax = 110 MPa, Nf = 5620, tf = 1.56 h.
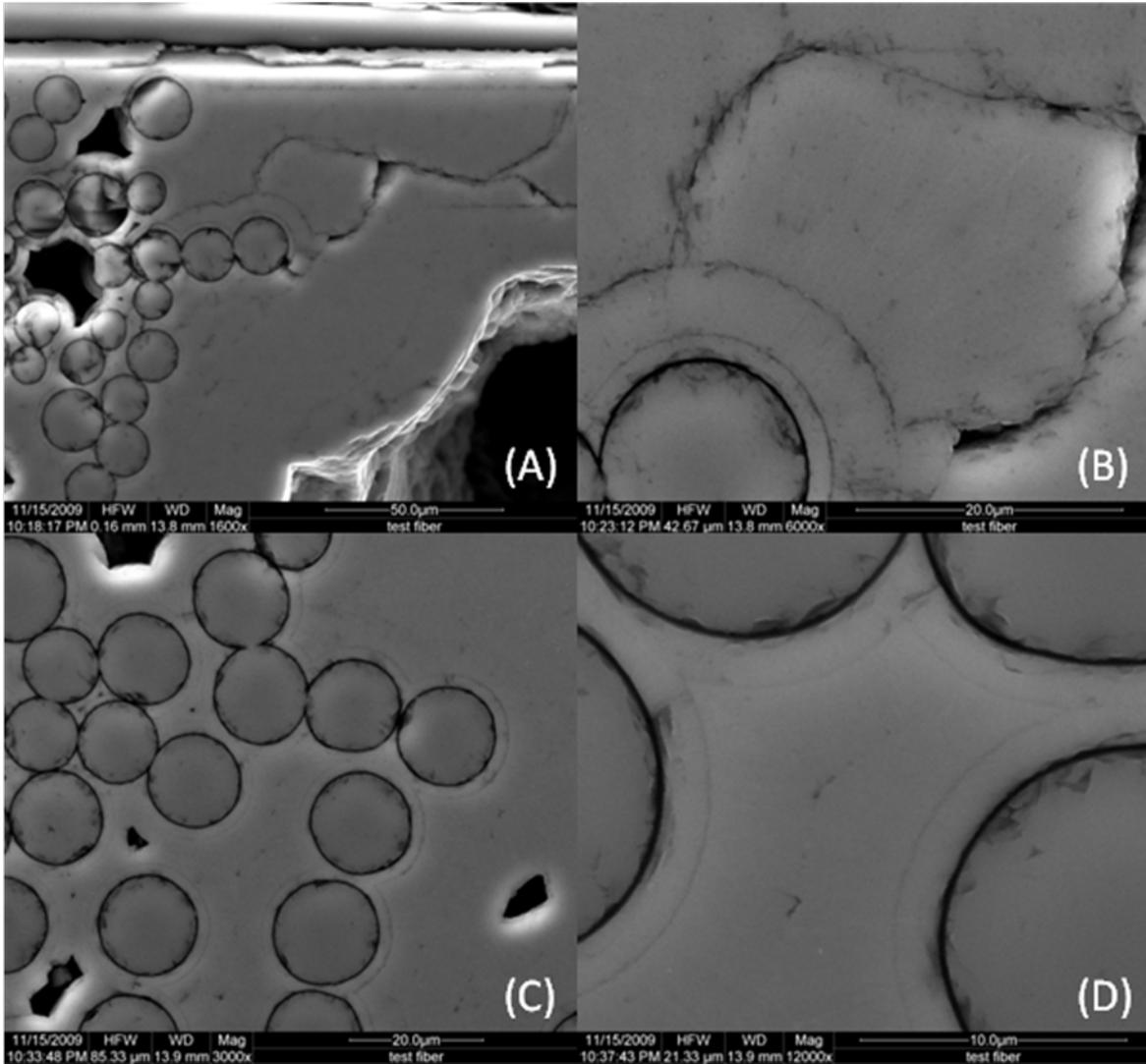
Figure 65: SEM micrographs of the polished surface of specimen P3-2 tested in fatigue at 1.0 Hz in air at 1200 ^{o}C. σmax = 80 MPa, Nf = 200,000, tf = 55.56 h.

4.6.5 Microstructure of the Specimens tested in Fatigue at 10 Hz

Figures 66-69 show the optical micrographs of the fracture surfaces of specimens P3-3 and P2-5 which were tested in fatigue at 10 Hz in air and the optical micrographs of the fracture surfaces of specimens P3-4 and P3-6 which were tested in fatigue at 10 Hz in steam. None of the specimens tested at 10 Hz produced fiber pull-out. As in the case of specimens failed in fatigue at 0.1 Hz and 1 Hz, no delamination between the plies of the composite was observed.
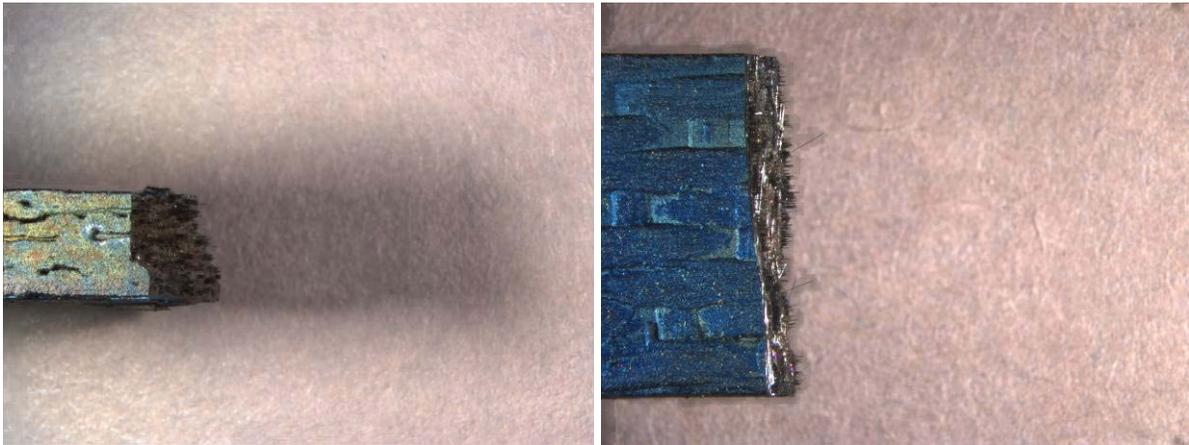
Figure 66: Optical micrographs of specimen P3-3 tested in fatigue at 10 Hz in air at 1200 ^{o}C. σmax = 100 MPa, Nf = 96,721, tf = 2.69 h.
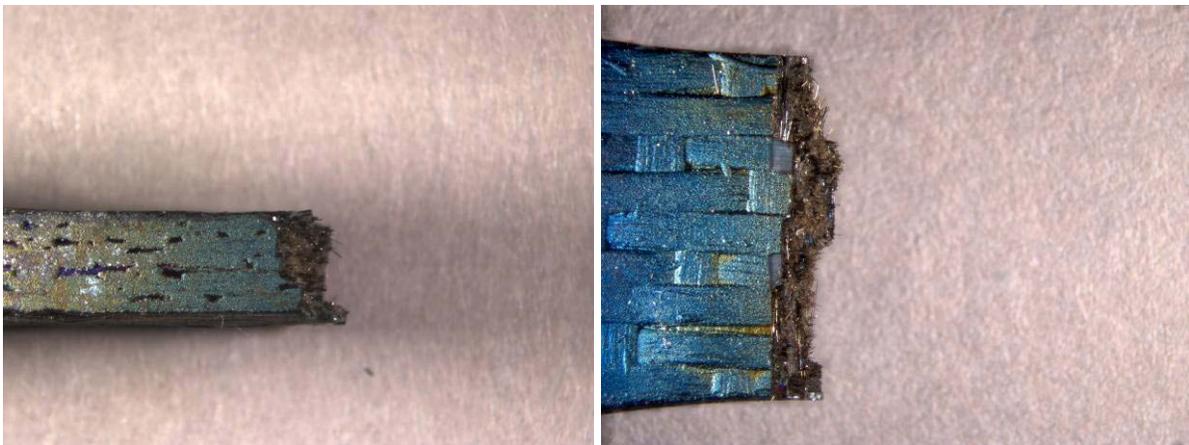
Figure 67: Optical micrographs of specimen P2-5 tested in fatigue at 10 Hz in air at 1200 ^{o}C. σmax = 80 MPa, Nf = 200,000, tf = 5.561 h.
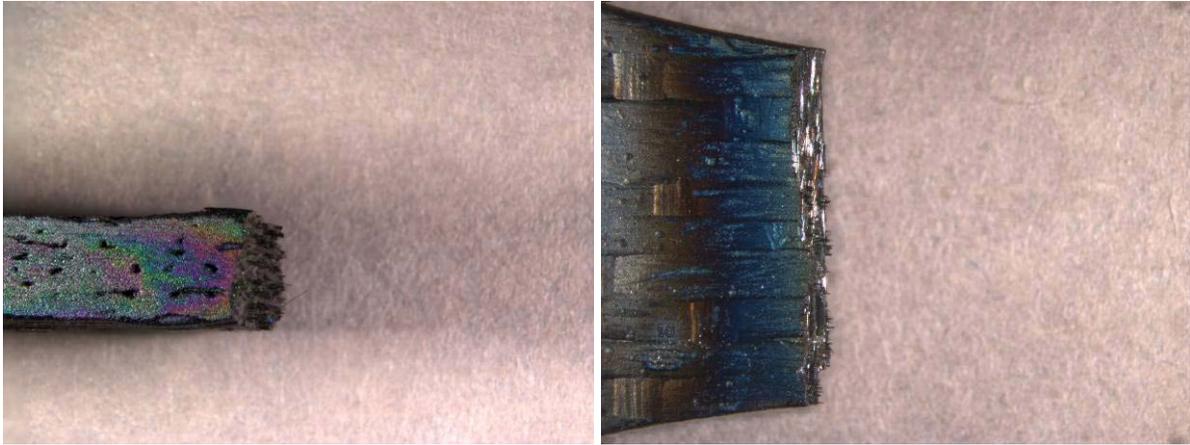
Figure 68: Optical micrographs of specimen P3-4 tested in fatigue at 10 Hz in steam at 1200 ᵒC. σmax = 80 MPa, Nf = 3,451, tf = 0.93 h.
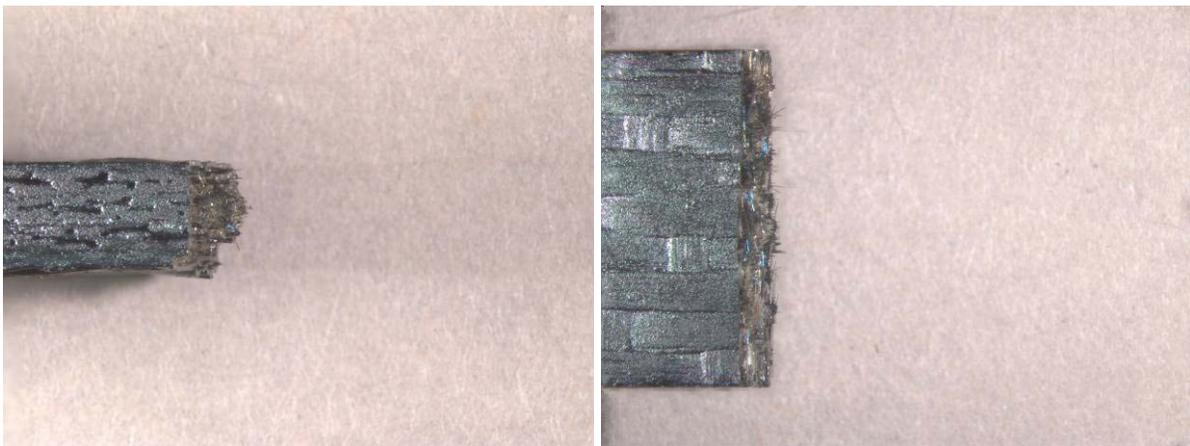
Figure 69: Optical micrographs of specimen P3-6 tested in fatigue at 0.1 Hz in steam at 1200 ᵒC. σmax = 60 MPa, Nf = 200,000, tf = 5.56 h.

The micrographs of the fracture surfaces produced in the 10 Hz tests display features not seen in the fracture surfaces produced in the 0.1 Hz or 1 Hz tests. SEM micrographs in Figure 70 (D) show what appear to be small, dark spots on the face of the fiber. Near these spots, the gap left by the BN fiber coating, which is normally very smooth and of even thickness, is rough and irregular. It is possible that the higher fatigue rate caused the fibers to slide across the

interface and abrade the adjacent matrix. This abrasion could have deformed the edges of the interface and at the same time produced matrix dust which settled on the facture surface.

In Figure 71 (C) and (D), a matrix crack is seen growing towards the "flash" SiC layer/SiC matrix boundary, then deflecting a short distance along the boundary in both directions, finally propagating through the "flash" SiC layer and bridging directly along the fiber. The holes inside individual fibers are also visible in these images.

When viewing the micrographs of the specimens tested in steam even more changes became apparent. In Figure 72 (C) and (D), severe degradation of the BN fiber coating is seen. Glassy bubbles have formed along the BN fiber coating at the fracture surface.

Figure 74 shows an overall view of the fracture surface of P3-6 which achieved fatigue run-out of 2 x 10^5 cycles in steam. The depth of the environmental intrusion is approximated by the dashed line. Overall fracture surface micrographs for the remaining specimens are included in Appendix A.

A closer look at the transition zone between the oxidized region and the brittle fracture zone in the interior of the specimen reveals material which has sloughed off the surrounding areas and flowed onto the fracture surfaces of the 0^0 fibers (seen in Figure 73 (C)). Additionally, it is seen in the lower right hand corner of Figure 73 (D) the "flash" SiC layer between the two fibers has cracked and is sloughing off. This sloughing may be the result of multiple brittle fractures and comminution of the ceramic constituents of the overall composite.

Unfortunately, the SEM micrographs of the polished sections of the specimens tested in fatigue at 10 Hz, Figures 75-78, do not offer additional insight. The images of the polished sections look very similar to those of the as-processed material and of the specimens tested at 0.1 Hz and 1.0 Hz.
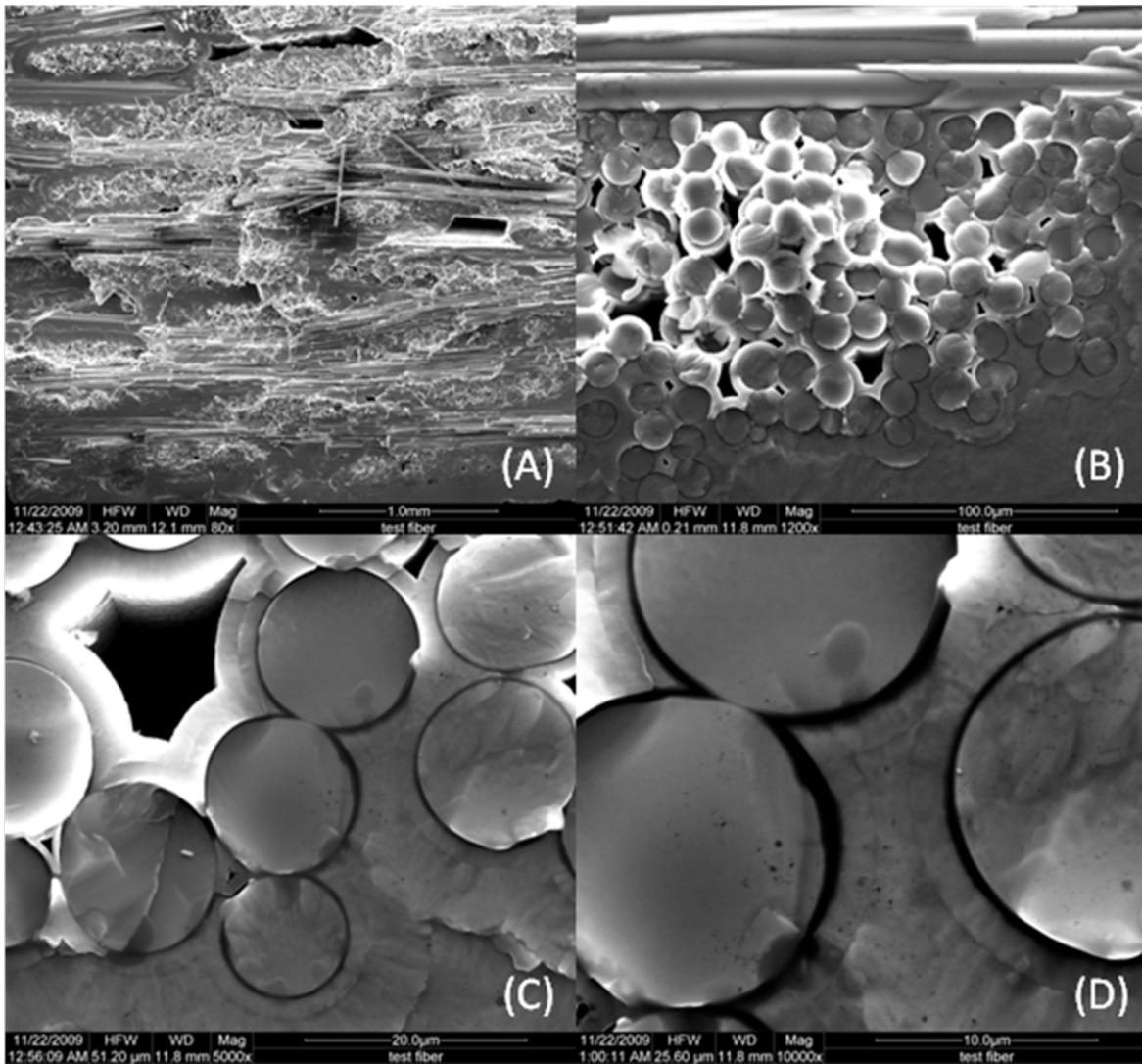
Figure 70: SEM micrographs of the fracture surface of specimen P3-3 tested in fatigue at 10 Hz in air at 1200 ^{o}C. σmax = 100 MPa, Nf = 96,721, tf = 2.69 h.
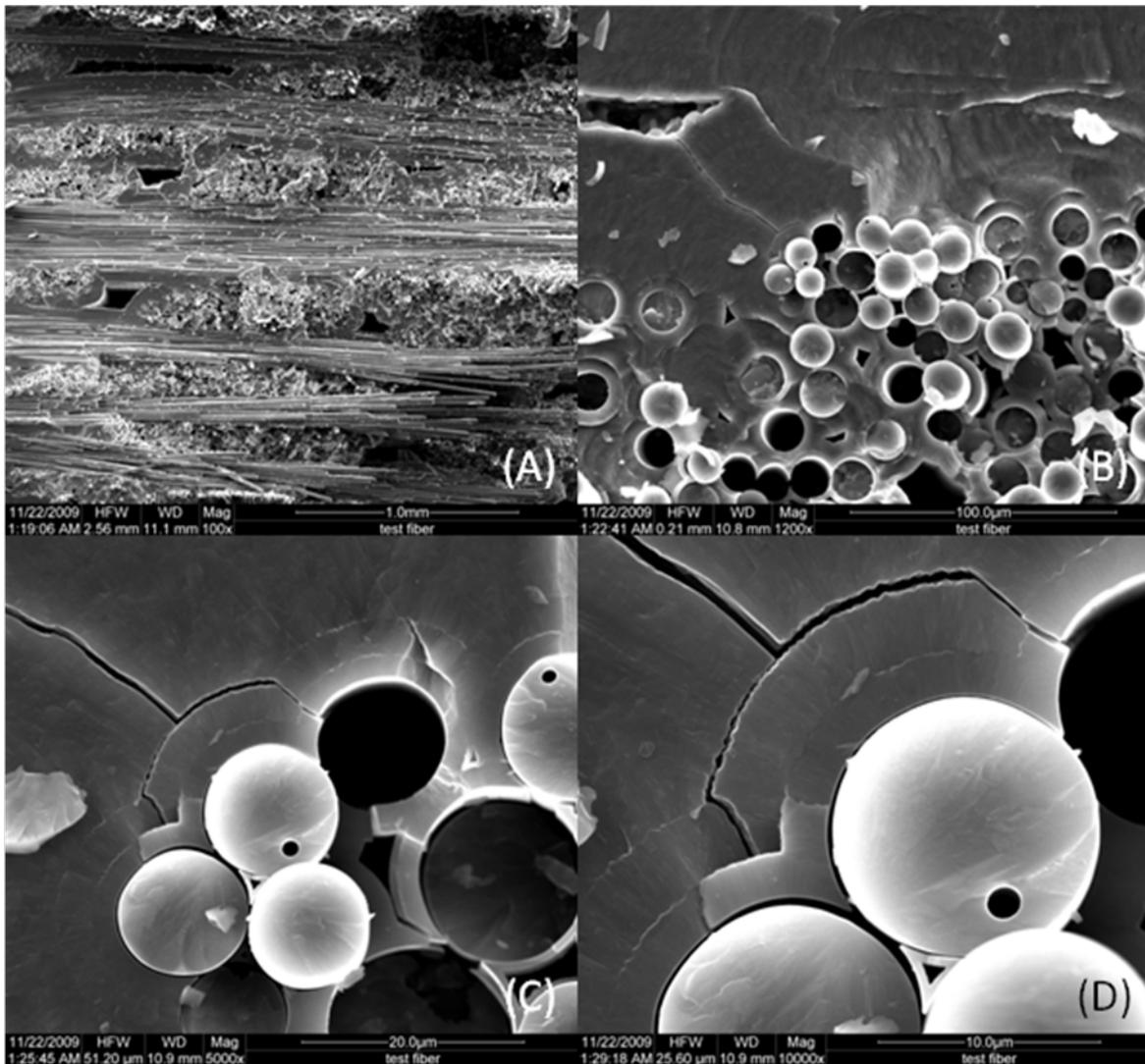
Figure 71: SEM micrographs of the fracture surface of specimen P2-5 tested in fatigue at 10 Hz in air at 1200 °C. σmax = 80 MPa, Nf = 200,000, tf = 5.56 h.
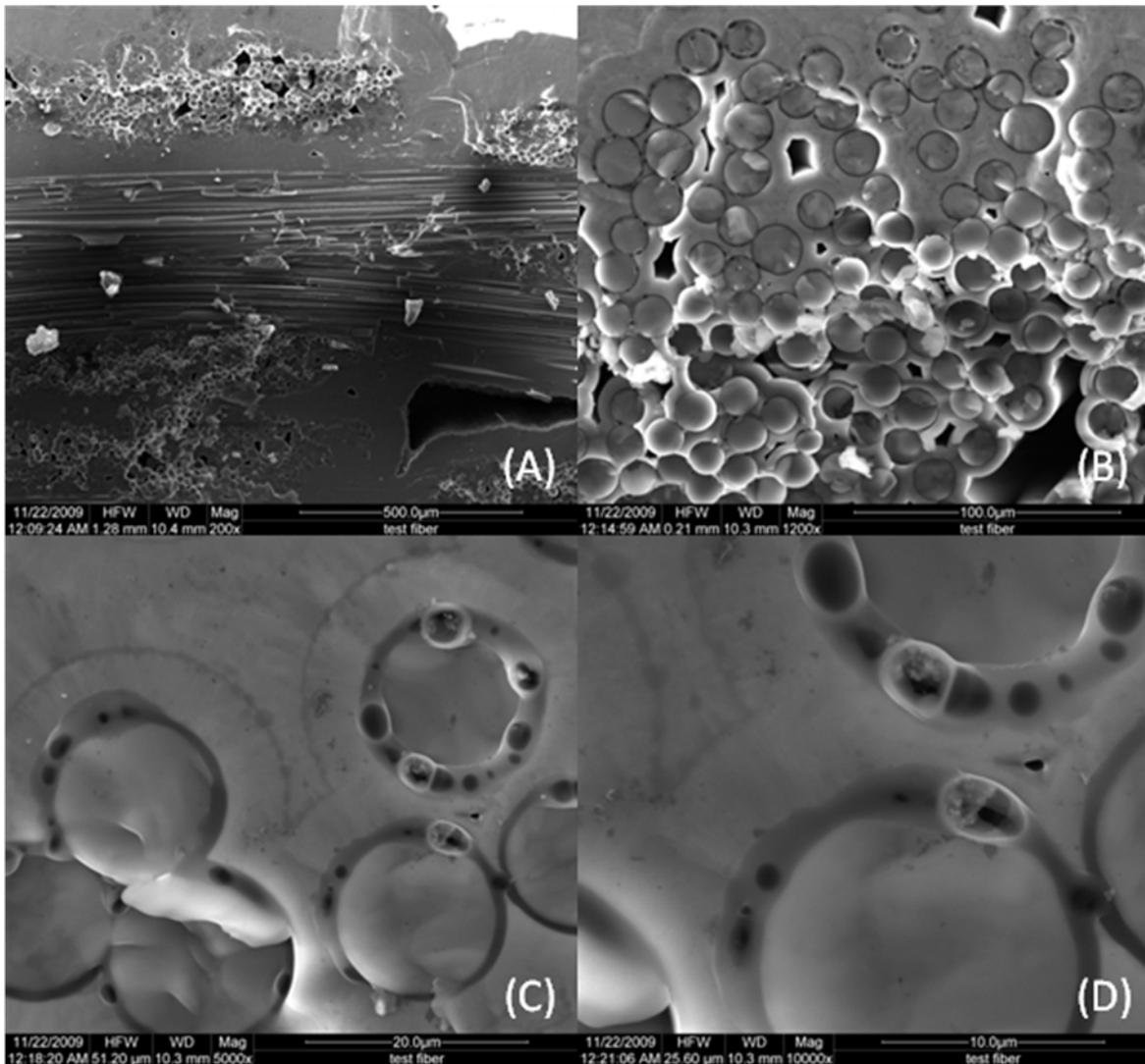
Figure 72: SEM micrographs of the fracture surface of specimen P3-4 tested in fatigue at 10 Hz in steam at 1200 ^{o}C. σmax = 80 MPa, Nf = 33,451, tf = 0.93 h.
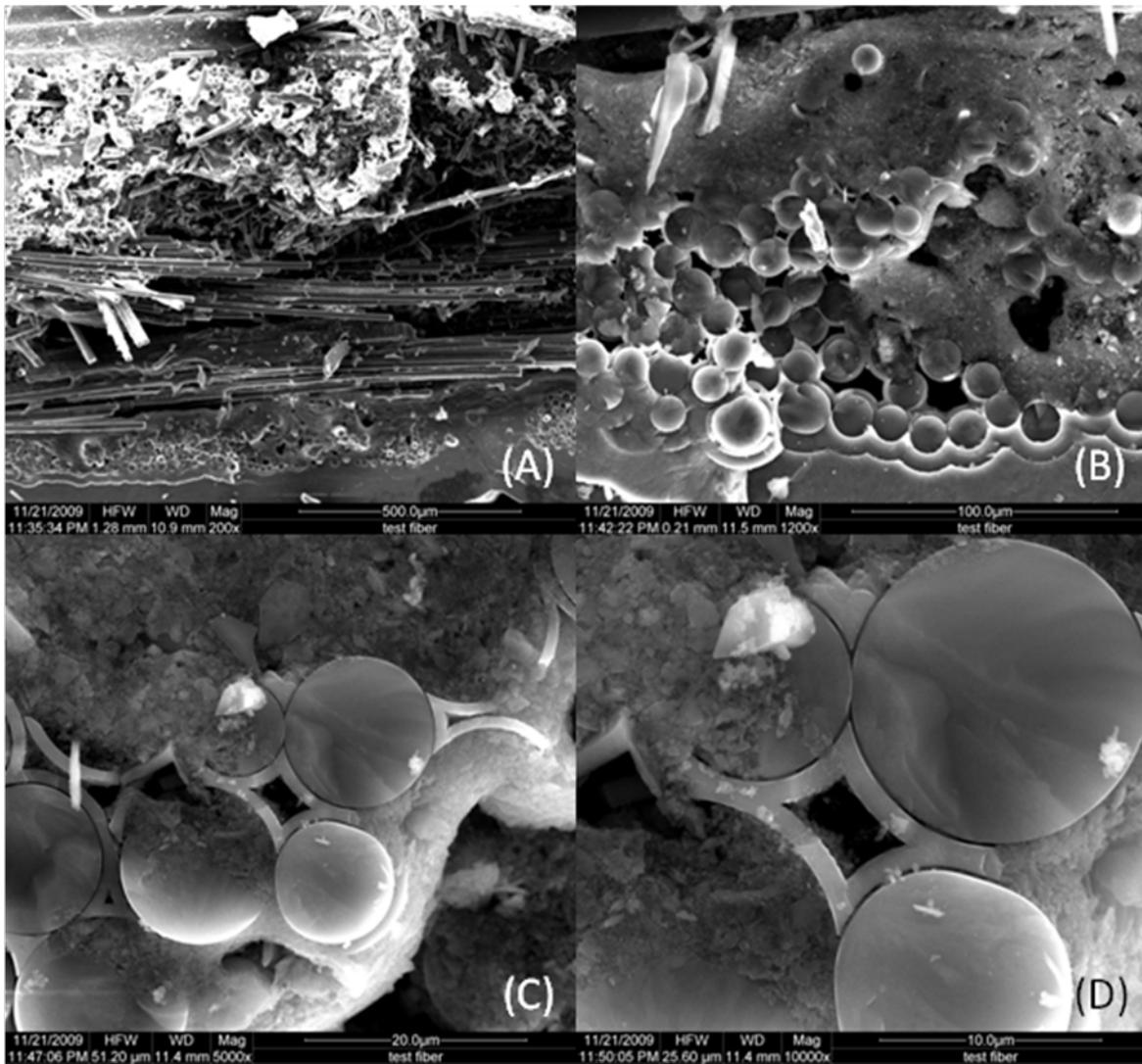
Figure 73: SEM micrographs of the fracture surface of specimen P3-6 tested in fatigue at 10 Hz in steam at 1200 °C. σmax = 60 MPa, Nf = 200,000, tf = 5.56 h.

Figure 74: Compiled SEM micrographs of total P3-6 fracture surface after failure during 10 Hz fatigue testing at 1200 $^{\circ}$C in steam with σmax = 60 MPa. Environmental intrusion zone indicated by dotted line.
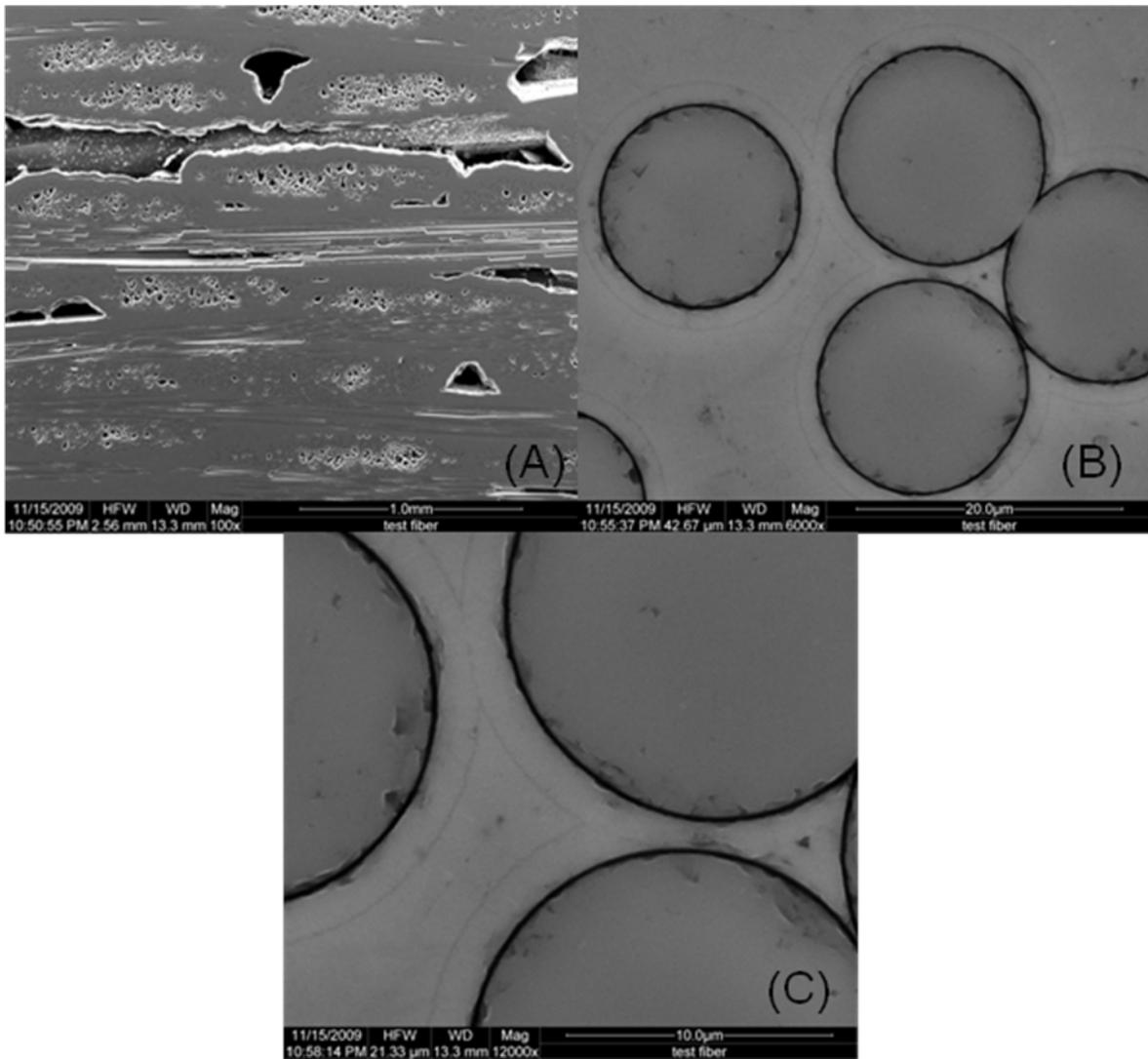
Figure 75: SEM micrographs of the polished surface of specimen P3-3 tested in fatigue at 10 Hz in air at 1200 °C. σmax = 100 MPa, Nf = 96,721, tf = 2.69 h.
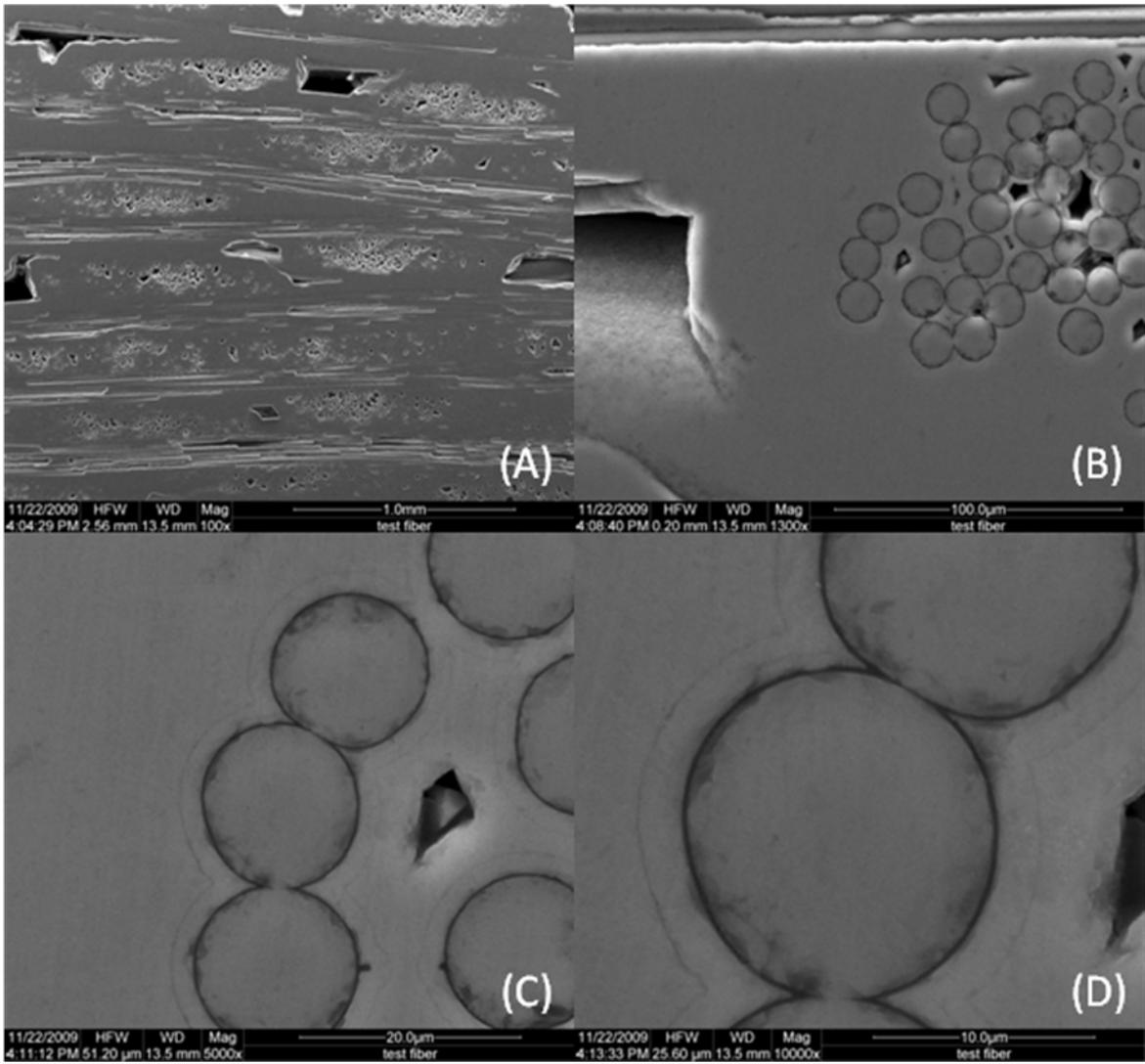
Figure 76: SEM micrographs of the polished surface of specimen P2-5 tested in fatigue at 10 Hz in air at 1200 ^{o}C. σmax = 80 MPa, Nf = 200,000, tf = 5.56 h.
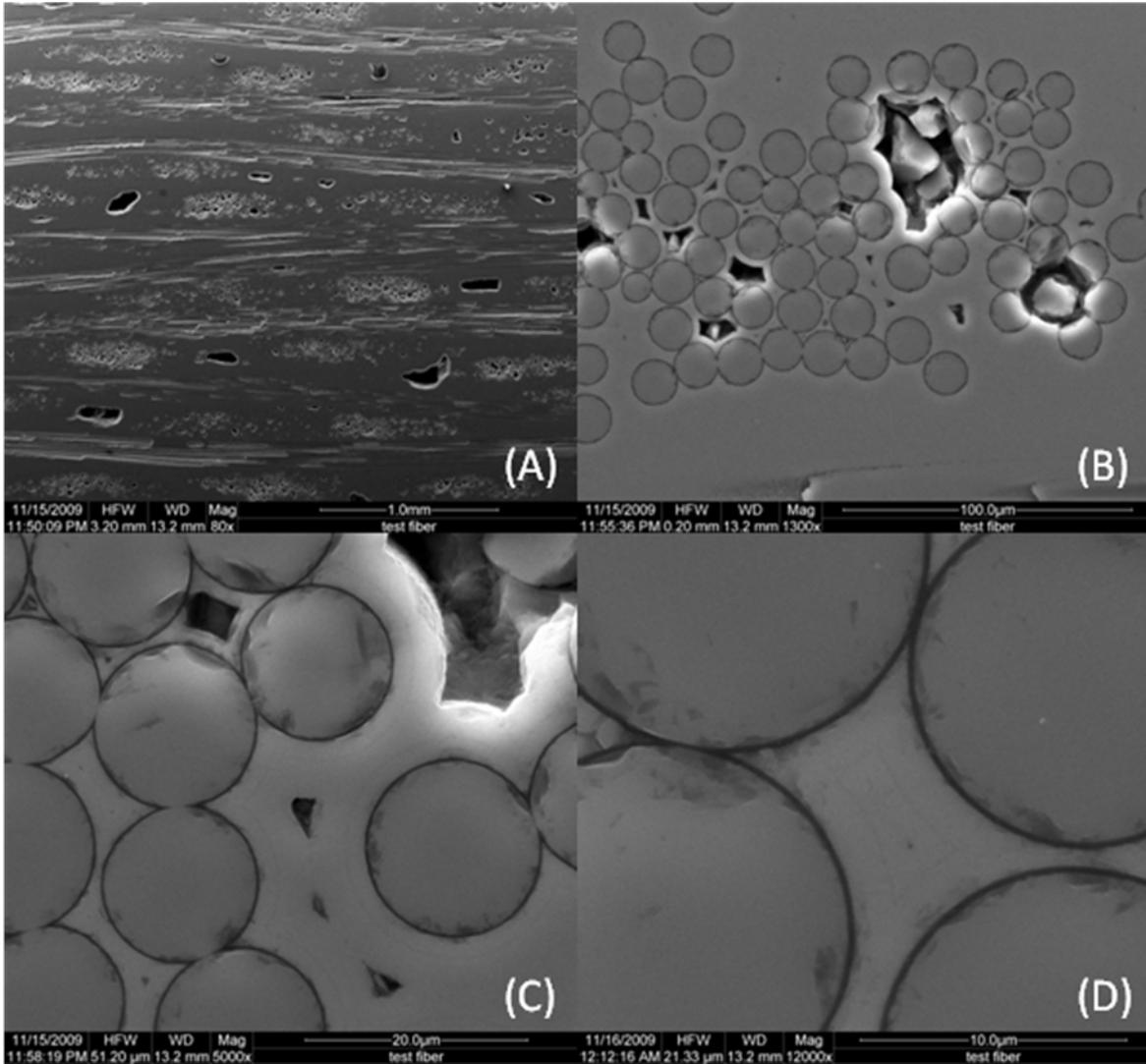
Figure 77: SEM micrographs of the fracture surface of specimen P3-4 tested in fatigue at 10 Hz in steam at 1200 $^{\circ}$C. σmax = 80 MPa, Nf = 33,451, tf = 0.93 h.
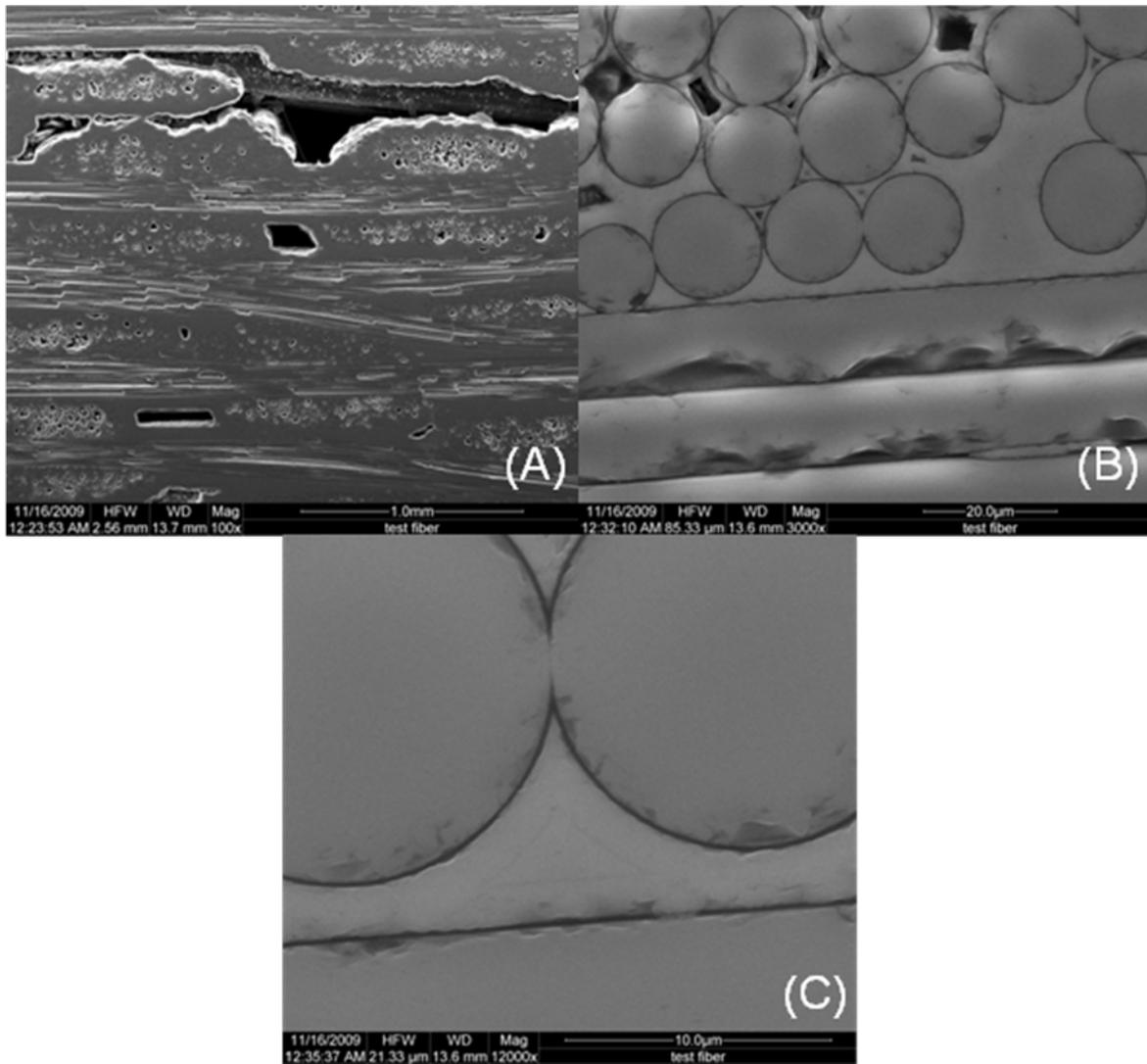
Figure 78: SEM micrographs of the fracture surface of specimen P3-6 tested in fatigue at 10 Hz in steam at 1200 ^{o}C. σmax = 60 MPa, Nf = 200,000, tf = 5.56 h.

V. Conclusions and Recommendations

5.1 Conclusions

The Hi-Nicalon/BN/SiC advanced CMC tested in this effort demonstrated excellent fatigue resistance in laboratory air at 1200 ^{0}C. Fatigue life of the CMC decreased as the fatigue stress increased. The presence of steam degraded the fatigue resistance of the material.

The Hi-Nicalon/BN/SiC CMC exhibited minimal strain ratcheting during fatigue testing. However, a reduction in stiffness with increasing fatigue cycles was observed. Fatigue frequency and/or environment appear to have little influence on the stiffness evolution with cycles.

Prior fatigue appeared to have no effect on the retained tensile strength of the Hi-Nicalon/BN/SiC. The reduction in retained modulus was limited to ~12%, irrespective of fatigue rate or fatigue environment.

No distinct trends could be discerned in the optical micrographs of the fracture surfaces of the specimens. The SEM micrographs of the fracture surfaces of the failed specimens showed increased oxidization at longer fatigue lifetimes in a steam environment. However, in all the failed specimens the oxidation was confined to a small region around the perimeter of the specimen, inside of which the specimen failed with little or no effects of oxidization. The SEM micrographs of the fracture surfaces of the specimens subjected to fatigue at 10 Hz suggest that additional damage to the composite constituents occurs at higher fatigue rates.

5.2 Recommendations

  To reduce the effects of panel-to-panel variability, additional tensile tests should be carried out to obtain more reliable tensile property values. Additionally, more fatigue tests at different fatigue levels should be conducted at each of the fatigue frequencies investigated in this study to obtain more complete S-N curves.
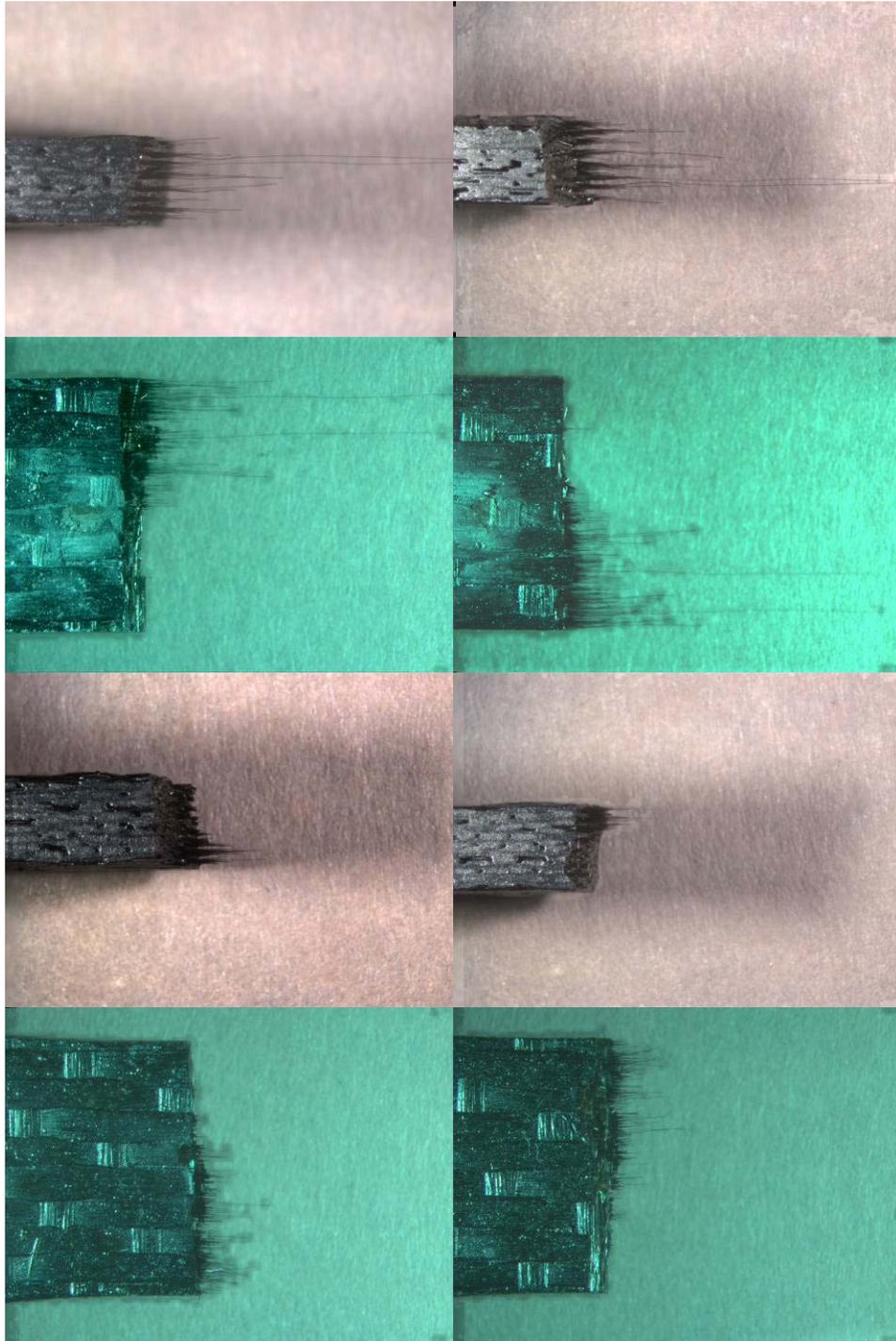
Figure 79: Optical micrographs of specimen P1-1 tested in fatigue at 1.0 Hz in steam at 1200 ^{o}C. σmax = 100 MPa, Nf = 11,447, tf = 3.18 h.
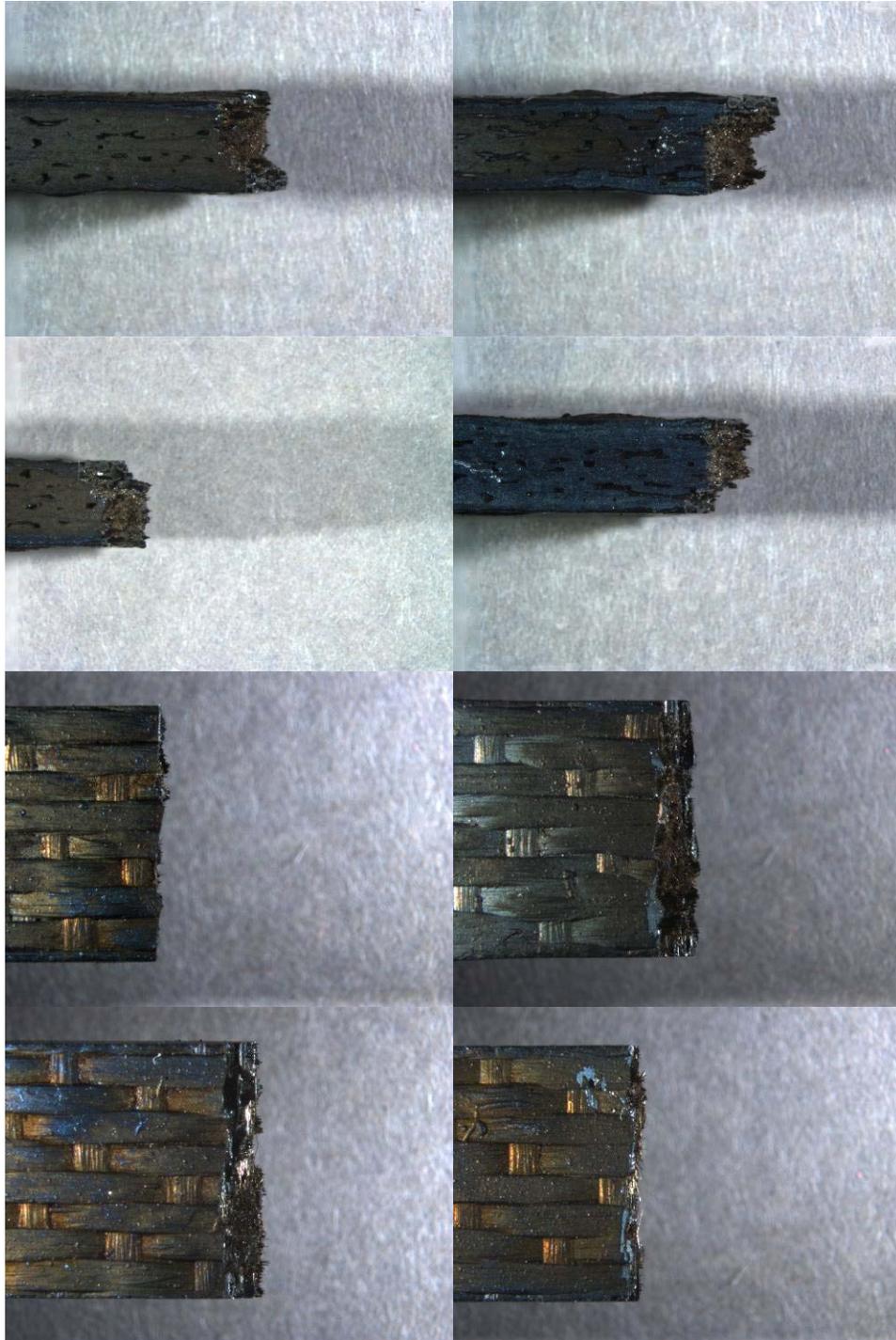
Figure 80: Optical Micrographs of the fracture surfaces produced in tensile test to failure conducted at 0.05mm/sec at 1200 °C in air on specimen P1-3.
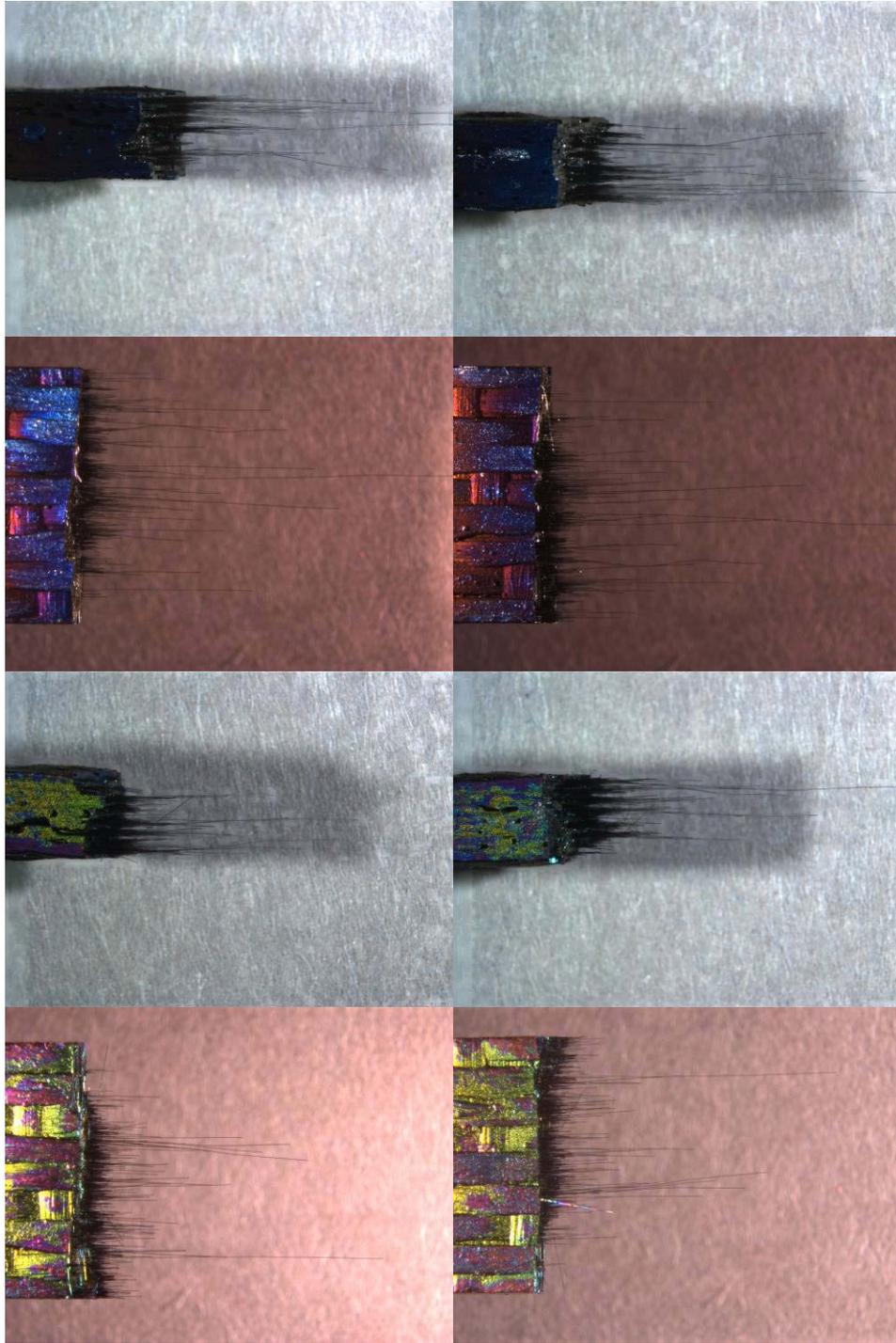
Figure 81: Optical micrographs of specimen P1-4 tested in fatigue at 1.0 Hz in air at 1200 °C. σmax = 120 MPa, Nf = 3766, tf = 1.05 h.
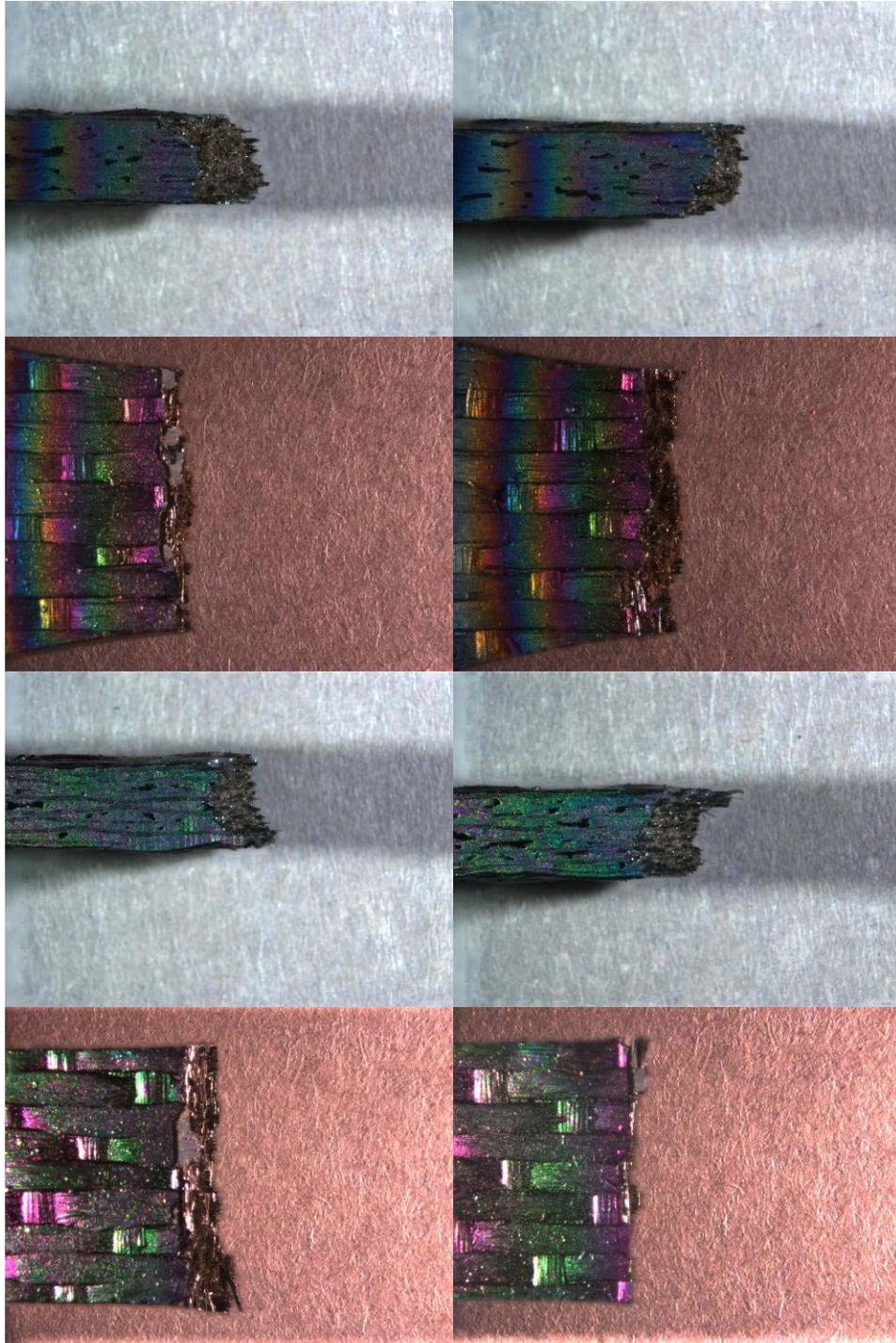
Figure 82: Optical micrographs of specimen P1-5 tested in fatigue at 1.0 Hz in air at 1200 °C. σmax = 80 MPa, Nf = 200,000, tf = 55.56 h.
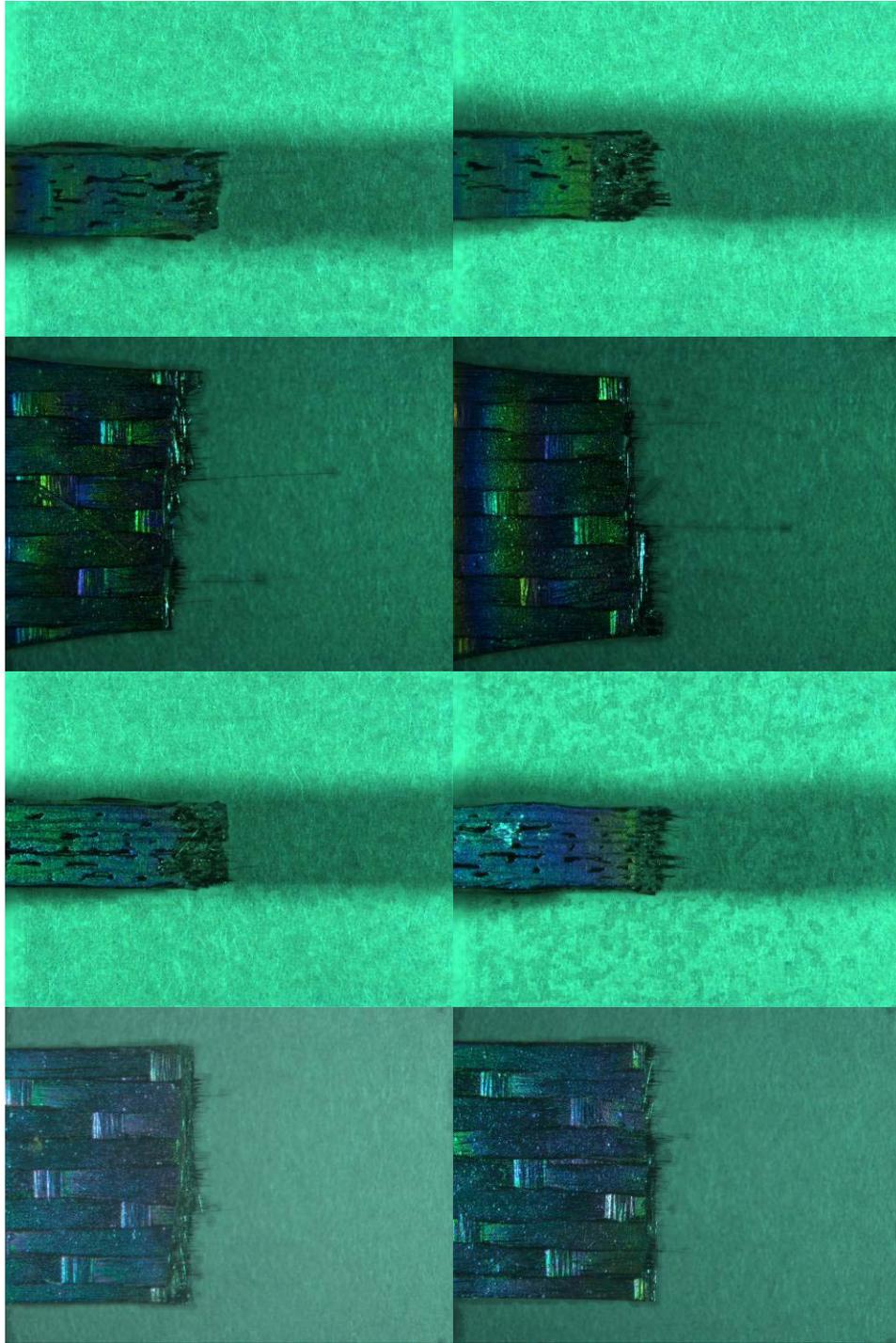
Figure 83: Optical micrographs of specimen P1-6 tested in fatigue at 1.0 Hz in air at 1200 °C. σmax = 100 MPa, Nf = 94,022, tf = 26.12 h.
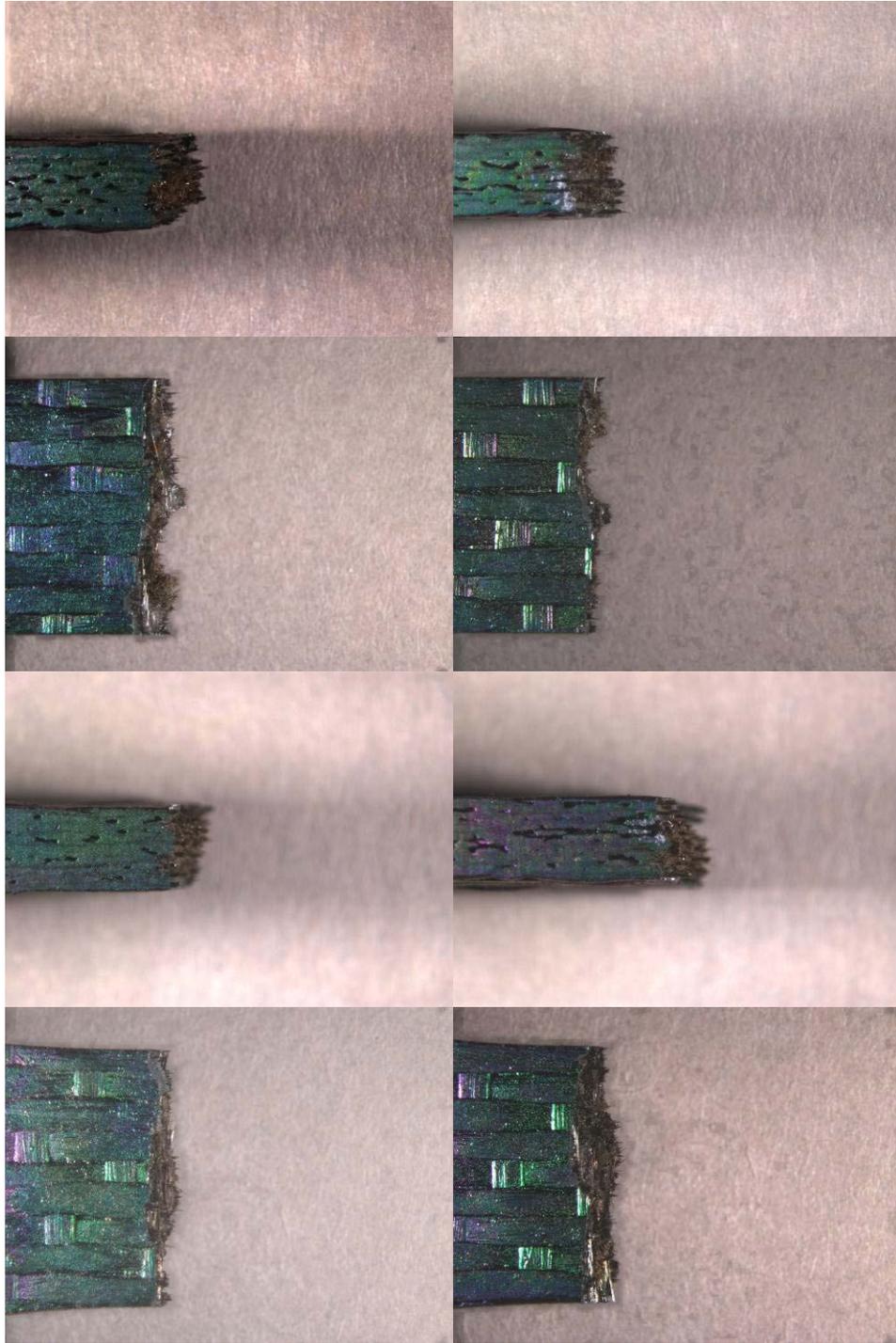
Figure 84: Optical micrographs of specimen P1-7 tested in fatigue at 1.0 Hz in air at 1200 °C. σmax = 100 MPa, Nf = 200,000, tf = 55.56 h.
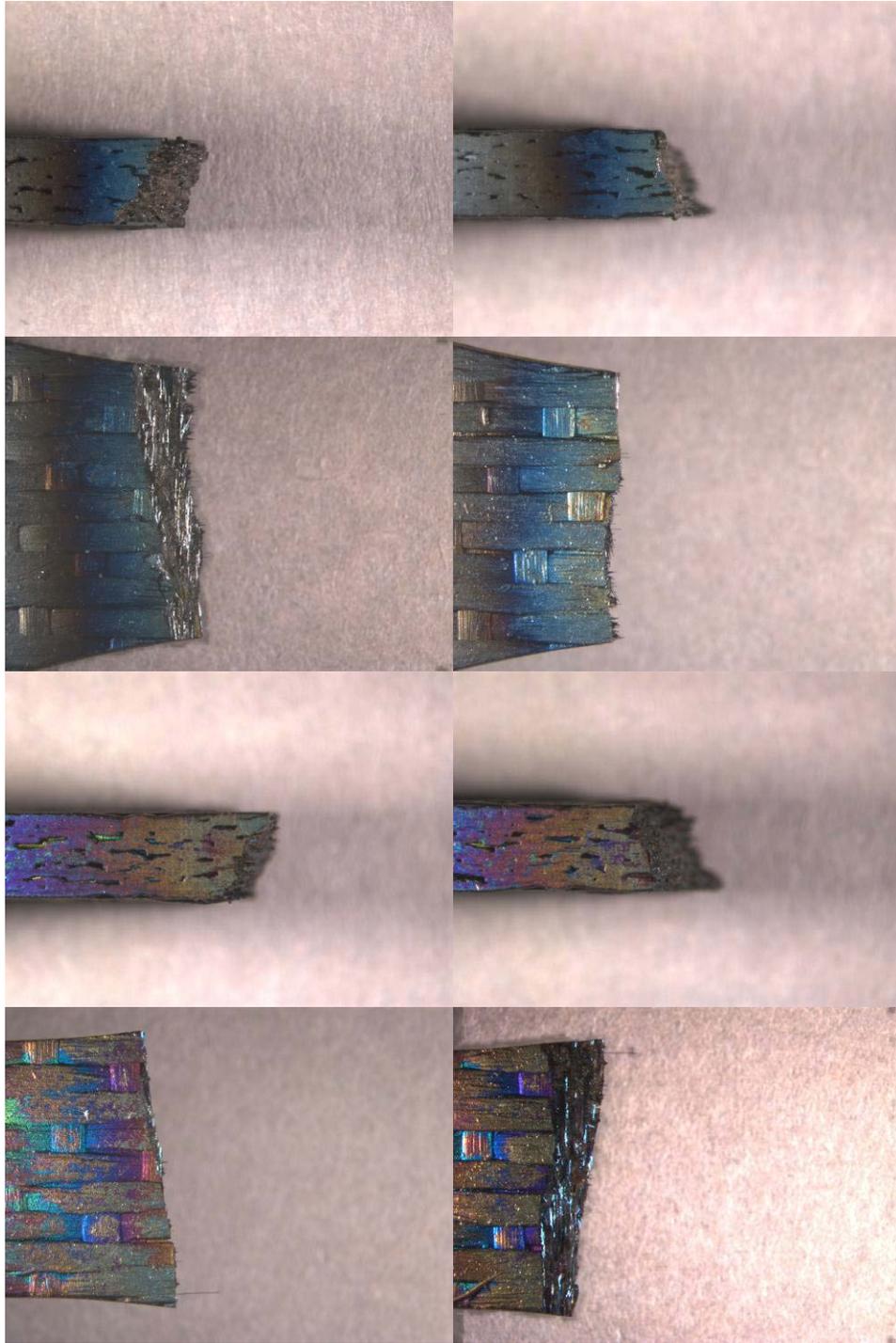
Figure 85: Optical micrographs of specimen P1-8 tested in fatigue at 1.0 Hz in air at 1200 °C. σmax = 110 MPa, Nf = 59,641 tf = 16.57 h.
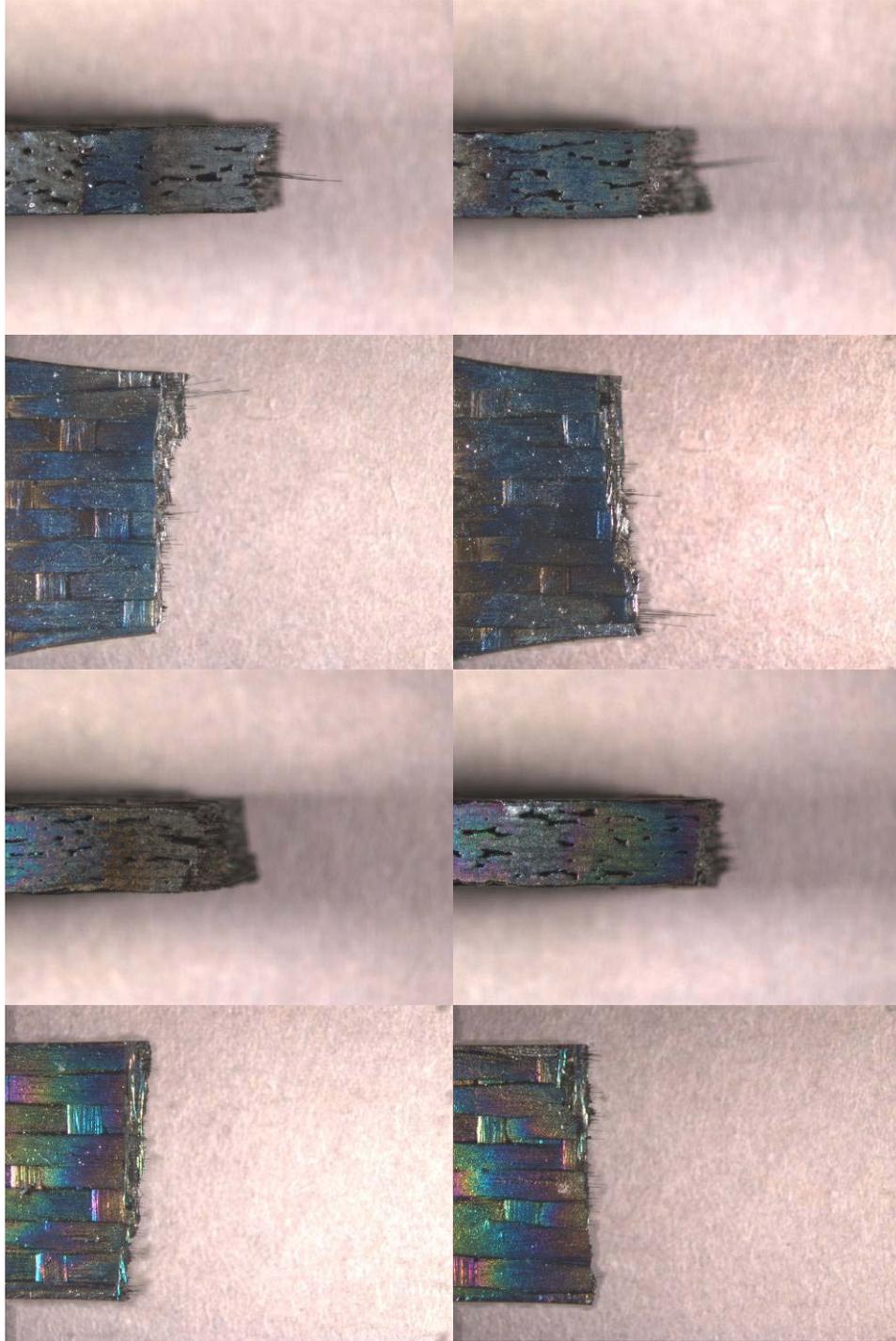
Figure 86: Optical micrographs of specimen P1-9 tested in fatigue at 1.0 Hz in steam at 1200 ^{o}C. σmax = 110 MPa, Nf = 5620, tf = 1.56 h.
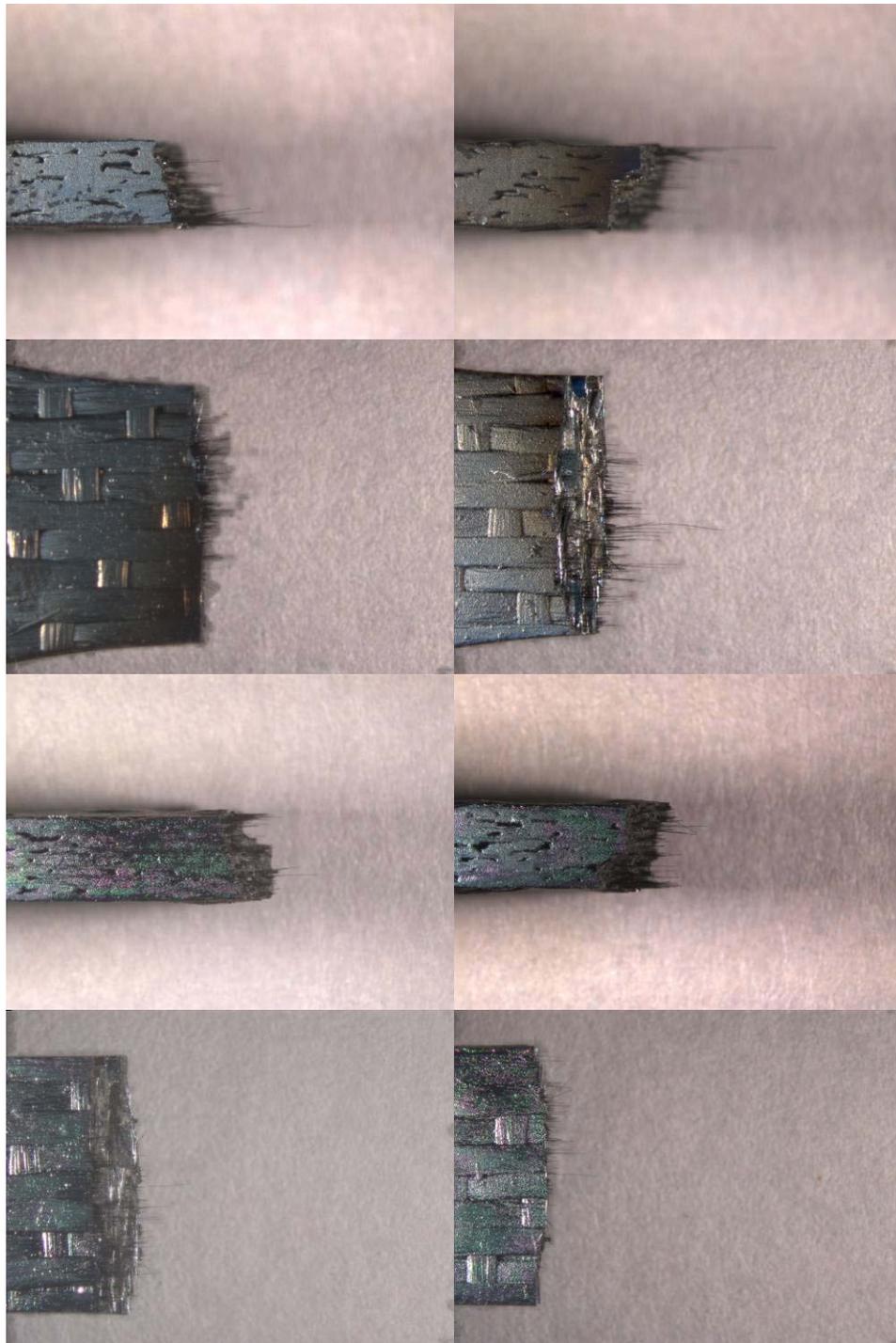
Figure 87: Optical micrographs of specimen P2-1 tested in fatigue at 1.0 Hz in steam at 1200 ^{o}C. σmax = 100 MPa, Nf = 1128, tf = 0.31 h.
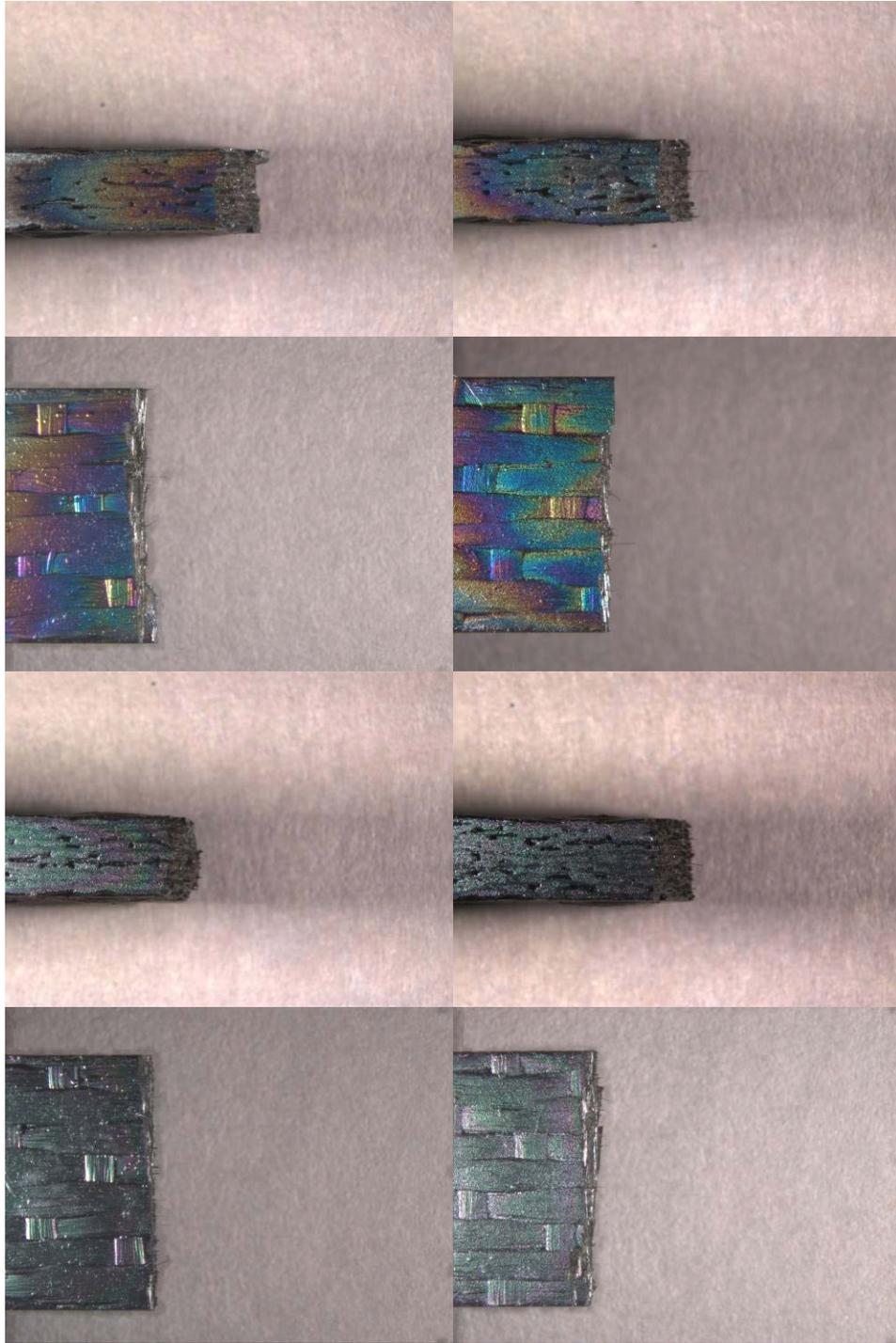
Figure 88: Optical micrographs of specimen P2-3 tested in fatigue at 1.0 Hz in steam at 1200 ^{o}C. σmax = 100 MPa, Nf = 1650, tf = 0.46 h.
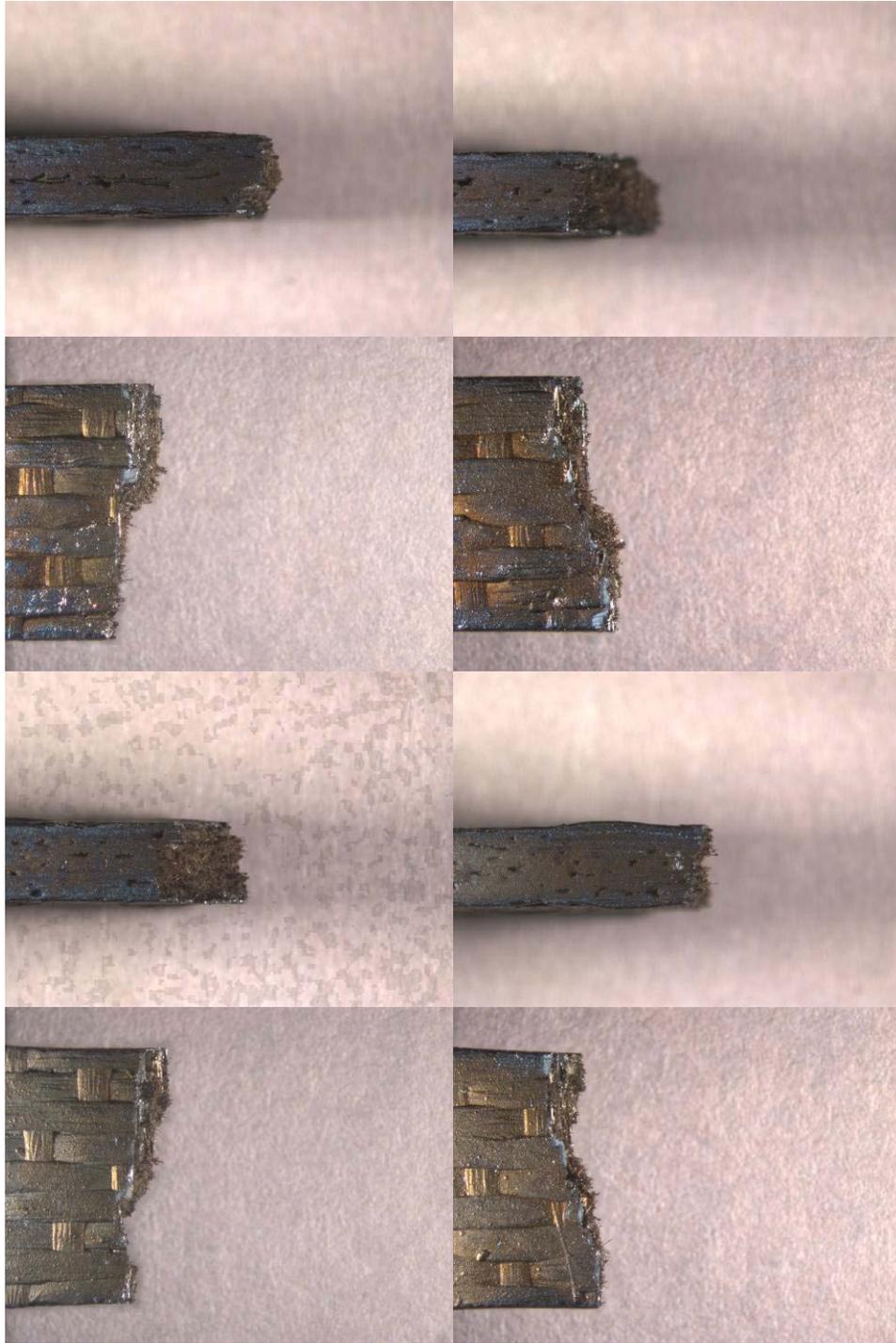
Figure 89: Optical Micrographs of the fracture surfaces produced in tensile test to failure conducted at 0.05mm/sec at 1200 ºC in air on specimen P2-4.
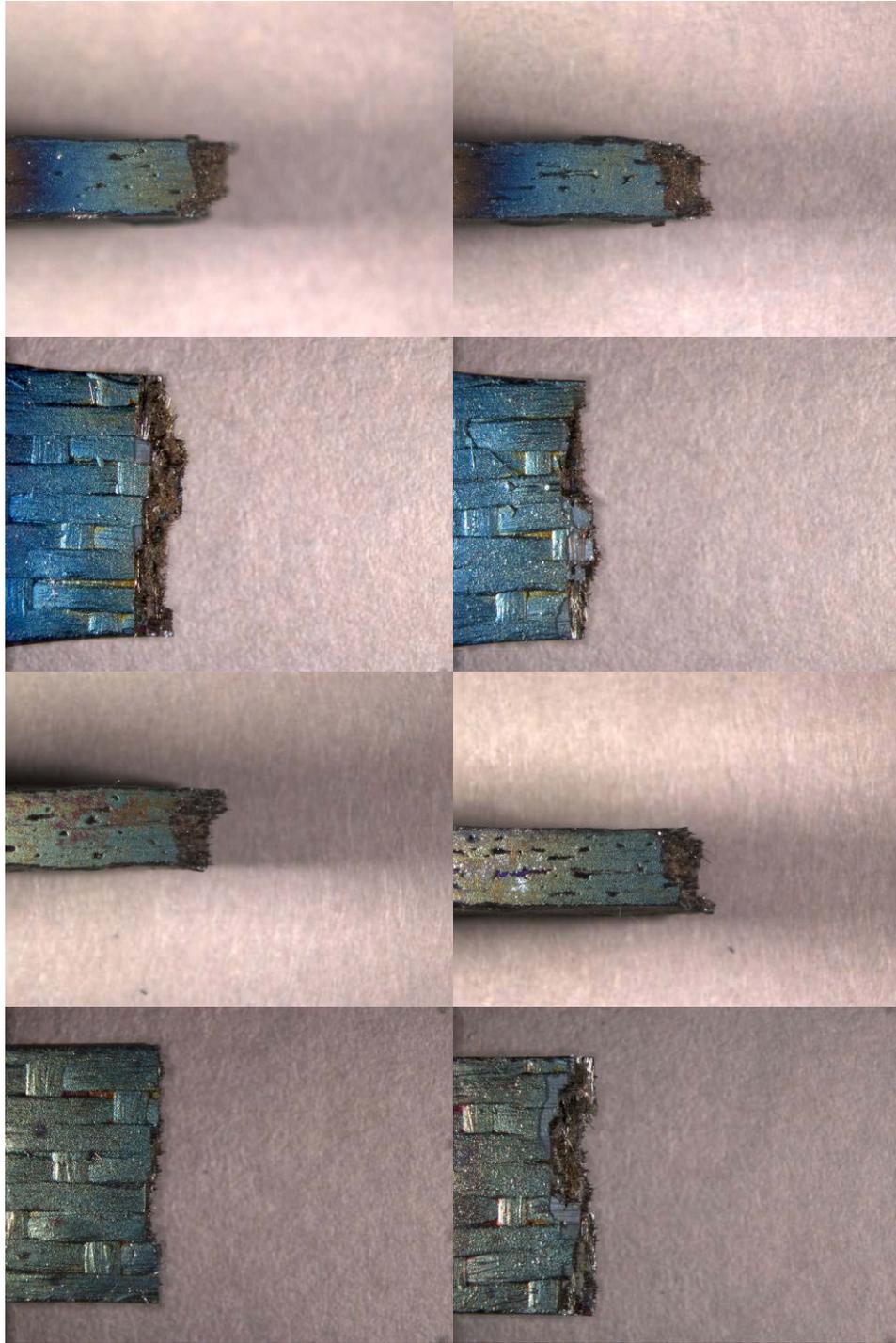
Figure 90: Optical micrographs of specimen P2-5 tested in fatigue at 10 Hz in air at 1200 °C. σmax = 80 MPa, Nf = 200,000, tf = 5.56 h.
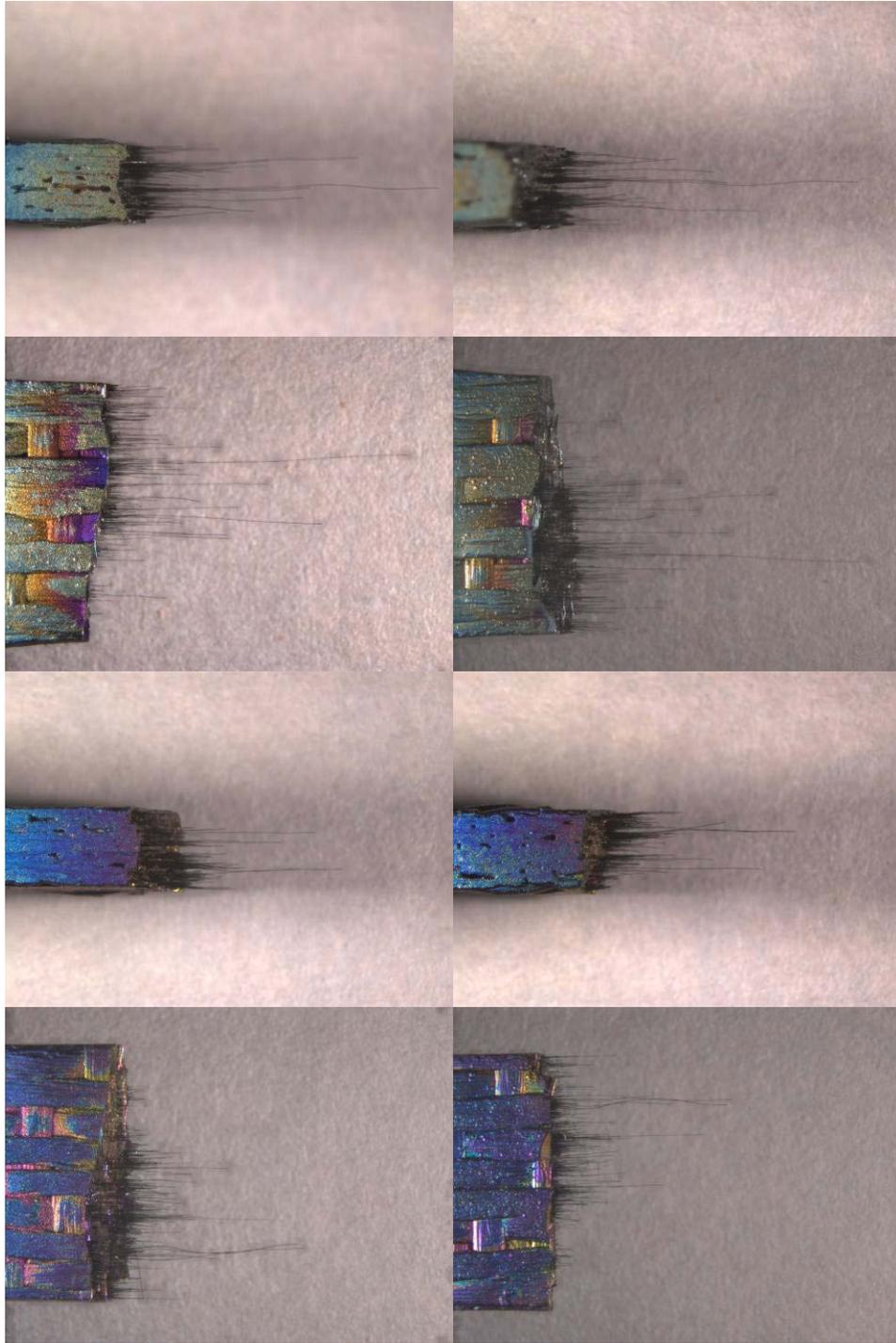
Figure 91: Optical micrographs of specimen P2-6 tested in fatigue at 0.1 Hz in air at 1200 °C. σmax = 120 MPa, Nf = 3780, tf = 10.5 h.
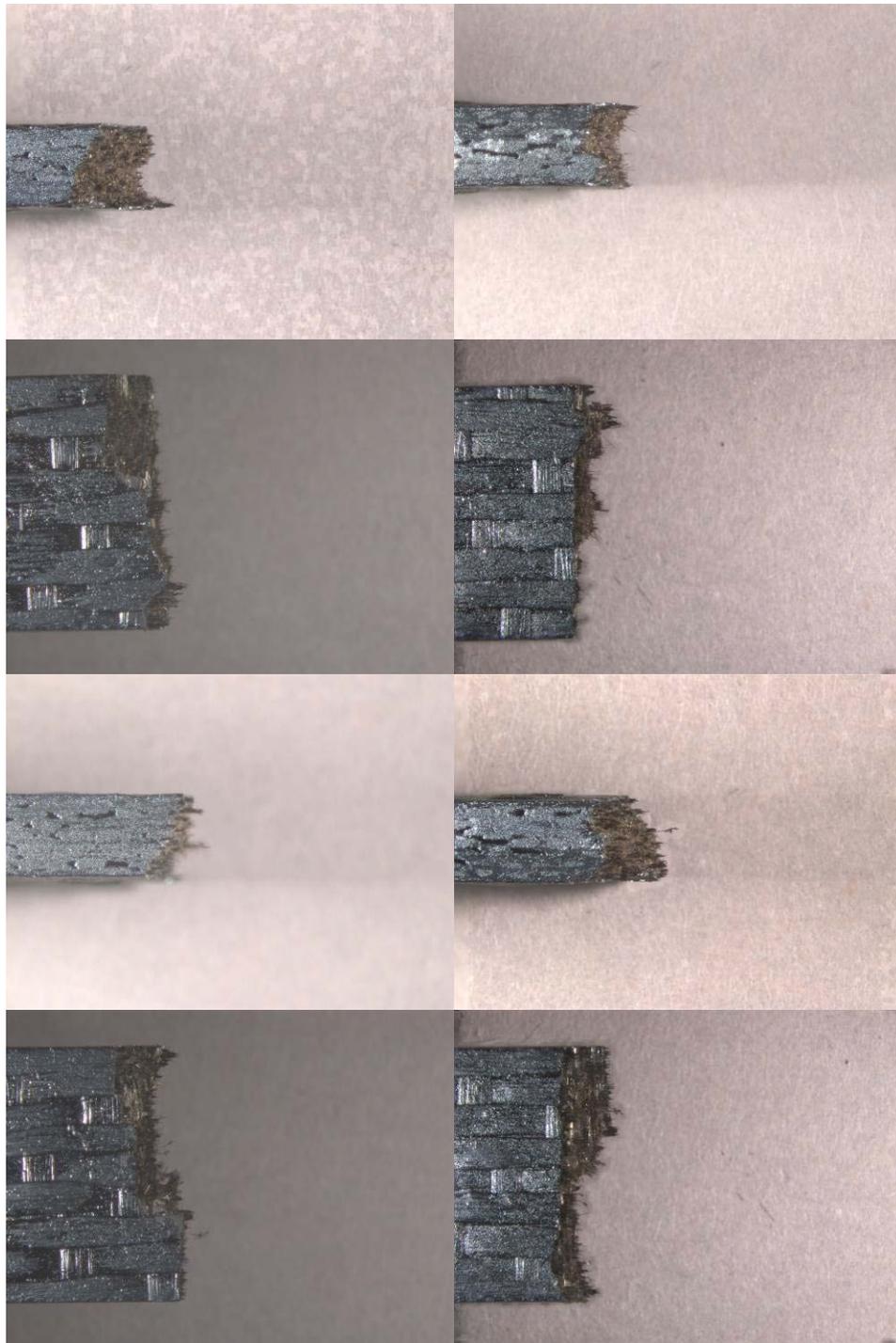
Figure 92: Optical micrographs of specimen P2-7 tested in fatigue at 0.1 Hz in air at 1200 ᵒC. σmax = 100 MPa, Nf = 100,000, tf = 277.78 h.
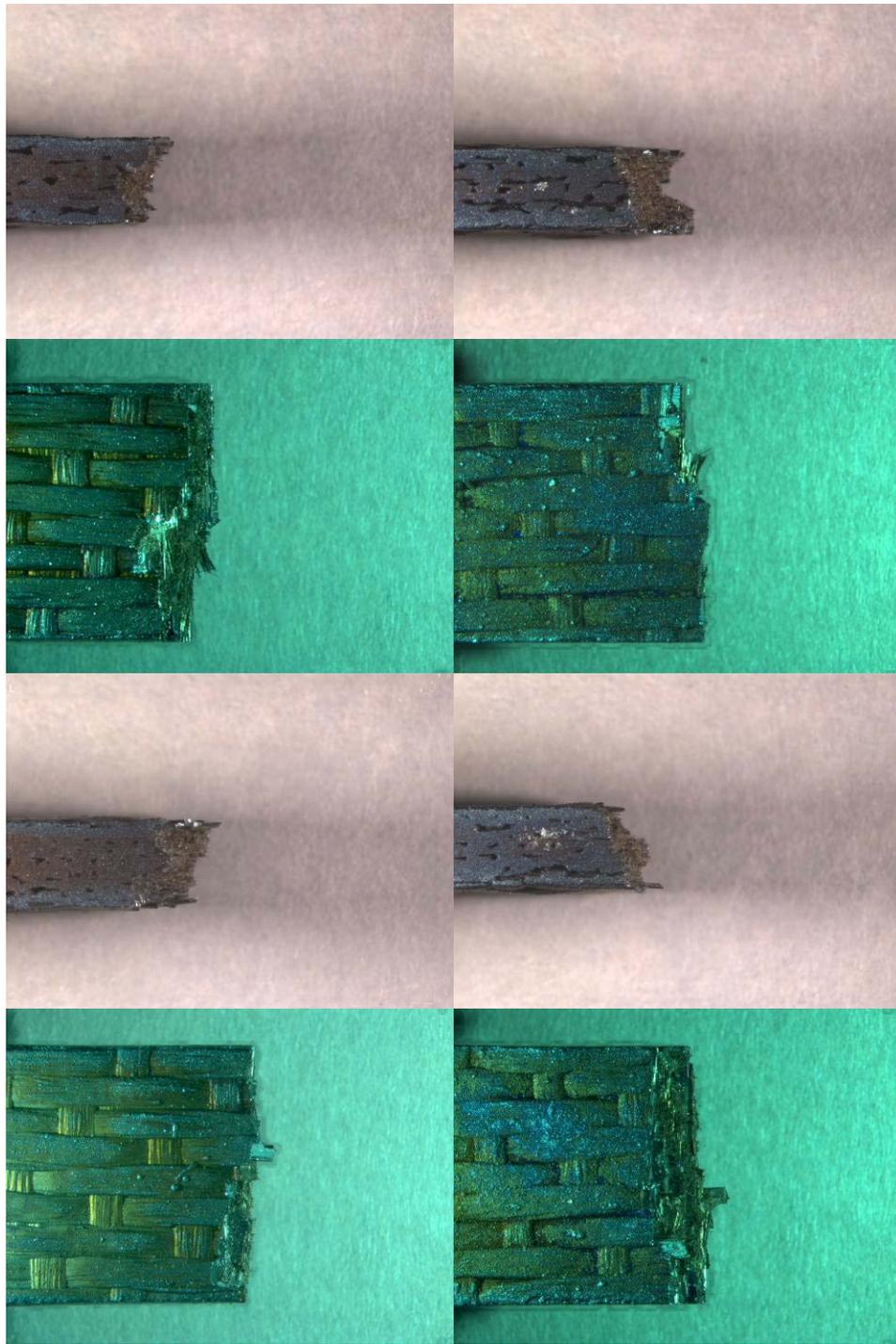
Figure 93: Optical Micrographs of the fracture surfaces produced in tensile test to failure conducted at 0.05mm/sec at 1200 °C in air on specimen P3-1.
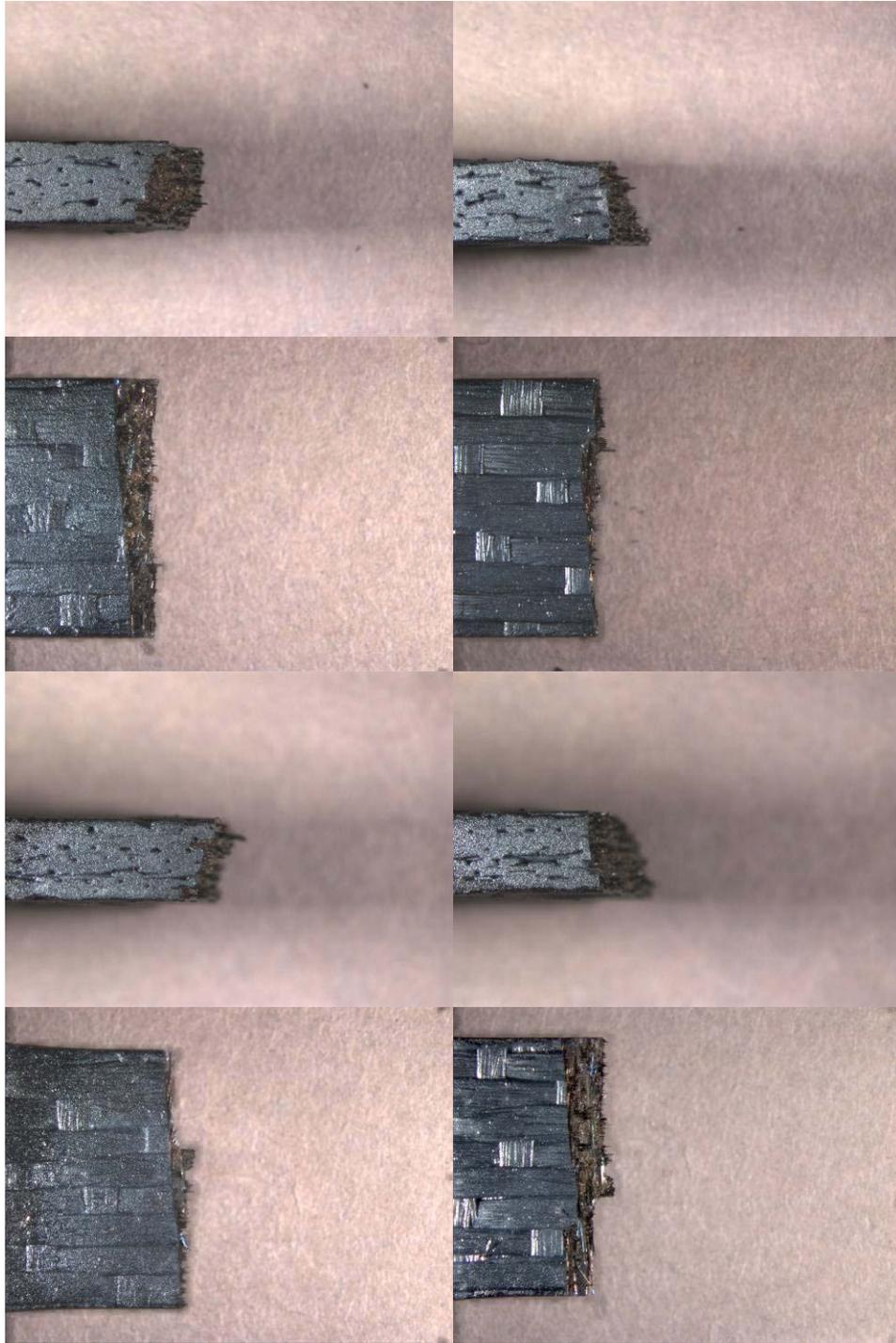
Figure 94: Optical micrographs of specimen P3-2 tested in fatigue at 1.0 Hz in steam at 1200 ^{o}C. σmax = 80 MPa, Nf = 200,000, tf = 55.56 h.
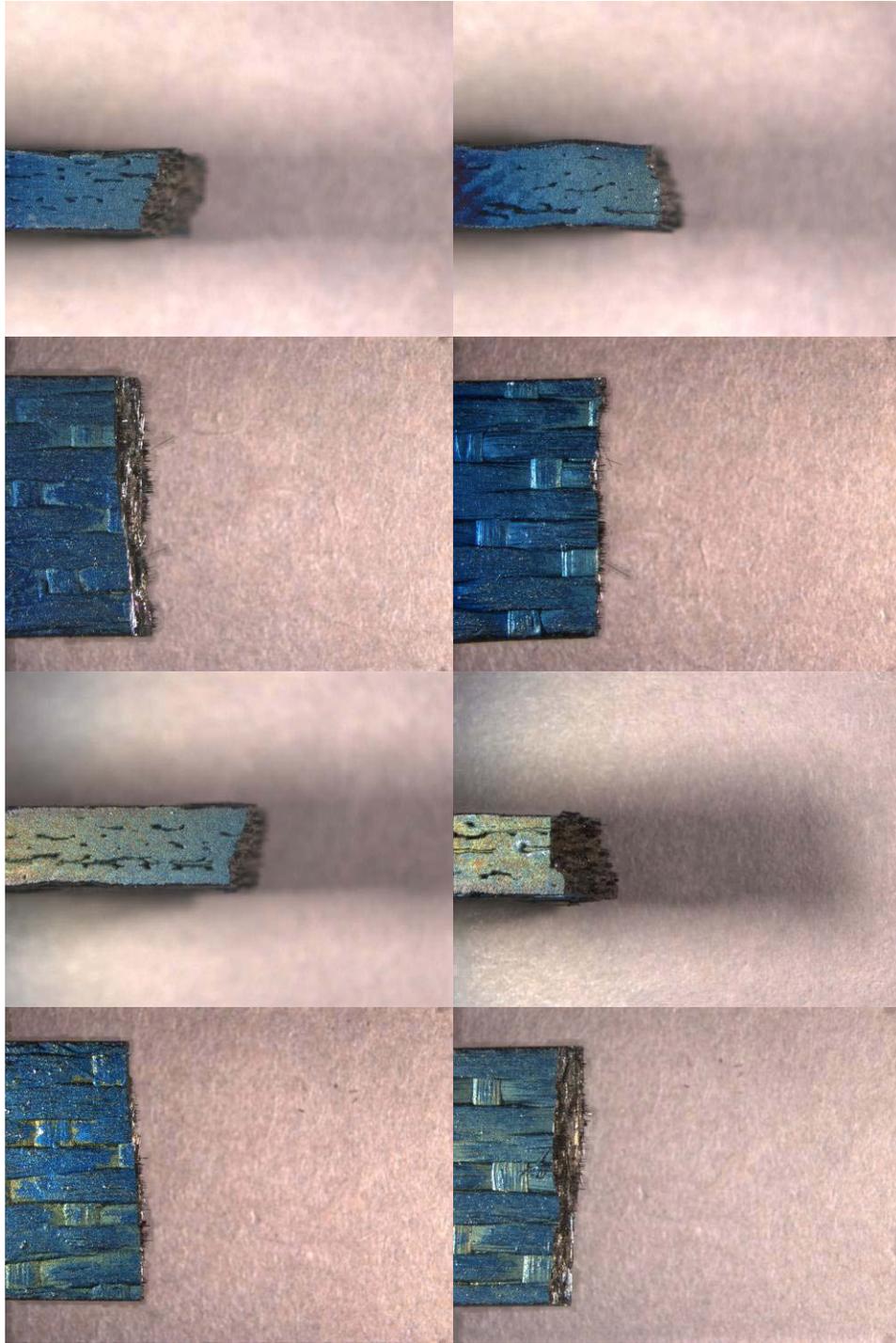
Figure 95: Optical micrographs of specimen P3-3 tested in fatigue at 10 Hz in air at 1200 °C. σmax = 100 MPa, Nf = 96,721, tf = 2.69 h.
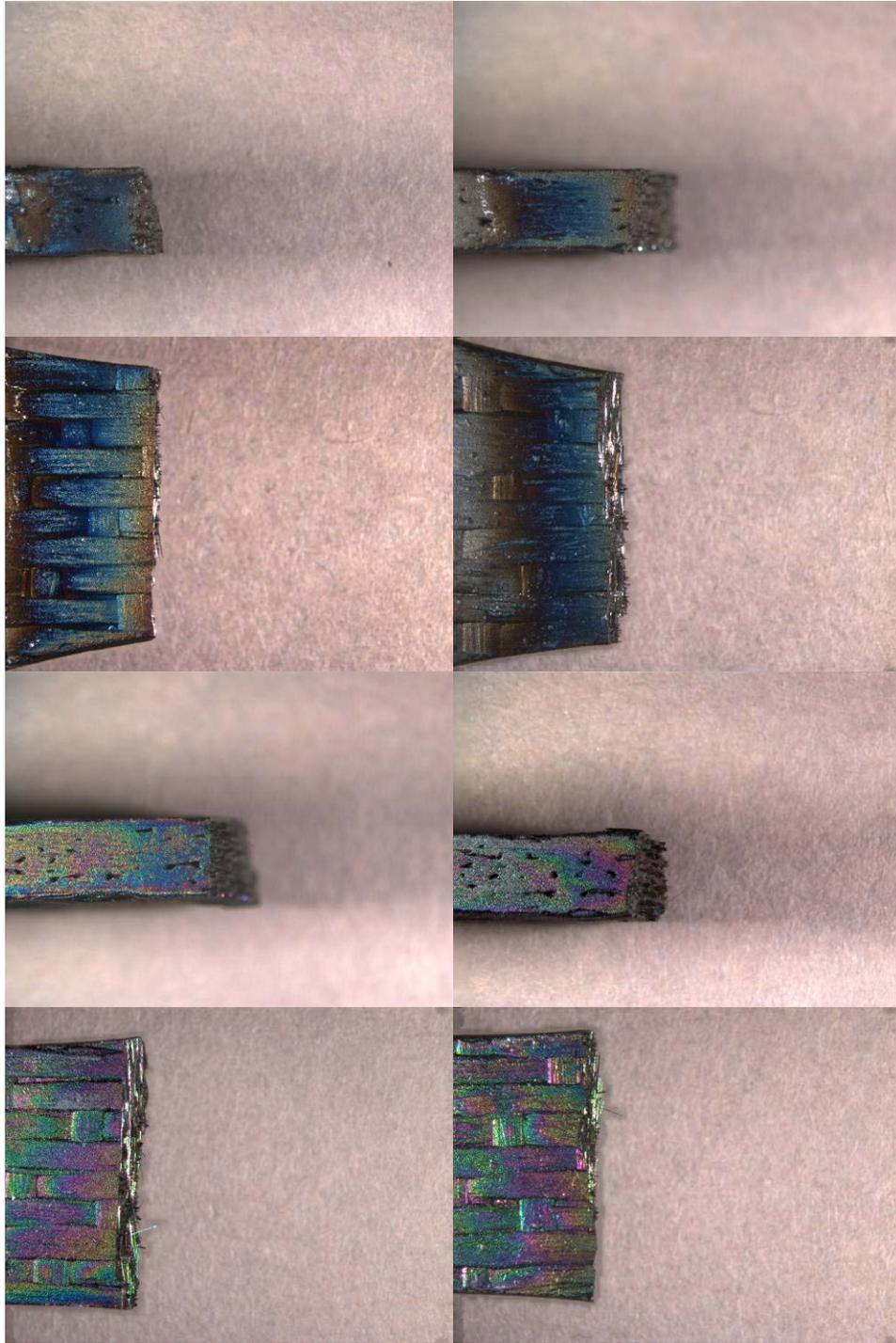
Figure 96: Optical micrographs of specimen P3-4 tested in fatigue at 10 Hz in steam at 1200 °C. σmax = 80 MPa, Nf = 33,451, tf = 0.93 h.
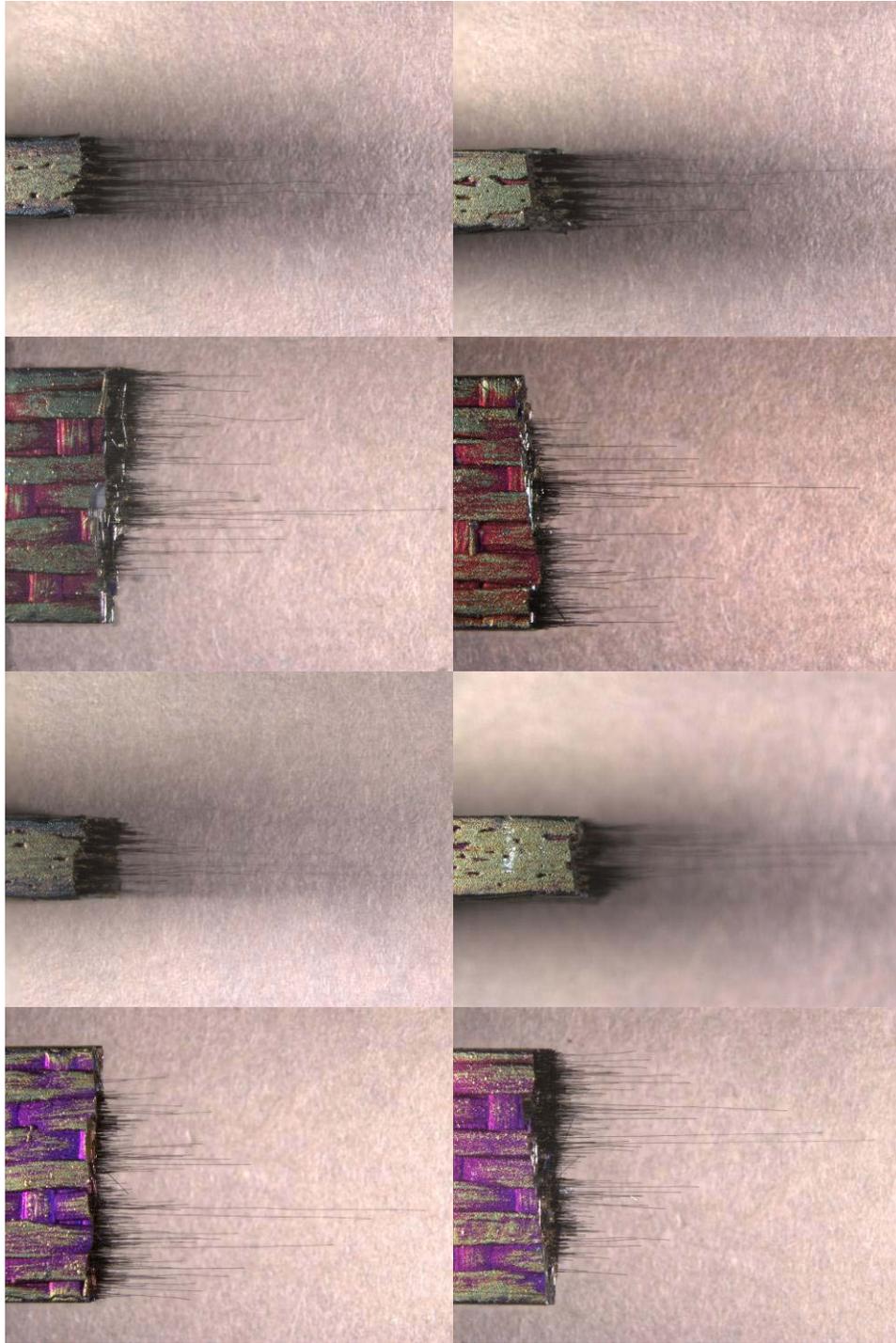
Figure 97: Optical micrographs of specimen P3-5 tested in fatigue at 0.1 Hz in air at 1200 °C. σmax = 120 MPa, Nf = 2092, tf = 5.81 h.
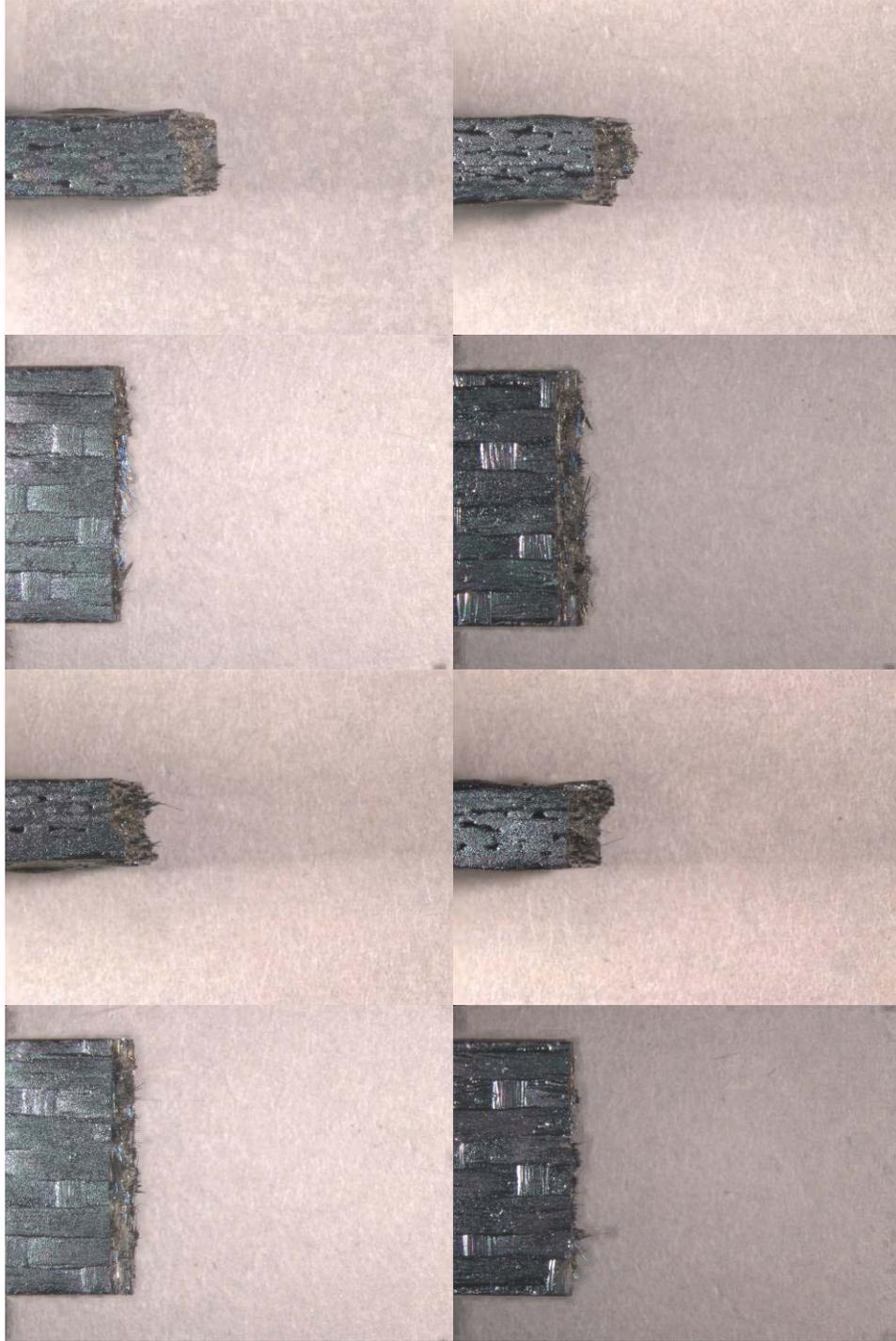
Figure 98: Optical micrographs of specimen P3-6 tested in fatigue at 10 Hz in steam at 1200 °C. σmax = 60 MPa, Nf = 200,000, tf = 5.56 h.
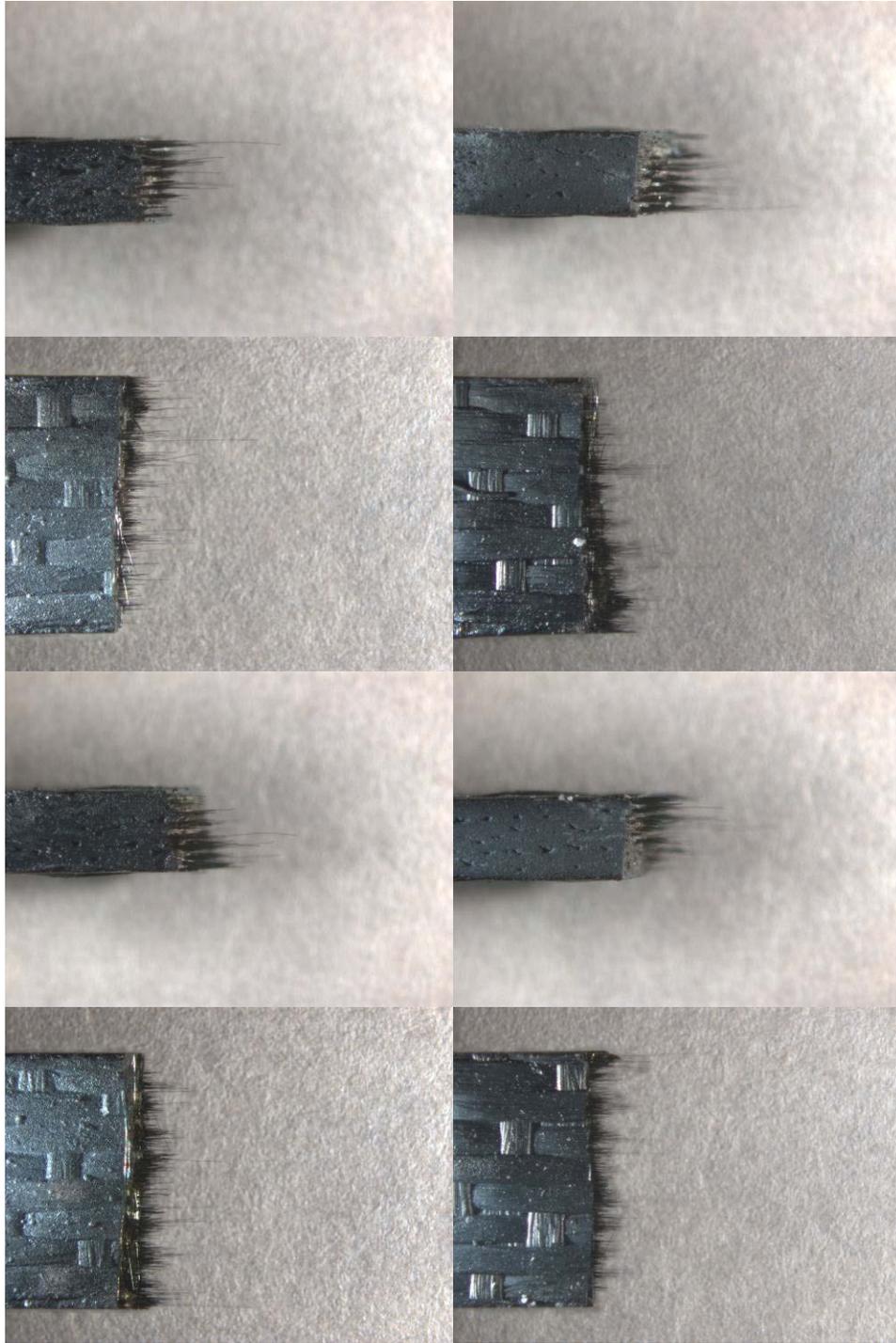
Figure 99: Optical micrographs of specimen P3-7 tested in fatigue at 0.1 Hz in steam at 1200 °C. σmax = 88 MPa, Nf = 88,575, tf = 246.04 h.
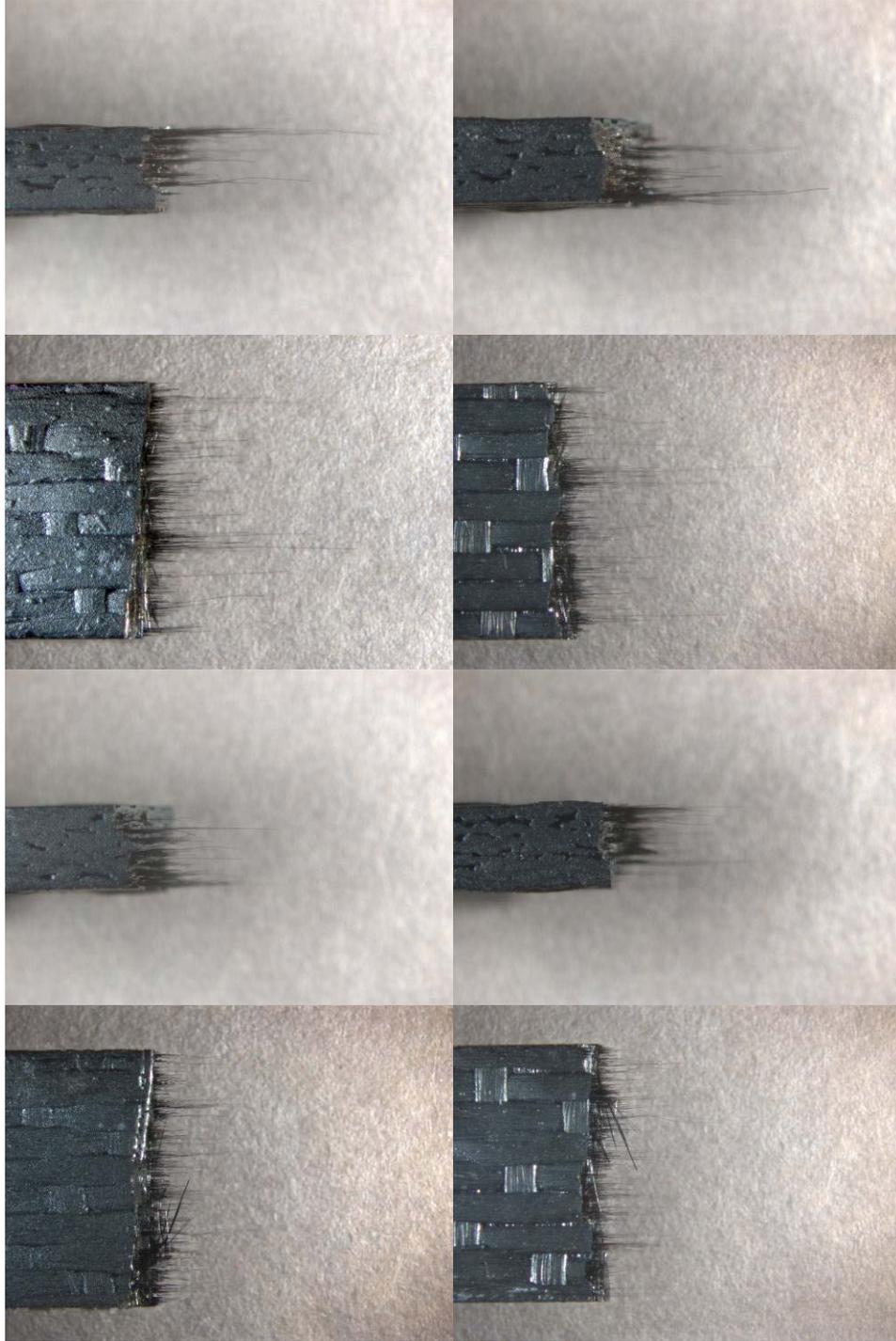
Figure 100: Optical micrographs of specimen P3-8 tested in fatigue at 0.1 Hz in steam at 1200 °C. σmax = 100 MPa, Nf = 13,726, tf = 38.12 h.
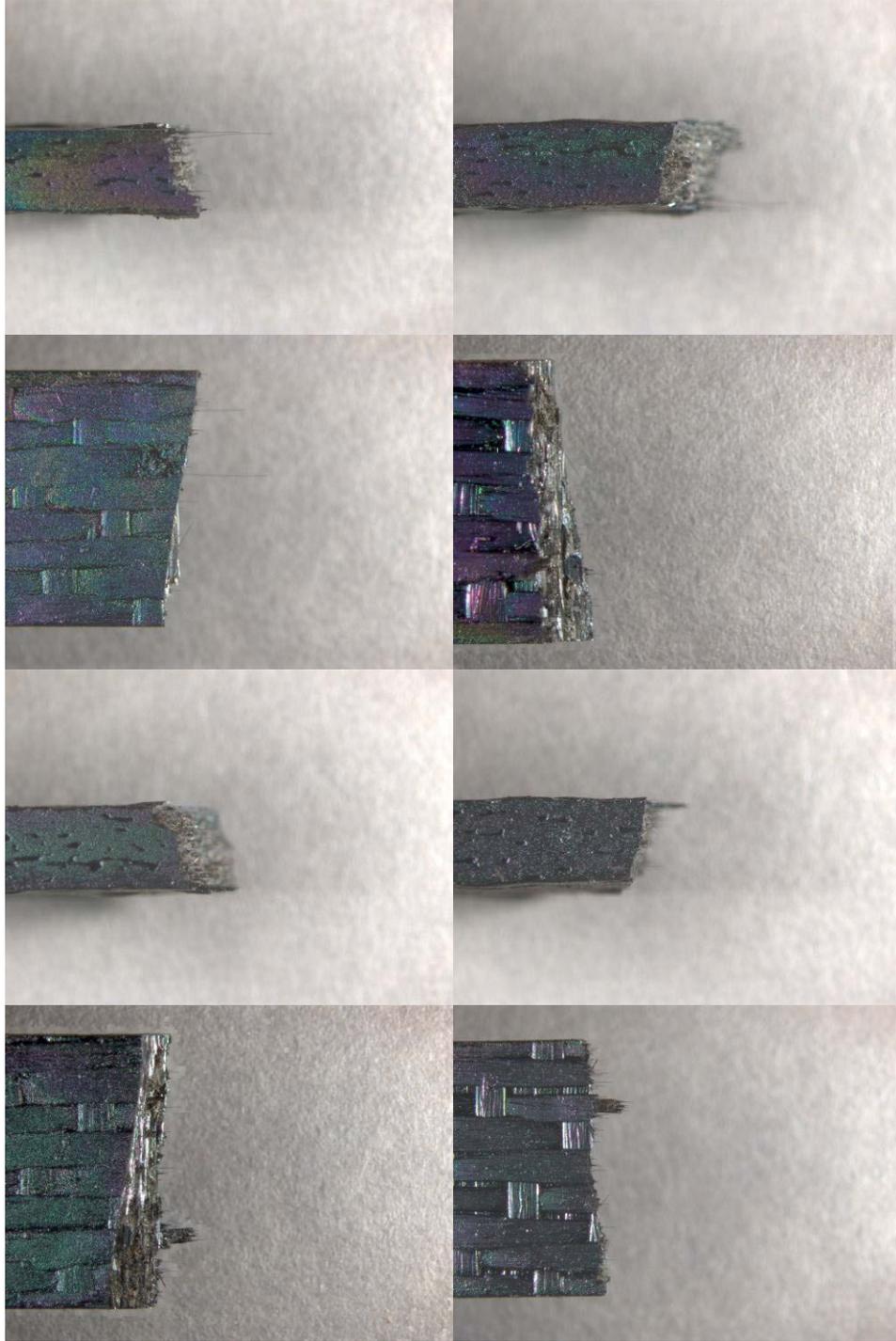
Figure 101: Optical micrographs of specimen P3-9 tested in fatigue at 0.1 Hz in steam at 1200 °C. σmax = 110 MPa, Nf = 548, tf = 1.52 h.
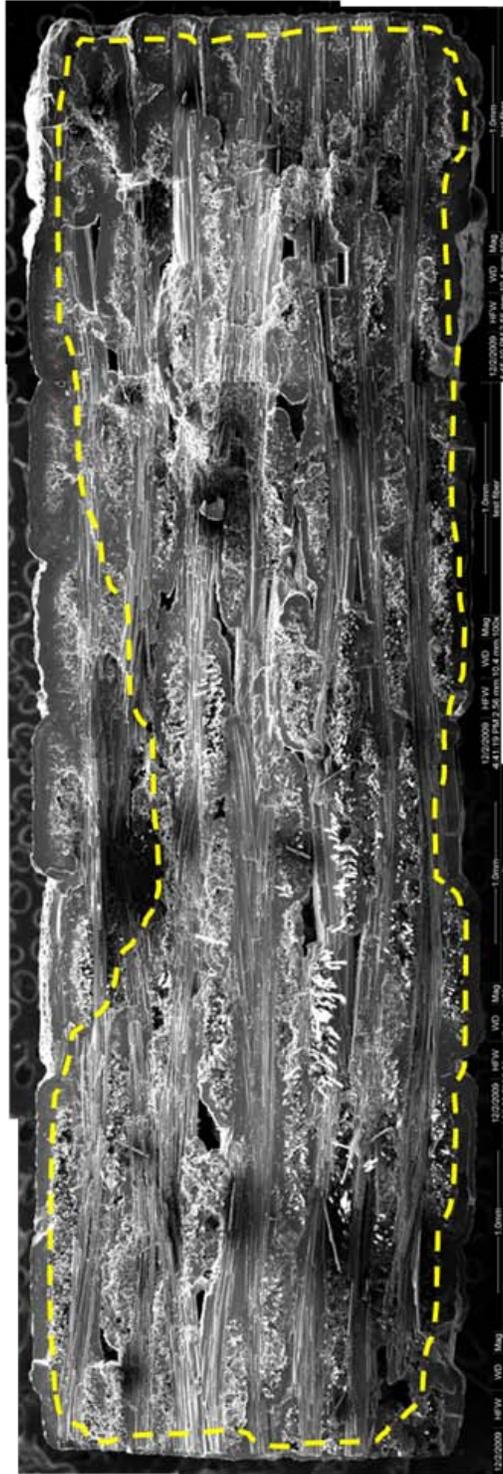
Figure 102: Compiled SEM micrographs of total P2-6 fracture surface after failing during 0.1 Hz fatigue testing at 1200 ^{o}C in air with σmax = 120 MPa. Environmental intrusion zone indicated by dotted line.
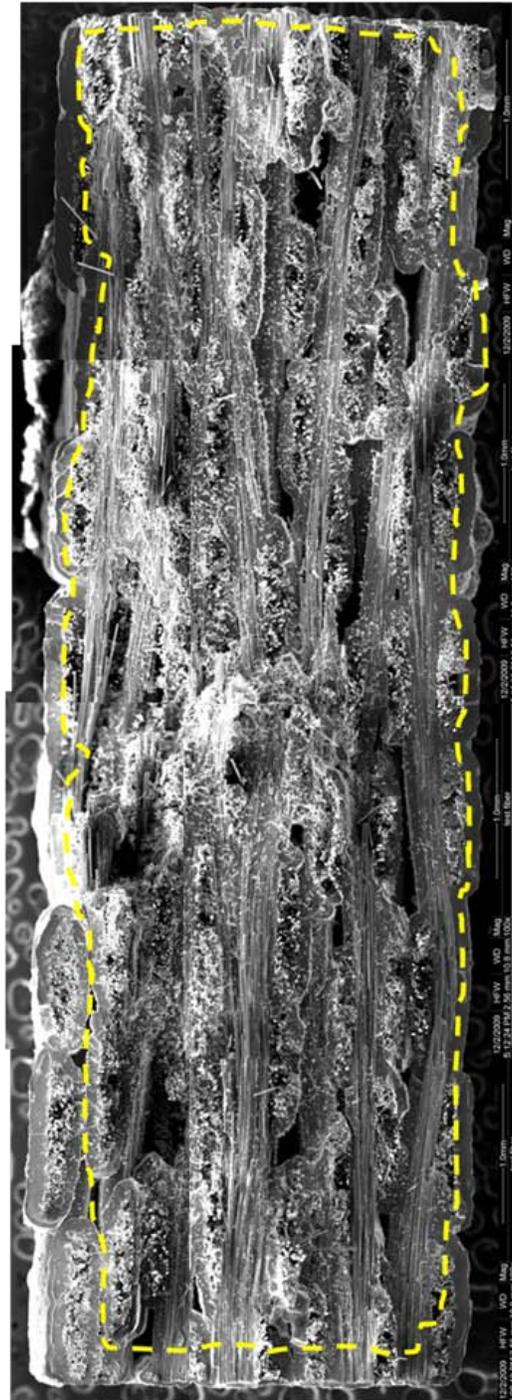
Figure 103: Compiled SEM micrographs of total P2-7 fracture surface after failing during 0.1 Hz fatigue testing at 1200 °C in air with σmax = 100 MPa. Environmental intrusion zone indicated by dotted line.
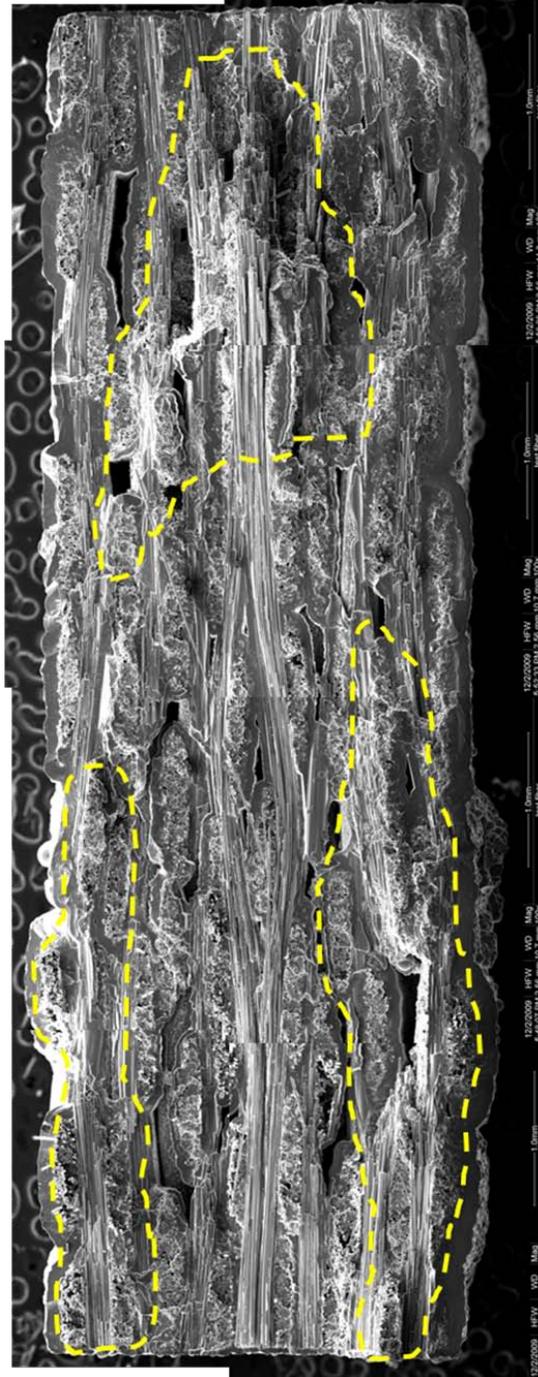
Figure 104: Compiled SEM micrographs of total P3-9 fracture surface after failing during 0.1 Hz fatigue testing at 1200 ^{o}C in steam with σmax = 110 MPa. Environmental intrusion zone indicated by dotted line.
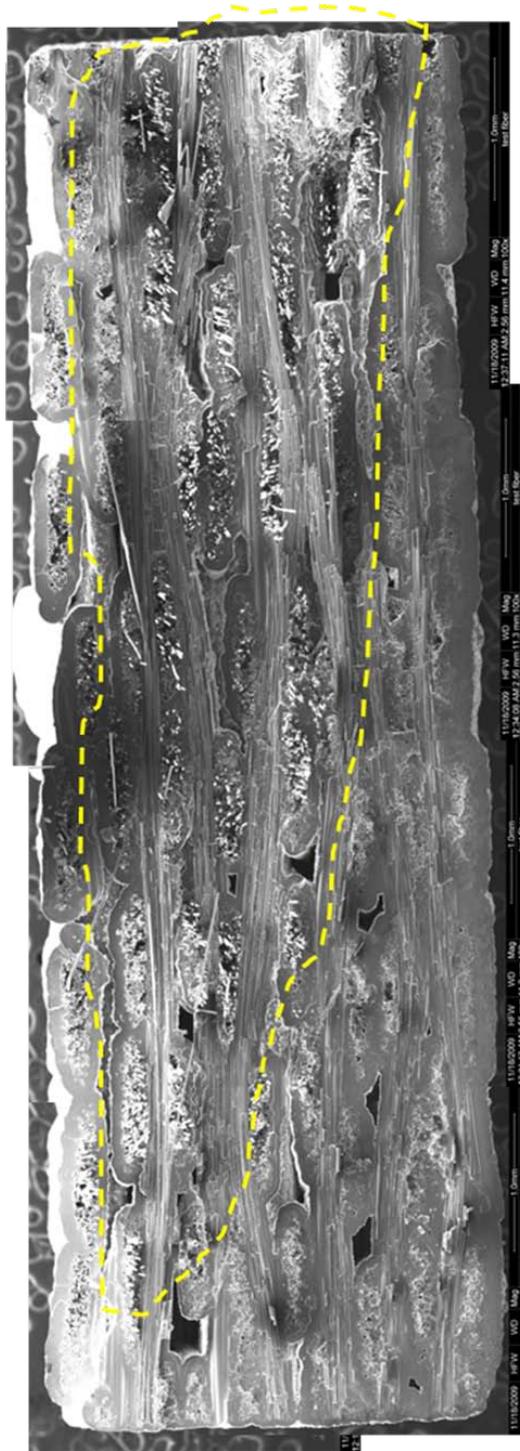
Figure 105: Compiled SEM micrographs of total P3-7 fracture surface after failing during 0.1 Hz fatigue testing at 1200 °C in steam with σmax = 88 MPa. Environmental intrusion zone indicated by dotted line.
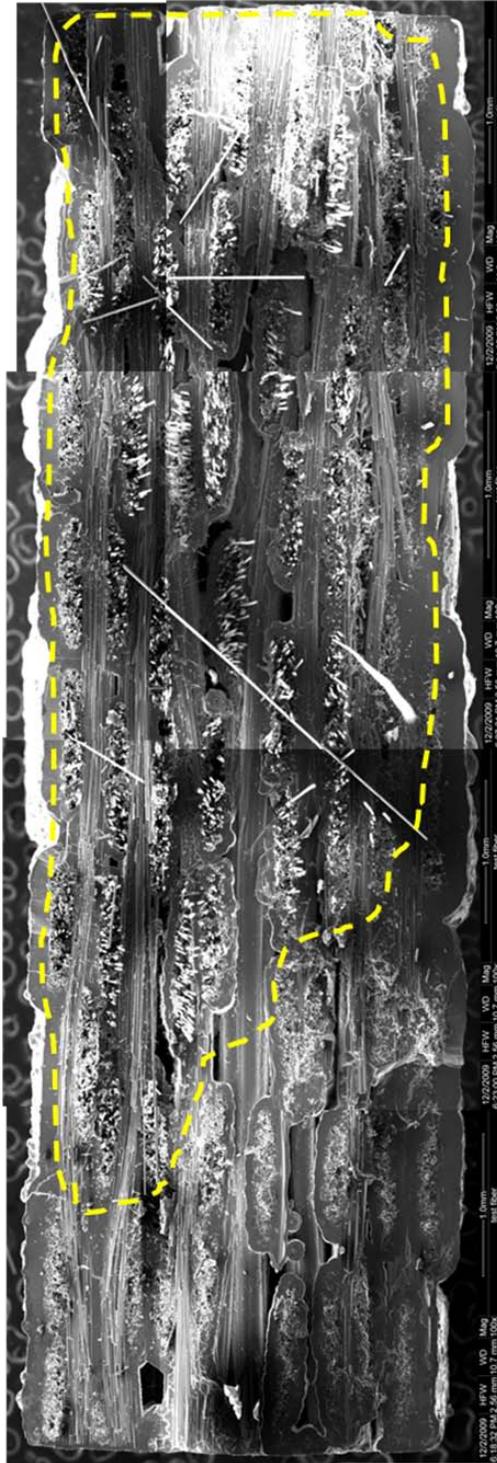
Figure 106: Compiled SEM micrographs of total P1-4 fracture surface after failing during 1.0 Hz fatigue testing at 1200 ^{o}C in air with σmax = 120 MPa. Environmental intrusion zone indicated by dotted line.
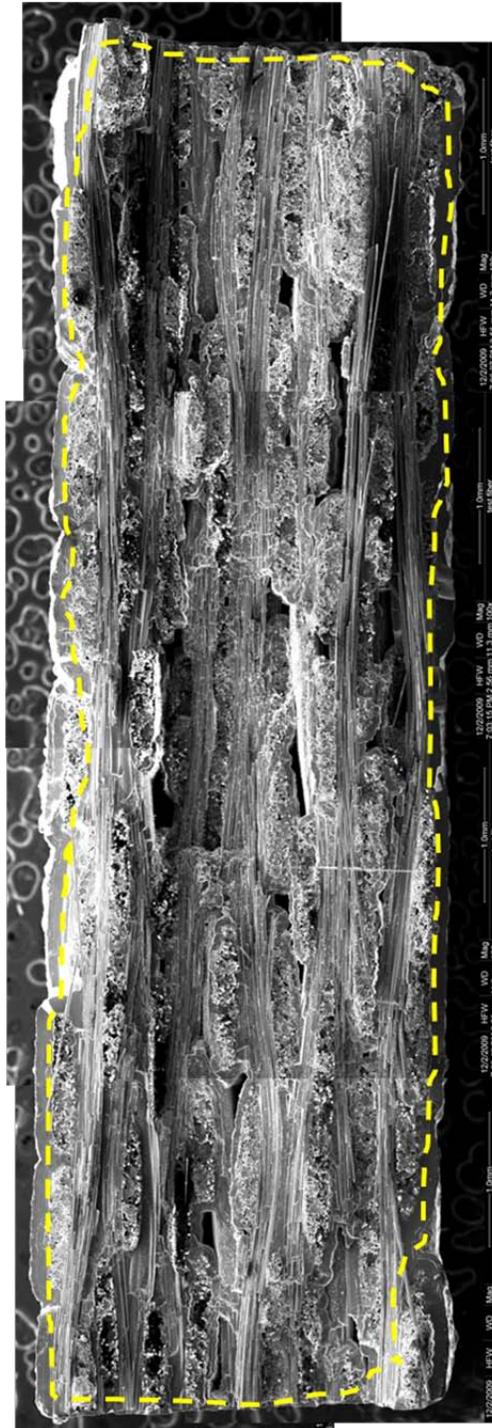
Figure 107: Compiled SEM micrographs of total P1-5 fracture surface after failing during 1.0 Hz fatigue testing at 1200 °C in air with σmax = 80 MPa. Environmental intrusion zone indicated by dotted line.
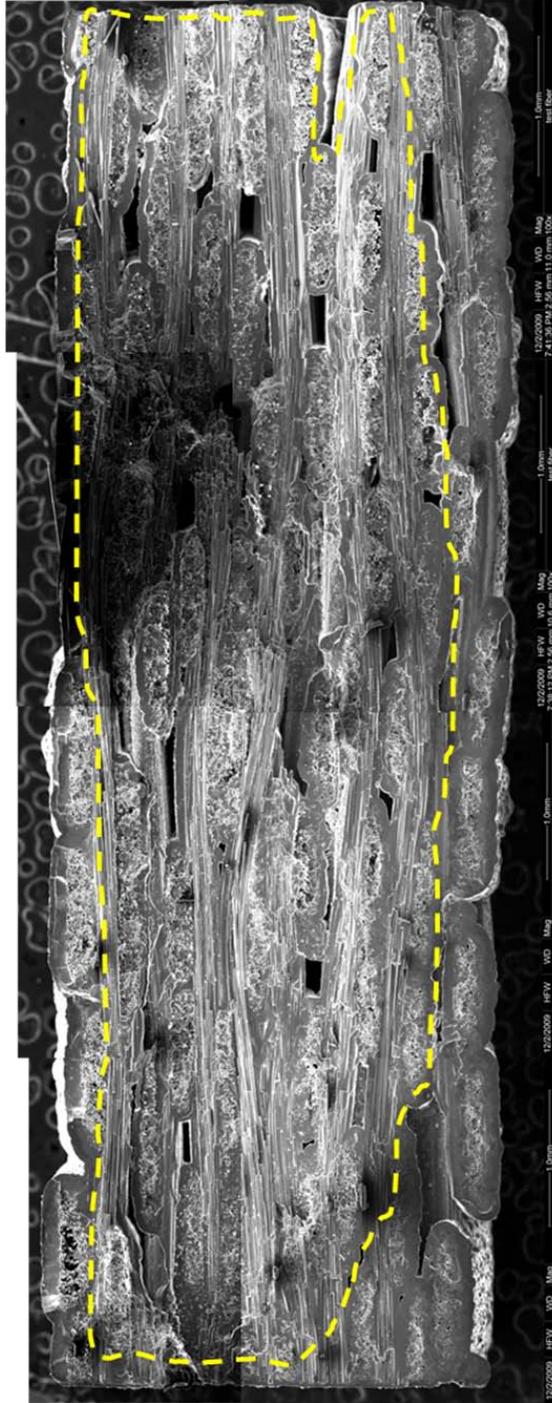
Figure 108: Compiled SEM micrographs of total P1-9 fracture surface after failing during 1.0 Hz fatigue testing at 1200 °C in steam with σmax = 100 MPa. Environmental intrusion zone indicated by dotted line.
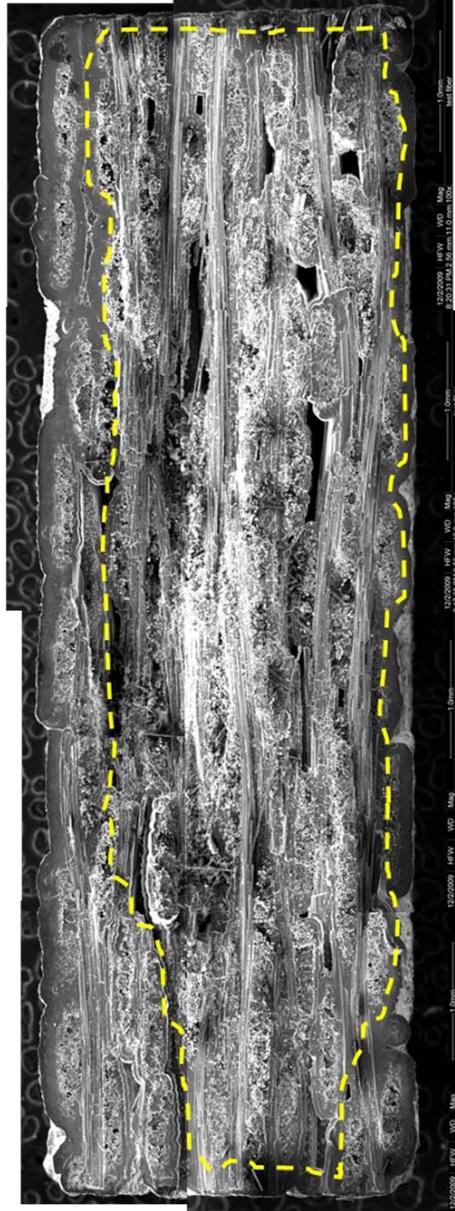
Figure 109: Compiled SEM micrographs of total P3-2 fracture surface after failing during 1.0 Hz fatigue testing at 1200 $^{\circ}$C in steam with σmax = 80 MPa. Environmental intrusion zone indicated by dotted line.
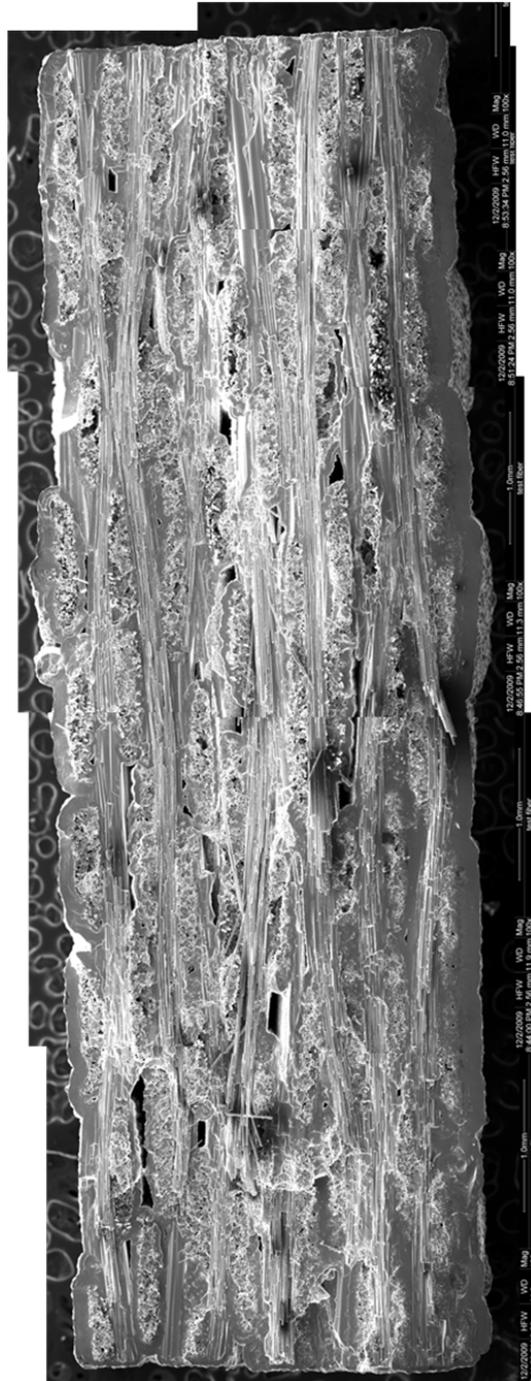
Figure 110: Compiled SEM micrographs of total P3-3 fracture surface after failing during 10 Hz fatigue testing at 1200 °C in air with σmax = 100 MPa. Environmental intrusion zone unidentifiable due to short time to failure.
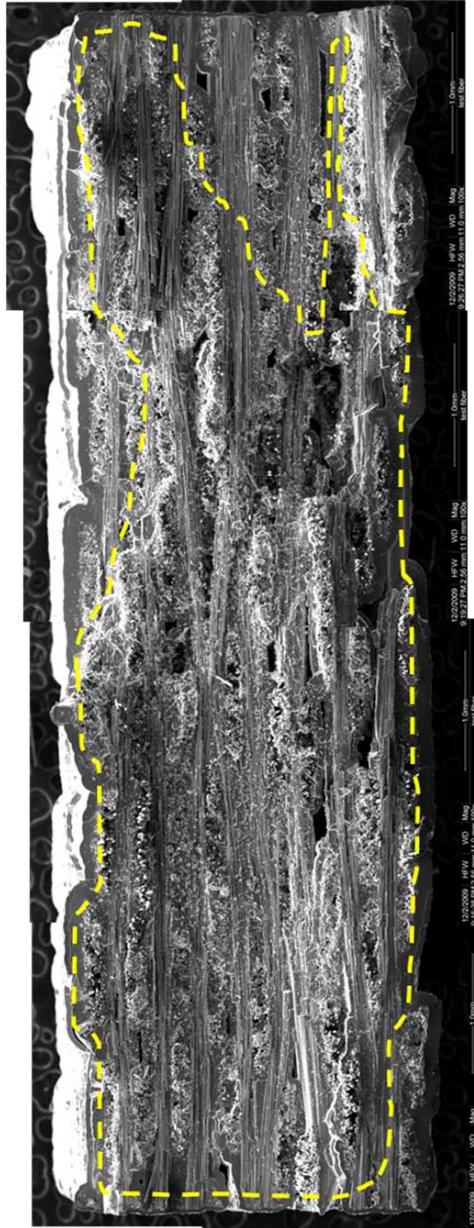
Figure 111: Compiled SEM micrographs of total P2-5 fracture surface after failing during 10 Hz fatigue testing at 1200 °C in air with σmax = 80 MPa. Environmental intrusion zone indicated by dotted line.
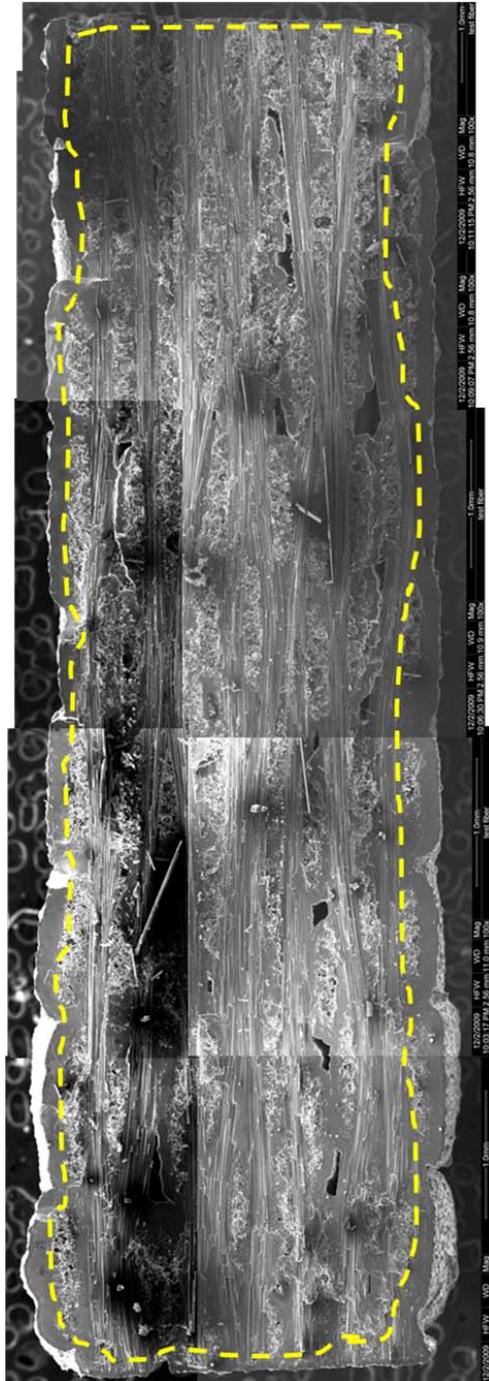
Figure 112: Compiled SEM micrographs of total P3-4 fracture surface after failing during 10 Hz fatigue testing at 1200 ^{o}C in steam with σmax = 80 MPa. Environmental intrusion zone indicated by dotted line.

Bibliography

1. AIAA Air Breathing Propulsion Technical Committee. *The Versatile Affordable Advanced Turbine Engine (VAATE) Initiative.* Reston: American Institute of Aeronautics and Astronautics, January 2006.

2. Campbell, F.C. *Manufacturing Technology For Aerospace Structural Materials.* London: Elsevier, 2006.

3. Chawla, K.K. *Ceramic Matrix Composites.* Boston: Kluwer Academic Publishers, 2003.

4. Daniel, Isaac M. and Ishai, Ori. *Engineering Mechanics of Composite Materials.* New York: Oxford University Press, 2006.

5. Dowling, Norman E. *Mechanical Behavior of Materials* (3rd Edition). New Jersey: Pearson Prentice Hall, 2007.

6. Eber, Chalene A. *Effect of Temperature and Steam Environment on Fatigue Behavior of an Oxide-Oxide Continuous Fiber Ceramic Composite.* MS Thesis, AFIT/GA/ENY/05-M09. School of Engineering and Management, Air Force Institute of Technology (AU), Wright-Patterson AFB, OH, March 2005.

7. Engesser, John Mark. *Monotonic, Creep-Rupture, and Fatigue Behavior of Carbon Reinforced Silicon Carbide (C/SiC) at an Elevated Temperature.* MS thesis, AFIT/GAE/ENY/04-M01. School of Engineering and Management, Air Force Institute of Technology (AU), Wright-Patterson AFB, OH, March 2004.

8. Fair, Geoff E. Private communications (2009).

9. Genelin, Christopher L. *Effects of Environment on Creep Behavior of Nextel 720/Alumina-Mullite Ceramic Composite at 1200^0C.* MS thesis, AFIT/GAE/ENY/08-M11. School of Engineering and Management, Air Force Institute of Technology (AU), Wright-Patterson AFB, OH, March 2008.

10. Hetrick, Griffin. *Effects of Frequency and Environment on Fatigue Behavior of an Oxide-Oxide Ceramic Matrix Composite and 1200^0C.* MS thesis, AFIT/GAE/ENY/06-J05. School of Engineering and Management, Air Force Institute of Technology (AU), Wright-Patterson AFB, OH, June 2006.

11. Kerans, Ronald J. Class lecture, MATL 685, Materials Selection and Processing. School of Engineering and Management, Air Force Institute of Technology, Wright-Patterson AFB, OH, February 2009.

12. Kim, Ted T. *Thermo-Mechanical Characterization of Silicon Carbide-Silicon Carbide Composites at Elevated Temperatures Using a Unique Combustion Facility.* Air Force Institute of Technology (AU), Wright-Patterson AFB, OH, September 2009 (ADA502557).

13. Krenkel, Walter (Editor). *Ceramic Matrix Composites.* Weinheim: Wiley-VCH Verlag GmbH & Co., 2008.

14. Mattingly, Jack D. and others. *Aircraft Engine Design.* Washington DC: American Institute of Aeronautics and Astronautics, Inc., 1987.

15. Mizuno, M, S. Zhu, Y. Nagano, Y. Sakaida, Y. Kagawa and M. Watanabe. "Cyclic-Fatigue behavior of SiC/SiC composites at room and high temperatures." Journal of American Ceramics, 79: 3065-3077 (June 1996).

16. Musikant, Soloman. *What Every Engineer Should Know About Ceramics.* New York: Marcel Dekker, Inc., 1991.

17. Naval Air Warfare Center Aircraft Divison. *Elevated Temperature Life Limiting Behavior of Hi-Nicalon SiC/SiC Ceramic Matrix Composite in Interlaminar Shear.* NAMCADPAX/TR-2007/5, March 2007.

18. Nogami, S, Hasegawa, A, Snead, L, Jones R, and Abe, K. "Effect of He pre-implantation and neutron irradiation on mechanical properties of SiC/SiC composite." Journal of Nuclear Materials, 329-333: 577-581 (2004).

19. Ruggles-Wrenn, M.B., Hetrick, G., Baek, S.S. "Effects of frequency and environment on fatigue behavior of an oxide-oxide ceramic composite at 1200^0C," International Journal of Fatigue, 30:502-516 (2008).

20. Ruggles-Wrenn, Marina B. Private communications (2009).

21. Sharma, Vipul. *Effects of Temperature and Steam Environment on Fatigue Behavior of Three SiC/SiC Ceramic Matrix Composites.* MS thesis, AFIT/GAE/ENY/08-S02. School of Engineering and Management, Air Force Institute of Technology (AU), Wright-Patterson AFB, OH, September 2008.

22. Wu, S, L. Cheng, Q. Zhang, L. Zhang, and Y. Xu. "Thermophysical and mechanical properties of a three dimensional Hi-Nicalon/SiC composite." International Journal of Applied Ceramic Technology, 3: 75-79 (2006).

23. Youngblood, G.E, and Newsome, G.A. *Dimensional Stability and Tensile Strength of Irradiated Nicalon-CG and Hi-Nicalon SiC Fibers.* Schenectady, New York: Kapl Atomic Power Laboratory, May 1997.

24. Zawada, Larry, J. Staehler, and S. Steel. "Consequence of Intermittent Exposure to Moisture and Salt Fog on the High-Temperature Fatigue Durability of Several Ceramic-Matrix Composites." Jounal of American Ceramics, 86: 1282-1291 (2003).

25. Zhu, S, M Mizuno, Y. Nagano, J. Cao, Y. Kagawa, and H. Kaya. "Creep and fatigue behavior in an enhanced SiC/SiC composite at high temperature." Journal of American Ceramics, 81: 2269-2277 (1998).

26. Zhu, S, M. Mizuno, Y. Kagawa, J. Cao, Y. Nagano, and H. Kaya. "Creep and fatigue behavior in Hi-Nicalon fiber reinforced silicon carbide composites at high temperature." Journal of American Ceramics, 82: 117-128 (1999).

27. Zhu, S, Mizuno, M, Kagawa, Y, and Mutoh, Y. "Monotonic tension, fatigue and creep behavior of SiC-fiber-reinforced SiC-matrix composites: a review." Composites Science and Technology, 59: 833-851 (January 1999).

VITA

Capt Devon T. Christensen was raised in Post Falls, Idaho. He graduated from St. George's High School in Spokane, Washington in 1997. In 1998 he entered the United States Air Force Academy in Colorado Springs, Colorado, graduating in 2002 with a Bachelor of Science in Aeronautical Engineering, and minors in both Mathematics and French.

His first assignment was as a project manager in the 412th Test Wing, Edwards AFB, CA. During this assignment he worked on T-38, F-15, and F-16 aircraft before taking charge of the X-45 unmanned combat aircraft project. His second assignment was as a structural engineer in the 84th Combat Sustainment Squadron, Hill AFB, UT. In this position Capt Christensen worked on T-37, T-38, F-4 and F-5 aircraft, as well as serving as the lead B-52 landing gear system engineer. Upon graduation from the Air Force Institute of Technology he will take an assignment in the Air Force Research Lab (AFRL) propulsion directorate at Wright-Patterson AFB, OH.

REPORT DOCUMENTATION PAGE				*Form Approved* *OMB No. 074-0188*
The public reporting burden for this collection of information is estimated to average 1 hour per response, including the time for reviewing instructions, searching existing data sources, gathering and maintaining the data needed, and completing and reviewing the collection of information. Send comments regarding this burden estimate or any other aspect of the collection of information, including suggestions for reducing this burden to Department of Defense, Washington Headquarters Services, Directorate for Information Operations and Reports (0704-0188), 1215 Jefferson Davis Highway, Suite 1204, Arlington, VA 22202-4302. Respondents should be aware that notwithstanding any other provision of law, no person shall be subject to an penalty for failing to comply with a collection of information if it does not display a currently valid OMB control number. **PLEASE DO NOT RETURN YOUR FORM TO THE ABOVE ADDRESS.**				
1. REPORT DATE *(DD-MM-YYYY)* 10-18-2009	**2. REPORT TYPE** Master's Thesis		**3. DATES COVERED** *(From – To)* May 2008 – Dec 2009	
4. TITLE AND SUBTITLE Fatigue Behavior of an Advanced SiC/SiC Composite at Elevated Temperature in Air and in Steam			**5a. CONTRACT NUMBER**	
			5b. GRANT NUMBER	
			5c. PROGRAM ELEMENT NUMBER	
6. AUTHOR(S) Christensen, Devon T., Capt, USAF			**5d. PROJECT NUMBER** 2009-075	
			5e. TASK NUMBER	
			5f. WORK UNIT NUMBER	
7. PERFORMING ORGANIZATION NAMES(S) AND ADDRESS(S) Air Force Institute of Technology Graduate School of Engineering and Management (AFIT/EN) 2950 Hobson Way WPAFB OH 45433-7765			**8. PERFORMING ORGANIZATION REPORT NUMBER** AFIT/GAE/ENY/09-D02	
9. SPONSORING/MONITORING AGENCY NAME(S) AND ADDRESS(ES) Dr. Geoff Fair Air Force Research Laboratory/Material and Manufacturing Directorate; Metals, Ceramics, and NDE Division 2230 Tenth Street, Bldg 655 WPAFB OH 45433-7765 DSN: 785-3232 geoff.fair@wpafb.af.mil			**10. SPONSOR/MONITOR'S ACRONYM(S)** AFRL/RXLN	
			11. SPONSOR/MONITOR'S REPORT NUMBER(S)	
12. DISTRIBUTION/AVAILABILITY STATEMENT APPROVED FOR PUBLIC RELEASE; DISTRIBUTION UNLIMITED.				
13. SUPPLEMENTARY NOTES				

14. ABSTRACT

The fatigue behavior of an advanced Silicon Carbide/Silicon Carbide (SiC/SiC) ceramic matrix composite (CMC) was investigated at 1200 ℃ in laboratory air and in steam environments. The composite consisted of a SiC matrix reinforced with Boron Nitride (BN) coated Hi-Nicalon fibers woven into eight-harness-satin (8HS) weave plies. Tensile stress-strain behavior and tensile properties were also evaluated at 1200 ℃. Tension-tension fatigue tests were conducted in both laboratory air and in steam at 1200 ℃ at frequencies of 0.1 Hz, 1.0 Hz, and 10 Hz. The tension-tension fatigue tests had a ratio of minimum stress to maximum stress of R = 0.1, with maximum stresses ranging from 80-120 MPa in air and 60-110 MPa in steam. Fatigue run-out was defined as 105 cycles for 0.1 Hz tests and as 2 x 105 cycles for 1.0 Hz and 10 Hz tests. Strain accumulation with cycles and modulus evolution with cycles were analyzed for each fatigue test. The CMC fatigue performance degraded after moving from the air to the steam environment. Fatigue limit was 100 MPa (46%UTS) in air and 80 MPa (37%UTS) in steam. Specimens that achieved run-out were subjected to tensile tests to failure to characterize the retained tensile properties. All specimens tested in air retained 100% of their tensile strength and only one specimen tested in steam showed strength degradation of approximately 5%. The average modulus loss in air and in steam was limited to 12%.

15. SUBJECT TERMS

Ceramic Matrix Composite (CMC), Silicon Carbide/Silicon Carbide Composite (SiC/SiC), Boron Nitride (BN), Chemical Vapor Inflitration (CVI), Fatigue Test, Tensile Properties, Environment

16. SECURITY CLASSIFICATION OF:			**17. LIMITATION OF ABSTRACT**	**18. NUMBER OF PAGES**	**19a. NAME OF RESPONSIBLE PERSON** Dr. Marina B. Ruggles-Wrenn
REPORT U	**ABSTRACT** U	**c. THIS PAGE** U	UU	151	**19b. TELEPHONE NUMBER** *(Include area code)* (937) 785-3636, ext 4641 Email: marina.ruggles-wrenn@afit.edu

Standard Form 298 (Rev: 8-98)
Prescribed by ANSI Std. Z39-18